

Wind related evolution of the Martian surface

Ph.D. dissertation by
Christina von Holstein-Rathlou
March 2011



Department of Physics and Astronomy
Faculty of Science
Aarhus University

Table of contents

Preface	i
Acknowledgements	ii
Publication list	iii
Peer-reviewed articles	iii
Extended abstracts	iii
Other publications and presentations	iv
Minor contributions	v
Abstract	vii
Resumé	viii

Part One – Background

Chapter 1 - Introduction to Mars	1
1.1 The Martian atmosphere	3
<i>1.1.1 Atmospheric carbon dioxide</i>	4
<i>1.1.2 Atmospheric dust</i>	5
Chapter 2 - Windblown sand and dust	7
2.1 Planetary boundary layers	7
2.2 Particle transport modes	8
2.3 Surface particle detachment	11
<i>2.3.1 Gravitational force</i>	12
<i>2.3.2 Adhesive force</i>	12
<i>2.3.3 Drag force</i>	13
<i>2.3.4 Lift force</i>	14
<i>2.3.5 Moment of torque</i>	14
<i>2.3.6 Results</i>	14
2.4 Modification to particle transportation modes	16
Chapter 3 - Aeolian Mars	17
3.1 Dust storms	17
3.2 Dust devils	17
3.3 Yardangs	18
3.4 Wind streaks	20
<i>3.4.1 Dark streaks</i>	20
<i>3.4.2 Bright streaks</i>	20
<i>3.4.3 Other streaks</i>	21
3.5 Dunes	21
<i>3.5.1 Dune movement</i>	22
3.6 Summary	23

Part Two – The Phoenix mission

Chapter 4 - The Phoenix mission	25
4.1 Meteorological investigations	26
4.2 Scientific instruments	27
4.2.1 <i>Dedicated soil analysis</i>	28
4.2.2 <i>Visual investigations</i>	28
4.2.3 <i>Meteorological instruments</i>	30
<i>The Telltale</i>	31
4.3 Meteorological results	32
4.3.1 <i>Diurnal cycle</i>	32
<i>Wind speeds and directions</i>	33
<i>Temperature and pressure</i>	34
4.3.2 <i>Seasonal changes</i>	35
<i>Wind speeds and directions</i>	35
<i>Temperature and pressure</i>	37
4.3.3 <i>Weather systems</i>	37
4.3.4 <i>Atmospheric water exchange</i>	40
4.4 Observations regarding aeolian transport	42
4.5 Conclusion	43
Chapter 5 - Telltale dust accumulation	45
5.1 Analysis of Telltale fibre contrast	45
5.2 Wind tunnel facility and dust analogue	50
5.3 Laboratory experiments	51
5.4 <i>Analysis</i>	52
5.5 Discussion and conclusion	55

Part Three – Electric Field Assisted Detachment

Chapter 6 - Electric Field Assisted Detachment	57
6.1 Electric field construction and discharge	58
6.2 Granular materials	60
6.3 Electric particle theory	61
6.4 Laboratory experiments	64
6.4.1 <i>Analysis</i>	65
6.5 Experimental results and discussion	69
6.6 Conclusion	72

Summary

Chapter 7 - Summary	75
7.1 The Phoenix mission	75
7.2 Electric field assisted detachment	76
7.3 Future work	76

Appendix

A References	I
A.1 Websites	XI
B <i>Winds at the Phoenix landing site</i>	XIII

Preface

This Ph.D. project has been carried out at the Department of Physics and Astronomy at Aarhus University in Denmark as a part of the ongoing activities of the Mars Simulation Laboratory. The project has run from April 2008 till March 2011 under the supervision of Jonathan Merrison and Haraldur Pall Gunnlaugsson. The main focus of the project has been on obtaining and analyzing data from the Danish contributed wind measuring instrument to the Phoenix Mars mission, the Telltale. Much of this was achieved with my participation as a member of the Atmospheric Science Theme Group in the landed operations of the Phoenix mission from May to November 2008. This body of work has utilized the unique experimental facilities available through the Mars Simulation Group both for the dealings with the Telltale as well as additional research on dust movement under the influence of electric fields.

The structure of the dissertation is as follows:

Part One introduced background information about the planet Mars, the physics governing dust and sand movement by wind as well as a presentation and discussion of windblown sand and dust observed on Mars.

Part Two introduces the Phoenix mission and the main meteorological results which include, but are not limited to, the results obtained from the Telltale instrument. Following this is the experimental research on time-dependent dust accumulation on the Telltale and its affect on the Telltale data. The complete work of the analysis of Telltale data from the Phoenix mission can be found in the article by C. Holstein-Rathlou et al. with the title *Winds at the Phoenix Landing Site* which is in the appendix.

Part Three concerns the experimental work regarding electric field assisted detachment of sand grains from a surface. It is a continuation of previous work performed by Jonathan Merrison and students, and this work has opened new avenues of research for future students.

The final chapter is a summary of the work done in this Ph.D. which assesses the knowledge gained of wind related processes on Mars. Finally there is a short discussion of possible avenues of future work based on the experiments performed in the course of this Ph.D.

After the submission of this thesis the chapter on electric field assisted detachment will be written as an article and submitted for publication.

Acknowledgements

I would like to greatly thank my advisors, Haraldur Páll Gunnlaugsson (Palle) and Jonathan Merrison, for all the wonderful things they have done to aid and assist me during my Ph.D. Your help and support in the laboratory, the office, at conferences and at the Phoenix mission have been invaluable and I am forever thankful. Thank you to the people of the Mars Simulation Laboratory group at Aarhus University for the use of laboratory facilities and materials for my experiments as well as many interesting Tuesday morning meetings.

I would like to thank Morten Bo Madsen for introducing me to Palle and his work, for my master thesis, thereby starting me on my road to this Ph.D. Thank you for getting me involved with the Phoenix mission and ultimately letting me experiencing the mission madness before, during and after landed operations. It was a wonderful experience.

I fondly remember the entire Phoenix science team, PR-personnel and “background” technical people with whom I have spent many wonderful months at the Phoenix Science Operations Center in Tucson, Arizona and met up with at many conferences since then. Thank you to the Atmospheric Science Theme Group for many wonderful scientific conversations on everything meteorological as well as entrusting me with leadership of the group allowing me to learn how missions are actually run. Special thanks go to Leslie Tamppari, an inspiring woman, mother and project scientist, who has shown be the great many things one can accomplish as a woman and a scientist. Thank you to the entire SSI imaging team, both the up- and downlink people, for the many wonderful Telltale images we received during the mission.

On a personal note I would like to give a special thanks to the Danish Phoenix contingency for the many wonderful hours spent carpooling, adventuring, eating and generally enjoying life during the Phoenix mission at all crazy hours of the day. To Pat, Keri, “Chewie”, Stephanie, Cherie, Rigel, Selby, Troy, Suzanne and Carla goes my personal thanks for our daily hugs, jokes, good times and wonderful conversations in hallways during the mission. What a wonderful flock of people to spend those many months with. Thank you to Sara Hammond for my “going away present”, the Marvin the Martian pin, which I had adored since first setting eyes on it and will always treasure!

The work was financed by the Niels Bohr Institute, University of Copenhagen, the Mars Simulation Laboratory and the Faculty of Sciece, Aarhus University. Thank you to especially Per Nørnberg and Morten Bo Madsen for their hard work in arranging and ensuring the funding for my Ph.D. and participation in the Phoenix mission. My participation in the Phoenix mission would not have been possible without Morten and Palle and the financial support they received from the Research Council for Nature and Universe (FNU).

Finally I would like to thank my friends and family for your never-ending support and listening ears which have endured with me during my many long years of scientific education that has brought me to this point. A heartfelt thanks to Kim Hedegaard Kristensen for coping with me during these final months of my Ph.D., keeping my spirits up through sickness and thesis writing with his encouragement and love, giving me a reason to go home every day.

Publication list

Peer-reviewed articles

Holstein-Rathlou, C., H.P. Gunnlaugsson, J.P. Merrison, K.M. Bean, B.A. Cantor, J.A. Davis, R. Davy, N.B. Drake, M.D. Ellehoj, W. Goetz, S.F. Hviid, C.F. Lange, S.E. Larsen, M.T. Lemmon, M.B. Madsen, M. Malin, J.E. Moores, P. Nørnberg, P. Smith, L.K. Tamppari, P.A. Taylor (2010) Winds at the Phoenix landing site, *J. Geophys. Res.*, 115, E00E18, doi: 10.1029/2009JE003411

Gunnlaugsson, H.P., C. Holstein-Rathlou, J.P. Merrison, S.K. Jensen, C.F. Lange, S.E. Larsen, M.B. Madsen, P. Nørnberg, H. Bechtold, E. Hald, J.J. Iversen, P. Lange, F. Lykkegaard, F. Rander, M. Lemmon, N. Renno, P. Taylor, P. Smith (2008) Telltale wind indicator for the Mars Phoenix lander, *J. Geophys. Res.*, 113, E00A04, doi: 10.1029/2007JE003008

Extended abstracts

Holstein-Rathlou, C., H.P. Gunnlaugsson, S.K. Jensen, C.F. Lange, M.B. Madsen, J. Merrison, P. Nørnberg, P. Smith, the Phoenix Science team (2008) The Telltale Wind Experiment for the NASA Phoenix Mars Lander 2008, *Geophysical Research Abstracts*, Vol. 10, EGU2008-A-11861, *EGU General Assembly 2008*, April 13-18, 2008, Vienna, Austria (poster)

Holstein-Rathlou, C., H.P. Gunnlaugsson, P. Taylor, C. Lange, J. Moores, M. Lemmon (2008) Winds at the Phoenix Landing Site, *American Geophysical Union, Fall Meeting 2008*, December 15-19, 2008, San Francisco, California, USA, Abstract U11B-0025 (poster)

Holstein-Rathlou, C., H.P. Gunnlaugsson, P. Taylor, C. Lange, J. Moores, M. Lemmon (2009) Winds at the Mars Phoenix Landing Site, *40th Lunar and Planetary Science Conference*, March 23-27, 2009, The Woodlands, Texas, USA, Abstract 1548 (talk)

Holstein-Rathlou, C., H.P. Gunnlaugsson, J.P. Merrison, P. Nørnberg, M.D. Ellehoj, K.M. Bean, M.T. Lemmon, L. Tamppari, P. Smith (2010) Time-dependent Dust Accumulation on the Mars Phoenix Wind Indicator, *41st Lunar and Planetary Science Conference*, March 1-5, 2010, The Woodlands, Texas, USA, Abstract 1811 (poster)

Holstein-Rathlou, C. et al. (2010) On Dust Storms Observed at the Phoenix Landing Site, *41st Lunar and Planetary Science Conference*, March 1-5, 2010, The Woodlands, Texas, USA, Abstract 1837 (poster)

Holstein-Rathlou, C. et al. (2010) Time-dependent Dust Accumulation on the Mars Phoenix Wind Indicator, *EPSC Abstracts*, Vol. 5, EPSC2010-388, *European Planetary Science Congress 2010*, September 19-24, 2010, Rome, Italy (poster)

Gunnlaugsson, H.P., C. Holstein-Rathlou, J.P. Merrison, C.F. Lange, M. Lemmon, P. Nørnberg, P. Taylor, P. Smith (2009) Winds at the Mars Phoenix landing site, *Geophysical Research Abstracts*, Vol. 11, EGU2009-7208, *EGU General Assembly 2009*, April 19-24, 2009, Vienna, Austria (talk)

Gunnlaugsson, H.P., C. Holstein-Rathlou, P. Taylor, Phoenix Science team (2010) Midnight temperature fluctuations at Mars Phoenix lander: Influence from Heimdal crater?, *EPSC Abstracts*, Vol. 5, EPSC2010-682, *European Planetary Science Congress 2010*, September 19-24, 2010, Rome, Italy (poster)

Gunnlaugsson, H.P., C. Holstein-Rathlou, J.P. Merrison, M.D. Ellehoj, M.T. Lemmon, Phoenix Science Team (2010) Time-Dependent dust accumulation on the Telltale fibres of the Phoenix mission, *Geophysical Research Abstracts*, Vol. 12, EGU2010-3153, *EGU General Assembly 2010*, May 2-7, 2010, Vienna, Austria (poster)

Other publications and presentations

Holstein-Rathlou, C., H.P. Gunnlaugsson and J.P. Merrison (2009) Telltale Calibration Report, ver.7, technical document, Department of Physics and Astronomy, Aarhus University, Århus, Denmark (Can be found through the Planetary Data System: http://atmos.nmsu.edu/pdsd/archive/data/phx-m-tt-5-wind-vel-dir-v10/phxwnd_0001/DOCUMENT/)

Holstein-Rathlou, C. et al. (2009) The Phoenix Mars mission: wind, water and habitability, *NASA-Nordic Astrobiology Summer School*, June 29 - July 13, 2009, Reykjavik, Iceland (poster)

Holstein-Rathlou, C. et al. (2010) Habitability at the Mars Phoenix landing site, *Astrobiology Graduate Conference 2010*, June 14-18, 2010, Tällberg, Sweden (talk)

Holstein-Rathlou, C. et al. (2010) Winds at the Phoenix landing site, *Danish Physical Society Annual Meeting*, June 22-23, 2010, Nyborg, Denmark (poster)

Larsen, S.E., H.E. Jørgensen, C. Holstein-Rathlou (2010) Vind og vejr på Mars (EN: Wind and weather on Mars), *Dansk Astronomi i Kikkerten*, Chp. 13, Forlaget Epsilon.dk, ISBN: 978-87-993384-0-5

Presentations on the progress of the work done with the Telltale data from the Phoenix mission was given at the Phoenix Science Team Meeting 16 (Dec. 13-14, 2008 at NASA Ames, Moffett Field, CA, USA) and Phoenix Science Team Meeting 17 (March 21-22, 2009 at Space Center Houston, TX, USA)

Article about studying astronomy at the University of Copenhagen for "Studies in Natural Science 2005" aimed at new students in astronomy. The article (in danish) can be found at: <http://www.nat.ku.dk/uddannelser/bachelor/astronomi/studerende/>

Minor contributions

My contribution to the following articles and abstracts consists in supplying and explaining the Telltale wind data for use in further analysis..

Ellehøj, M.D., P.A. Taylor, H.P. Gunnlaugsson, B.T. Gheynani, C. Holstein-Rathlou, L. Drube, J. Whiteway (2008) Phoenix: Dustless Devils at the Lander Site, *Third International Workshop on The Mars Atmosphere: Modeling and Observations*, November 10-13, 2008, Williamsburg, Virginia, USA, Abstract 1447

Ellehøj, M.D., H.P. Gunnlaugsson, P.A. Taylor, B.T. Gheynani, J. Whiteway, M.T. Lemmon, K.M. Bean, L.K. Tamppari, L. Drube, C. Von Holstein-Rathlou, M.B. Madsen, D. Fisher, P. Smith (2009) Dust Devils and Vortices at the Phoenix Landing Site on Mars, *40th Lunar and Planetary Science Conference*, held March 23-27, 2009, The Woodlands, Texas, USA, Abstract 1558

Ellehoj, M.D., H.P. Gunnlaugsson, P.A. Taylor, H. Kahanpää, K.M. Bean, B.A. Cantor, B.T. Gheynani, L. Drube, D. Fisher, A.-M. Harri, C. Holstein-Rathlou, M.T. Lemmon, M.B. Madsen, M.C. Malin, J. Polkko, P.H. Smith, L.K. Tamppari, W. Wend, J. Whiteway (2010) Convective vortices and dust devils at the Phoenix Mars mission landing site, *J. Geophys. Res.*, 115, E00E16, doi: 10.1029/2009JE003413

Gunnlaugsson, H.P., M.D. Ellehøj, P.A. Taylor, J. Whiteway, M.T. Lemmon, L.K. Tamppari, L. Drube, C. Holstein-Rathlou, M.B. Madsen (2009) Dust Devils and vortices at the Phoenix landing site on Mars, *Geophysical Research Abstracts*, Vol. 11, EGU2009-9979, *EGU General Assembly 2009*, April 19-24, 2009, Vienna, Austria

Merrison, J.P., M.B. Madsen, C. Holstein-Rathlou, H.P. Gunnlaugsson, P. Nornberg, K.R. Rasmussen (2009) Wind Driven Grain Transport on Mars, *Workshop on the Microstructure of the Martian Surface*, August 27-29, 2009, Copenhagen, Denmark, Abstract 1505

Merrison, J.P., M.B. Madsen, C. Holstein-Rathlou, H.P. Gunnlaugsson, P. Nornberg, K.R. Rasmussen (2009) Properties of the Martian Dust Aerosol, *EPSC Abstracts*, Vol. 4, EPSC2009-77, *European Planetary Science Congress 2009*, September 14-18, 2009, Potsdam, Germany

Merrison, J.P., C. Holstein-Rathlou, H.P. Gunnlaugsson, P. Nornberg (2009) A European Mars Simulation Wind Tunnel Facility, *EPSC Abstracts*, Vol. 4, EPSC2009-76, *European Planetary Science Congress 2009*, September 14-18, 2009, Potsdam, Germany

Merrison, J.P., C. Holstein-Rathlou, H.P. Gunnlaugsson, P. Nornberg (2009) A Forthcoming European Mars Simulation Wind Tunnel Facility, *40th Lunar and Planetary Science Conference*, March 23-27, 2009, The Woodlands, Texas, USA, Abstract 1544

Tamppari, L.K., D.S. Bass, B. Cantor, I. Daubar, D. Fisher, K. Fujii, H.P. Gunnlaugsson, T.L. Hudson, D. Kass, A. Kleinboehl, M. Lemmon, M. Mellon, A. Pankine, N. Renno, M. Searls, F. Seelos, P. Taylor, C. von Holstein-Rathlou, J. Whiteway, M. Wolff (2008) Phoenix and Mars Reconnaissance Orbiter Coordinated Atmospheric Science, *American Geophysical Union, Fall Meeting 2008*, December 15-19, 2008, San Francisco, California, USA, Abstract P33C-03

Tamppari, L.K., D.S. Bass, B. Cantor, I. Daubar, D. Fisher, K. Fujii, H.P. Gunnlaugsson, T.L. Hudson, D. Kass, A. Kleinboehl, M. Lemmon, M. Mellon, A. Pankine, M. Searls, F. Seelos, S. Smrekar, P. Taylor, C. von Holstein-Rathlou, J. Whiteway, M. Wolff (2009) Phoenix and MRO Coordinated Atmospheric Science, *40th Lunar and Planetary Science Conference*, held March 23-27, 2009, The Woodlands, Texas, USA, Abstract 2000

Tamppari, L.K., D. Bass, B. Cantor, I. Daubar, C. Dickinson, D. Fisher, K. Fujii, H.P. Gunnlaugsson, T.L. Hudson, D. Kass, A. Kleinböhl, L. Komguem, M.T. Lemmon, M. Mellon, J. Moores, A. Pankine, J. Pathak, M. Searls, F. Seelos, M.D. Smith, S. Smrekar, P. Taylor, C. Holstein-Rathlou, W. Weng, J. Whiteway, M. Wolff (2010) Phoenix and MRO coordinated atmospheric measurements, *J. Geophys. Res.*, 115, E00E17, doi: 10.1029/2009JE003415

Taylor, P.A., H.P. Gunnlaugsson, C. Holstein-Rathlou, C.F. Lange, J. Moores, C. Cook, C. Dickinson, V. Popovici, J. Seabrook, J. Whiteway (2008) Phoenix: Summer Weather in Green Valley (126W, 68N on Mars), *Third International Workshop on The Mars Atmosphere: Modeling and Observations*, November 10-13, 2008, Williamsburg, Virginia, USA, No. 1447, p.9024

Taylor, P.A., C. Cook, M. Daly, R. Davy, C. Dickinson, L. Drube, M.D. Ellehoj, B.T. Gheynani, H.P. Gunnlaugsson, A. Harri, V. Hipkin, C. Holstein-Rathlou, H. Kahgnpag, C.F. Lange, J. Polkko, V. Popovici, N. Renno, W. Weng, J. Whiteway (2008) Temperature and Pressure at the Phoenix Landing Site, *American Geophysical Union Fall Meeting 2008*, December 15-19, 2008, San Francisco, California, USA, Abstract U11B-0023

Whiteway, J., L. Komguem, C. Dickinson, C. Cook, M. Illnicki, V. Popovici, J. Seabrook, M. Daly, A. Carswell, P. Taylor, R. Davy, J. Pathak, C. Lange, D. Fisher, V. Hipkin, L. Tamppari, M. Lemmon, N. Renno, H. Gunnlaugsson, L. Drube, C. Holstein-Rathlou, P. Smith (2008) Observations of Dust, Ice Water Clouds, and Precipitation in the Atmosphere of Mars, *American Geophysical Union Fall Meeting 2008*, December 15-19, 2008, San Francisco, California, USA, Abstract U14A-09

Abstract

Analysis of data from the NASA Phoenix Mars mission and laboratory experiments performed at Aarhus University have been combined to examine specific aspects of the wind related evolution of the Martian surface.

The first meteorological measurements in the northern polar region of Mars were performed during the Phoenix mission. Wind speeds and directions were measured by a mechanical anemometer, the Telltale, through analysis of images taken with the onboard imager. Other meteorological instruments included a pressure sensor, three thermocouples and a LIDAR. They were supplemented by observations from the Surface Stereo Imager as well as coordinated measurements between the Phoenix lander and the instruments onboard the Mars Reconnaissance Orbiter (MRO). The diurnal cycle was characterized by calm nocturnal conditions and the presence of convective turbulence during daytime. Telltale wind data suggests that Heimdall crater is the source of the nocturnal temperature fluctuations. Seasonal changes were reflected by increased average wind speeds, wind directions continuously from west and decreasing temperature and pressure.

Observations made with Mars Color Imager on MRO and the Telltale suggested two different mechanisms for the dust lifting events affecting the Phoenix landing site. Prior to $L_s \sim 95^\circ$ events were associated with the evaporation of the seasonal CO_2 ice but not with increased wind speeds. After $L_s \sim 110^\circ$ they are associated with the passing of weather systems characterized by condensate clouds and higher wind speeds.

Phoenix observed the first snow fall on Mars as fall streaks from water-ice condensate clouds. Atmospheric water content dropped at earlier hours than could be explained by condensation. Two possible hypotheses are hydration of perchlorate molecules or multi-layer adsorption of water molecules onto surface grains. No aeolian activity was recorded at the Phoenix landing site besides dust devils. This is probably due to the presence of cloddy soils and the ongoing surface modification caused by the freeze-thaw cycle of the ice-cemented soils.

During the Phoenix mission it was observed that the contrast in images of the Telltale fibres changed with time possibly due to time dependent accumulation and removal of atmospheric dust on the fibres. Measured wind speeds were below the threshold for dust detachment, however passing dust devils could exceed this. Experiments showed that wind speeds of less than 10 m/s were needed indicating the formation of sand-sized dust agglomerates which have a lower threshold wind speed. Dust devils are still the most likely cause for the massive dust removal around $L_s \sim 120^\circ$. The experiment verifies that no high wind speed events were missed in the intermittent Telltale data.

Electric fields have been measured in naturally dust lifting phenomena on Earth and are believed to be present on Mars. Experiments have shown that electric field assisted detachment is dependent on the electrical properties of the surface. Detachment is aided by conductive surfaces and hindered by insulating surfaces. The low conductivity of the Martian regolith should thus further inhibit aeolian movement. It is hypothesized that global dust storms could be a consequence of a significantly elevated conductivity in the southern polar regions by sub surface liquid water.

Resumé

Analyser af data fra NASA Phoenix Mars missionen og eksperimenter udført i laboratorierne ved Aarhus Universitet er blevet kombineret for at undersøge visse aspekter af den vind relateret udvikling af Mars' overflade.

De første meteorologiske målinger i de nordlige polære egne af Mars blev udført i løbet af Phoenix missionen. Vind hastigheder og retninger blev målt af en mekanisk vindmåler, kaldet Telltalen, ved at analysere billeder taget med det ombordværende kamera. Af andre meteorologiske instrumenter kan nævnes en tryk måler, tre temperaturmålere og en LIDAR. De blev suppleret af målinger fra Surface Stereo Imager så vel som koordinerede målinger mellem Phoenix landeren og instrumenterne ombord på Mars Reconnaissance Orbiter (MRO). Vejrets daglige rytme blev karakteriseret ved rolige natlige forhold og tilstedeværelsen af konvektiv turbulens i dagtimerne. Telltale vind data indikerer at Heimdall krateret er kilden til den natlige turbulens i temperaturen. Sæsonmæssig variation reflekteredes i øget gennemsnitlig vind hastigheder, vind retninger fra vest gennem hele dagen og faldende temperaturer og tryk.

Observationer foretaget af Mars Color Imager på MRO og med Telltalen antyder at der er to forskellige mekanismer der styrer støv løftnings begivenhederne som påvirker Phoenix landingsstedet. Før $L_s \sim 95^\circ$ var de associeret med fordampningen af den sæsonbestemte CO_2 is, men ikke med øgede vind hastigheder. Efter $L_s \sim 110^\circ$ var de associeret med forbigående vejr systemer karakteriseret ved kondensat skyer og øget vind hastigheder.

Phoenix observerede det første snefald på Mars fra vand-is kondensat skyer. Atmosfærisk vand indhold dalede flere timer tidligere end kondensering kunne forklare. To muligheder er hydrering af perklorat molekyler eller adsorption af flere lag af vand molekyler på overflade partikler. Ingen vindreven aktivitet blev observeret ved Phoenix landingsstedet på nær støv djævla. Dette kan være på grund af tilstedeværelsen af klumpet jord og den igangværende modificering af overfladen fra den årlige frys-tø cyklus af den is-cementeret jord.

I løbet af Phoenix missionen blev det observeret at kontrasten af Telltale snoren i billeder ændres med tiden, muligvis pga. en tidsafhængig ophobning og fjernelse af atmosfærisk støv på snoren. Målte vind hastigheder var under grænseværdien for støv frigørelse fra overflader, men forbigående støv djævla kan komme over denne grænse. Eksperimenter viste at vind hastigheder mindre end 10 m/s var nødvendige, hvilket indikerer dannelsen af sand-størrelse støv agglomerater, der har en lavere grænseværdi. Støv djævla er stadigvæk den mest sandsynlige forklaring på den massive støv fjernelse omkring $L_s \sim 120^\circ$. Eksperimentet verificerede at ingen høje vind hastigheder var udeladt fra det uregelmæssige Telltale datasæt.

Elektriske felter er blevet målt i naturligt forekomme støv løftnings fænomener på Jorden, og menes at være tilstede på Mars. Eksperimenter har vist at elektrisk felt assisteret frigørelse afhænger af overfladens elektriske egenskaber. Frigørelsen hjælpes af ledende overflader og hindres af isolerende overflader. Den lave konduktivitet af Mars' øverste jordlag burde hæmme vindreven aktivitet. Det foreslås at de globale støvstorme kunne være en konsekvens af en signifikant øgning i konduktiviteten grundet flydende vand under overfladen i de sydlige polære egne.

Part One
Background

Chapter 1 - Introduction to Mars

Mars has held the fascination of mankind since ancient times with its red color shining brightly in the night sky. As the first telescopes were pointed to the planet they revealed a planet with a mean radius about half the size of Earth (3390 km), a surface gravity of a mere one third of Earth's (3.71 m/s^2), a year almost twice as long (687 Earth days), but with a day length similar to Earth of 24h 37min [Kieffer et al., 1992, Mars Factsheet]. Popular belief was that Mars would resemble a small Earth with canals of water, civilized cities and vegetation [Kieffer et al., 1992]. These myths were laid to rest with the technical advances in observing techniques in the 20th century combined with the discoveries of the many successful Mars missions listed in Table 1.1. A gap of two decades separate the groundbreaking early Mars missions from the highly successful contingency of newer Mars missions.

A total of six landers have managed to send back scientific data from Mars. The Soviet lander Mars 3 only lasted 20 s, too short to send back any scientific data [Kieffer et al., 1992] and contact was lost with Beagle 2 upon separation from the orbiter [Beagle]. The landing sites for the remaining six landers are plotted in Fig. 1.1. The majority landed between 30°N and 30°S with only Viking Lander 2 and Phoenix in the northern lowlands. The Phoenix mission and its results will be discussed in Chp. 4.

Table 1.1 Overview of all successful Mars missions sorted by launch year. Intervals indicate operation time at Mars beyond the launch year. Far right are the regularly used abbreviations. Missions launched before 1980 are referred to as "early Mars missions". Landers and their end of operation year are indicated in bold [NASA- missions].

1964 (flyby)	Mariner 4	
1969 (flyby)	Mariner 6	
1969 (flyby)	Mariner 7	
1971	Mars 3 Orbiter/ Lander	
1971 - 1972	Mariner 9	
1973	Mars 5	
1975 - 1980/ 82	Viking 1 Orbiter/ Lander	(VL1)
1975 - 1978/ 80	Viking 2 Orbiter/ Lander	(VL2)
1996 - 2007	Mars Global Surveyor	(MGS)
1996	Mars Pathfinder	(MPF)
2001 - present	Mars Odyssey	(ODY)
2003 - present	Mars Express Orbiter/ Beagle 2 Lander	
2003 - present	Mars Exploration Rover - Spirit	(Spirit)
2003 - present	Mars Exploration Rover - Opportunity	(Opportunity)
2005 - present	Mars Reconnaissance Orbiter	(MRO)
2008	Phoenix Mars Lander	(PHX)

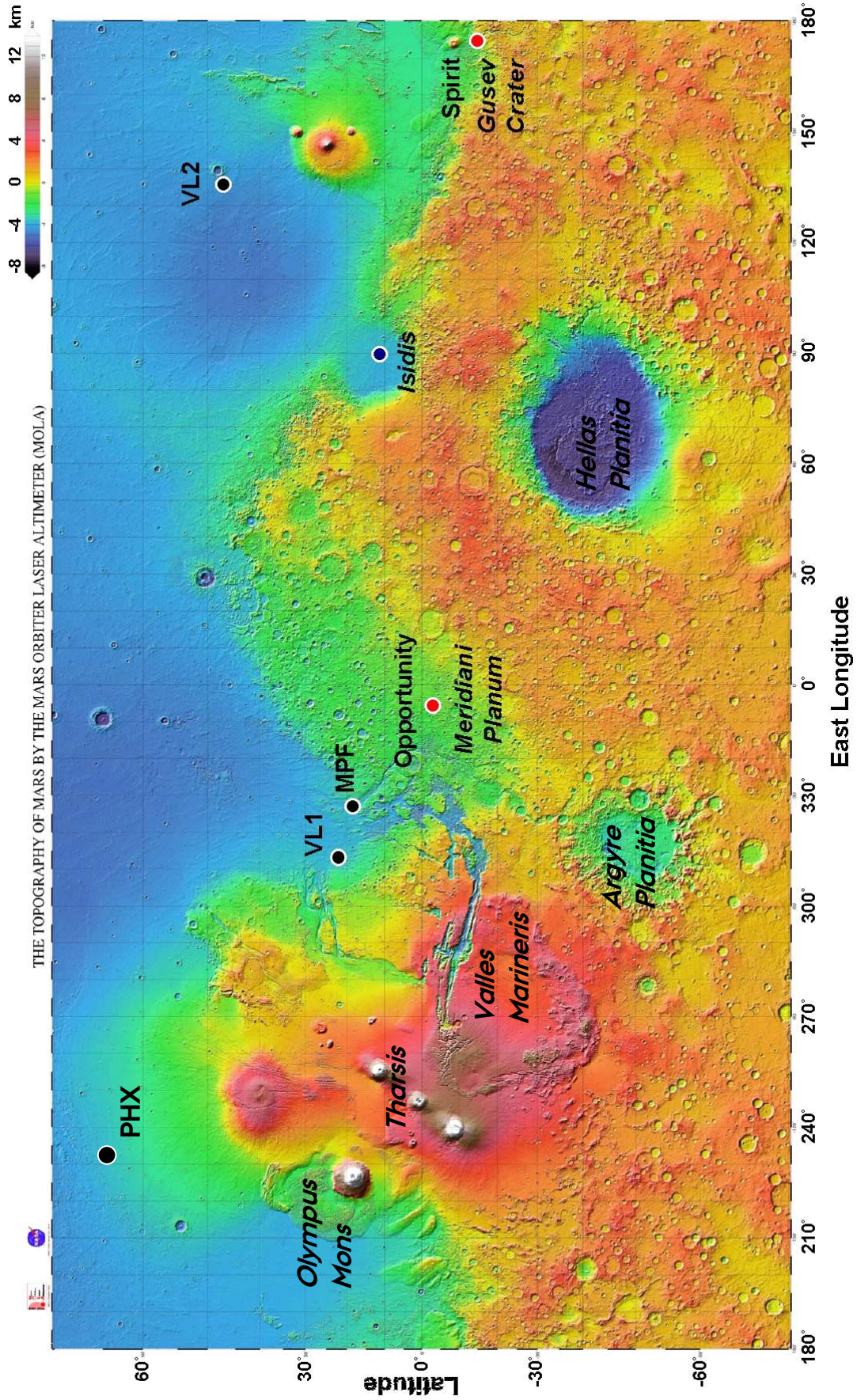


Fig. 1.1: Overview of the landing sites on Mars overlaid on a high resolution topographic shaded relief map made from data from the Mars Orbiter Laser Altimeter (MOLA) onboard the Mars Global Surveyor. Beagle 2 is suspected to have landed at the Isidis Plateau. [NASA landing sites]

The first views of the Martian surface in 1964 by Mariner 4 showed a lunar-like surface [Kieffer et al., 1992] quite unlike anything expected by people of Earth proving that Mars was indeed an alien world. Topographical maps, as in Fig. 1.1, display the dichotomy of the Martian surface where the highly cratered southern hemisphere is 3 to 6 km above the reference gravity equipotential surface and the quite smooth northern hemisphere is 1 to 3 km below the equipotential surface [Lindal et al., 1979].

With the landing of the highly successful Viking missions in 1975, color images showed a barren, rock-strewn surface (cf. Fig. 1.2), a sight which is repeated everywhere on Mars only interrupted by the polar ice caps. Dust covers the surface providing the red coloring of the regolith which is topped by a dust-colored orange-reddish sky. Mean annual temperature was measured to be 213-220 K with variations due to diurnal and seasonal cycles as well as latitude [Gierasch, 1974, Snyder, 1979, Ryan, 1979, Larsen et al., 2002].

A day, or a “sol”, on Mars lasts 24h 37min with 667 sols (or 686.98 Earth days) to a Martian year. Mars experiences four seasons due to its axial inclination of 25.2° which is similar to Earth’s [Larsen et al., 2002], however the seasons are not of equal length since Mars has a more elliptical orbit than Earth. Months and seasons on Mars are defined using degrees of solar longitude, L_s , defined as the angle of Mars’ position in its orbit relative to its position at northern hemisphere spring equinox (cf. Fig. 1.3). Mars’ closest approach to the Sun happens at perihelion corresponding to southern summer.



Fig. 1.2: Panorama image taken by the Viking 2 lander showing the meteorological boom hovering above the rock-strewn surface [VIK].

1.1 The Martian atmosphere

The measurements of early Mars missions laid the foundation for our understanding of the Martian atmosphere. Earthbound observations in the 20 years predating Mariner 4’s arrival at Mars detected the presence of carbon dioxide (CO_2) in the atmosphere and calculated surface pressures of 24-85 mbar. Mariner 4 revealed an atmosphere with pressures as low as 4.1 – 7 mbar and CO_2 as the major component [Kieffer et al., 1992]. Today we know that CO_2 constitutes 95.3 % of the atmosphere with nitrogen, argon, oxygen and water as minor components (< 2%) [Larsen et al., 2002]. The low content of water in the atmosphere is no hindrance for precipitation and many Mars

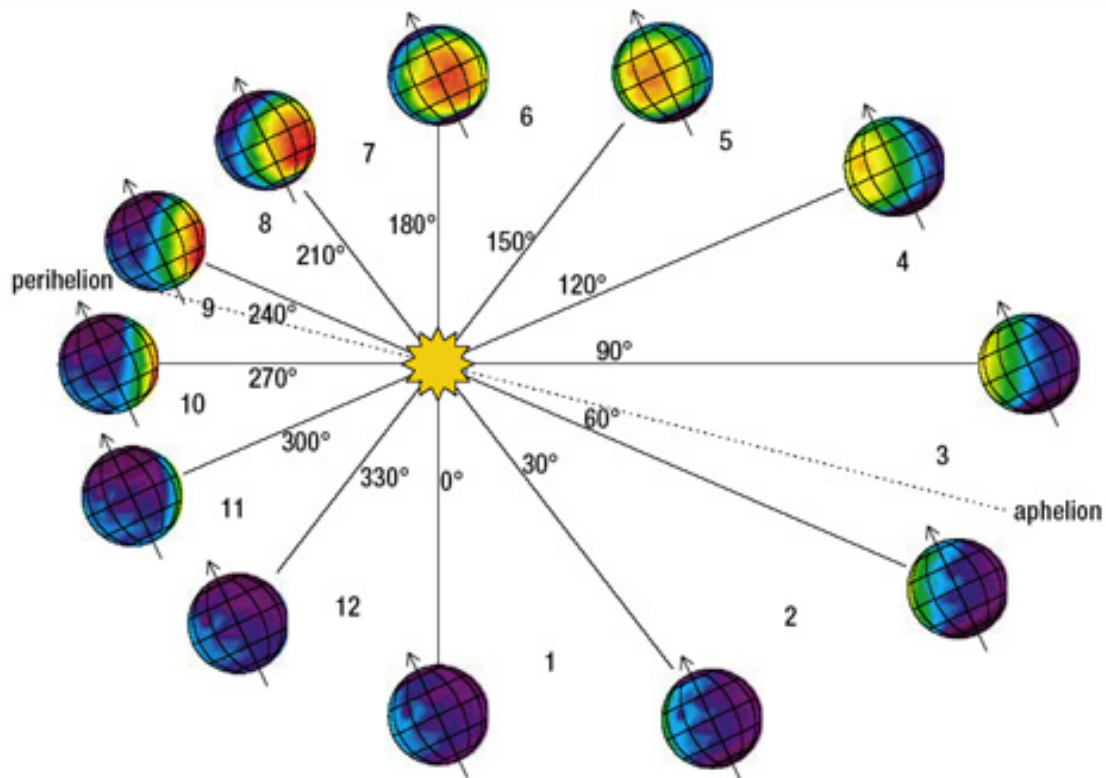


Fig. 1.3: Mars' orbit around the Sun with solar longitudes indicated in degrees. Mars' closest approach to the Sun happens at perihelion and Mars is furthest from the Sun at aphelion. The numbers refer to a division of the orbit into twelve months of unequal length due to the elliptical orbit. The beginnings of the seasons in the northern hemisphere are $L_s = 0^\circ$ for northern spring, $L_s = 90^\circ$ for northern summer, $L_s = 180^\circ$ for northern autumn and $L_s = 270^\circ$ for northern winter [ESA seasons].

missions have observed clouds of dust and water-ice as well as ground fogs [Briggs et al., 1977, Pollack et al., 1977, Kieffer et al., 1992].

1.1.1 Atmospheric carbon dioxide

The importance of carbon dioxide to the Martian atmosphere was highlighted with the exploration of the Martian polar caps. In 1969 Mariner 6 and 7 recorded surface temperatures of 150 K, consistent with CO_2 ice, disproving the long-held beliefs of pure water-ice polar caps [Kieffer, 1992]. Follow-up measurements were made by Mariner 9 in 1972 indicating that the polar ice caps must be composed of permanent water-ice caps with seasonally dependent CO_2 ice caps [Kliore et al., 1973]. In 1976 the two Viking missions, each composed of a lander and an orbiter, arrived at Mars. Analysis of pressure measurements made by the two landers over a full Martian year showed that the range in atmospheric pressures measured by Mariner 4 was highly dependent on the seasonal CO_2 ice caps. The large dip in atmospheric pressure at $L_s \sim 150^\circ$ (cf. Fig. 1.4) coincides with maximum accumulation of CO_2 in southern winter which severely depletes the atmosphere. The subsequent sublimation of CO_2 in southern spring leads to an increase in pressure, followed by a smaller dip in pressure at the maximum accumulation of CO_2 at the end of northern winter [Hess et al., 1979, Leovy 1979].

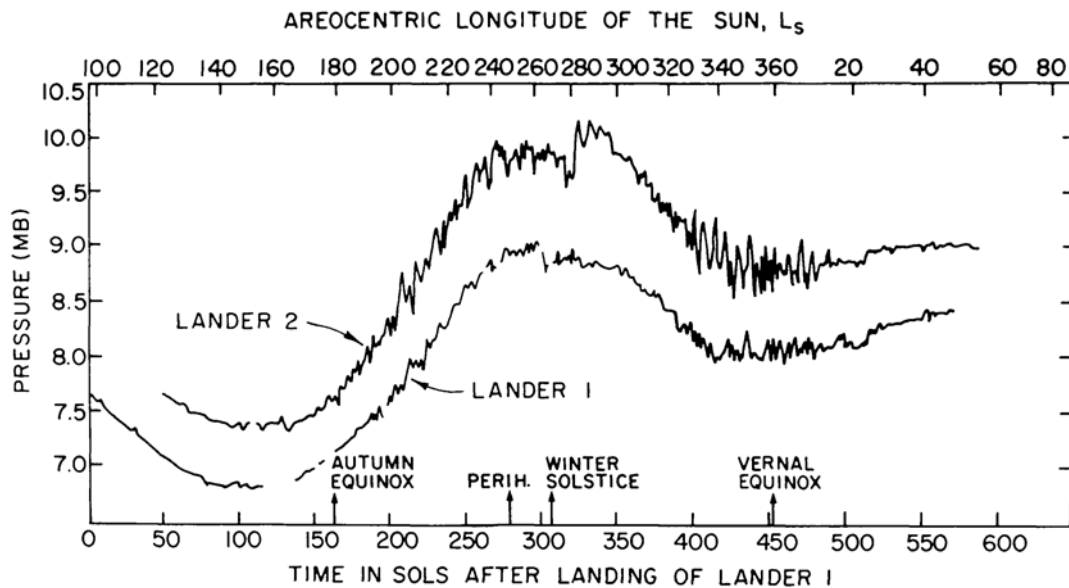


Fig. 1.4: Daily average surface pressures as measured at the Viking Lander 1 and 2 sites with perihelion (southern spring equinox) of the Martian orbit indicated (Perih.) [Leovy, 1979]. Sol refers to one day on Mars.

1.1.2 Atmospheric dust

The Martian atmospheric pressure jump at $L_s \sim 280^\circ$ is an indicator of the occurrence of important surface to atmosphere interactions. The jump is a reaction to the second of two planetwide dust storms observed and experienced by the Viking landers. The first occurred at $L_s \sim 205^\circ$ and is not clearly visible in the data [Leovy, 1979]. A planetwide dust storm was also active as Mariner 9 arrived to Mars [Gierasch, 1974] but no surface pressures could be recorded. Mariner 9 observed an atmospheric temperature increase of about 50 K from the average [Gierasch, 1974] and the Viking landers saw surface maximum and minimum temperatures approach one another [Ryan and Henry, 1979] as a result of these of the insulation caused by the airborne dust in the dust storms.

The Martian atmosphere is always dust-laden to some extent as illustrated in Fig. 1.5, with the reddish atmosphere resembling the color of the regolith. Analyses of atmospheric and surface observations from various Mars missions have shown that the atmospheric dust has diameters of 1-5 μm [Conrath et al., 1973, Tomasko et al., 1999, Lemmon et



Fig. 1.5: Color composite image from Viking Orbiter 1 showing Galle crater in the foreground. Between the surface and space is the thin sliver of the dust-filled Martian atmosphere.

al., 2004] whereas the regolith particles have diameters of minimum 50 μm [Cabrol et al., 2008, Sullivan et al., 2008, Goetz et al., 2010]. The inconsistency in particle sizes is one of the fundamental issues of windblown activity on Mars and is intimately linked to the issues on particle entrainment by wind discussed in the next chapter.

Chapter 2 - Windblown sand and dust

Working with *aeolian* (wind-driven) particle movement on planetary bodies with atmospheres requires an understanding of the physics governing their mobilization and transportation. The similarities between Earth and the other planetary bodies in our Solar System mean that many of the equations and theories are easily transferred. However, caution must be exercised in doing so, since empirical studies have been the basis for many relevant theories. This chapter will introduce the relevant theories and equations regarding particle movement under the influence of wind with specific attention to Mars. This will form the basis on which to understand the results from decades of Mars observations and the experiments conducted during this thesis.

2.1 Planetary boundary layers

Planetary atmospheric structure and dynamics are governed by *e.g.* temperature, gravity and fluid density resulting in quite different atmospheres for the various planetary bodies. When making planetary comparisons of atmospheric flows the Reynolds number can reveal whether or not the flows are dynamically similar and thus comparable [Greeley and Iversen, 1985]:

$$\text{Re} = \frac{UL}{\nu} = \frac{\rho UL}{\mu} \quad (2.1)$$

Here ρ is the atmospheric density, U is a characteristic velocity scale, L is a characteristic length scale, ν is the kinematic viscosity and μ the molecular viscosity. The Reynolds number is a measure of the ratio of the inertial forces to the forces caused by viscosity. High values of Re indicate turbulent flow, whereas smaller values correspond laminar flow [Salby, 1996].

The planetary boundary layer is an inherently turbulent layer which forms the connection between the atmosphere and surface enabling the transportation of material and energy [Salby, 1996]. Turbulence is generated at the ground and maintained in the boundary layer under specific atmospheric conditions. At the ground there is a strong shear as the wind flow adjusts to satisfy the no-slip condition, meaning there is no wind velocity at ground level [McIlveen, 1992]. As the air parcels experience this shear stress they are set in rotation becoming turbulent eddies, which are responsible for the turbulent transport. Turbulence is maintained through continuous production of eddies by the wind shears as well as disturbances in the wind flow by turbulence itself, thus giving rise to turbulent motion even in short absences of wind flow. Thermally-driven convection will either reinforce the turbulent eddies during unstable atmospheric conditions (*e.g.* daytime) or dampen out the turbulence under stable conditions (*e.g.* at night) [McIlveen, 1992, Salby, 1996].

At the surface, the creation of turbulence entails that there exists a very shallow laminar surface layer wherein the surface shear stress is defined as [Greeley and Iversen, 1985]:

$$\tau = \rho u_*^2 \quad (2.2)$$

The friction velocity, u_* , is not a true wind speed as much as a reflection of the turbulent shear. It is comparable to the vertical component of the fluctuating turbulent wind speed, which is responsible for keeping particles airborne [Greeley and Iversen, 1985]. The shear stress is responsible for particle detachment thus the friction velocity is a threshold wind speed used for comparison with measurements when examining the onset of aeolian activities.

The wind shear diminishes with increasing height creating a wind gradient which becomes a logarithmic function of height when τ and ρ are uniform through the boundary layer [Greeley and Iversen, 1985, McIlveen, 1992]:

$$\frac{U}{u_*} = \frac{1}{\kappa} \ln\left(\frac{z}{z_0}\right) \quad (2.3)$$

where U is the mean wind speed parallel to the surface, κ is von Karman's constant usually taken as 0.4 and z is the measuring height above the surface. z_0 is the surface roughness height which is usually on the scale of a few to several millimetres. It characterizes the surface and is a function of the shape of the surface elements as well as the average distance between them. The Viking landers, Mars Pathfinder and the Phoenix Mars mission have measured roughness heights between 5 mm and 3 cm corresponding to regions with a low quantity of smaller rocks to regions with a greater quantity of larger rocks [Tillman et al., 1994; Sullivan et al., 2000, Holstein-Rathlou et al., 2010].

Eq. (2.3) can be used to determine u_* and z_0 experimentally by measuring wind speeds at several different heights above the surface. Plotting wind speeds as a function of height in a semi-log diagram results in a straight line where z_0 is the intercept and the slope is inversely proportional to u_* . The method was used by the Mars Pathfinder mission which has been the only Mars lander designed to measure wind speeds at several heights [Sullivan et al., 1996, 2000]. Determining these parameters from wind speeds at only one height requires alternative methods involving *e.g.* heat fluxes and turbulence in the wind speeds, as done by the Viking and Phoenix lander(s) and will not be discussed further [Sutton et al., 1978, Holstein-Rathlou et al., 2010].

2.2 Particle transport modes

Fig. 2.1 illustrates the three principle modes of transportation for surface particles. Particles are lifted from the surface due to the surface shear stress exerted by the wind gradient (A). Once airborne, particles are accelerated downward by the force of gravity until they reach their terminal speed at which the drag force is equal to the weight of the particle. When the terminal speed exceeds the friction speed, gravity will carry the particle smoothly to the surface where it may impact other particles of similar or larger sizes and return to flight. This motion of "leaping" is called *saltation* (B-D). Similar sized particles may become saltating particles by ejection from the surface upon impact, a process called "splash" (D). Saltating particles may eject smaller sized particles

for which the friction velocity becomes larger than the terminal velocity and the turbulent eddies of the atmosphere will keep the particles in *suspension* (E) allowing them to travel to much higher altitudes than the saltating particles. Finally there are the particles too large for wind to lift, which move by *creep* as they are hit by saltating particles (F) [Greeley and Iversen, 1985].

From a meteorological perspective particle types are defined by their modes of transportation. Particles which can be suspended are termed *dust* while particles which saltate are termed *sand*. The particles which undergo creep are not directly relevant to this work, and will not be dealt with further. On Earth sand is empirically defined as particle sizes of 63 μm -2mm, with dust being finer material [Sullivan et al., 2008].

Experimental research has examined the threshold friction speed, or dynamic threshold, required for the onset of saltation under various Mars like atmospheric conditions for various sizes of sand grains with different diameters [Greeley et al., 1980]. Analysis produced a semi-empirical expression for the threshold parameter for various ranges of the friction Reynolds number:

$$\text{Re}_* = \frac{\rho u_* d_p}{\mu} \quad (2.4)$$

where d_p is the particle diameter. For values of the Reynolds number between 0.3 and 10 the dependency of the threshold friction speed for saltation on particle diameter was calculated for Earth, Mars, Venus and Titan (cf. Fig. 2.2) [Greeley and Iversen, 1985]. For Mars the optimum friction wind speed for the onset of saltation is about 2 m/s for particles diameters of 115 μm . Particles smaller than this are bound more strongly to the surface by adhesive forces while larger particles are more difficult to lift due to the force of gravity. The

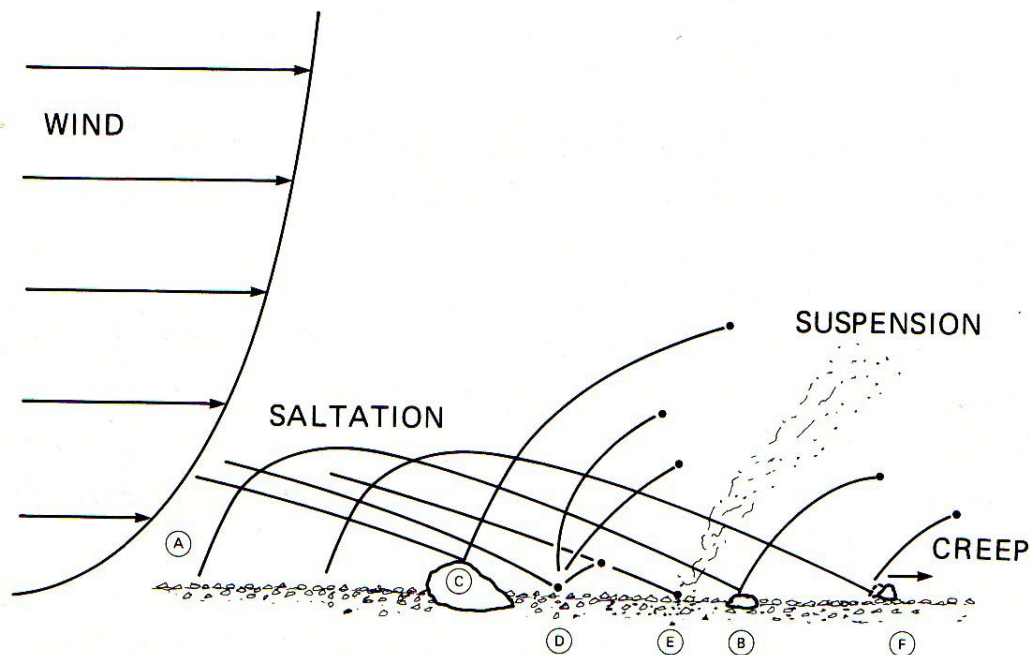


Fig. 2.1: Diagram showing the three principal modes of aeolian transport of grains; saltation, suspension and creep [Greeley and Iversen, 1985].

friction speed can be translated to a mean wind speed (at measuring heights of 1.5 to 2 m height) by means of the logarithmic wind profile (Eq. (2.3)). With roughness heights between 5mm and 3 cm this results in wind speeds of 20 to 30 m/s for the onset of saltation.

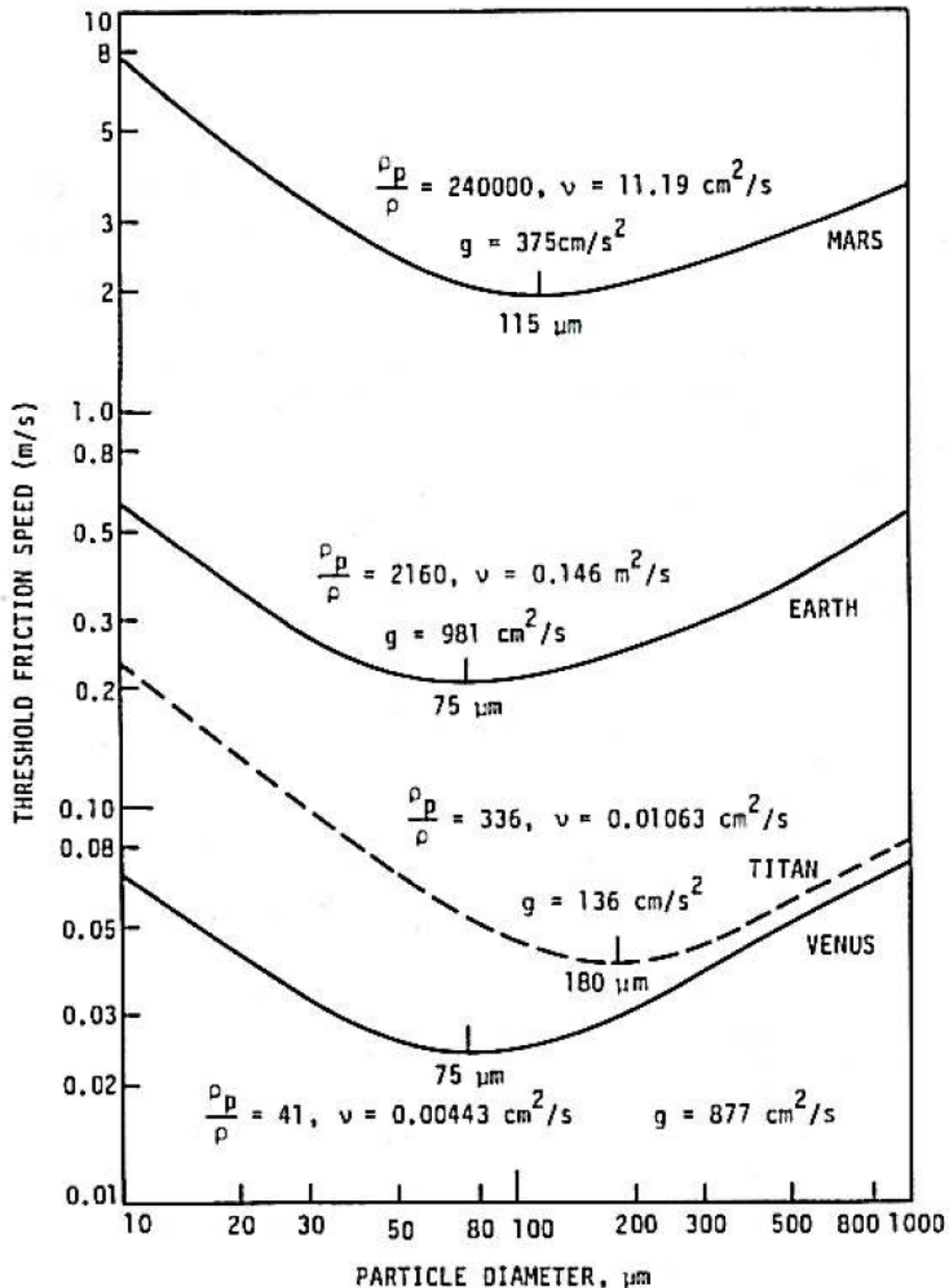


Fig. 2.2: Threshold friction speed as a function of particle diameter calculated for Mars, Earth, Venus and Saturn's moon Titan. ρ_p is the particle density, ρ is the atmospheric density, g is the gravitational constant and ν is the atmospheric viscosity [Greeley and Iversen, 1985].

Three missions have made in-situ measurements of wind speeds on the surface of Mars, namely the Viking landers, Mars Pathfinder and the Phoenix mission. The wind speeds from Mars Pathfinder have not been analyzed [Schofield et al., 1997] although wind profile measurements hinted at wind speeds generally below 6 m/s [Sullivan et al., 2000]. Of the remaining two missions, daily average wind speeds were of the order 2 to 12 m/s with a maximum measured wind speed from the Phoenix mission of 16 m/s not associated with a storm [Hess et al., 1977, Holstein-Rathlou et al., 2010]. The Viking landers measured wind gusts of about 25 m/s during dust storms [Ryan and Henry, 1979], but high wind events such as these are rare [Sullivan et al., 2008]. Saltation should thus be expected to be an infrequent event, however, once started saltation can be self-sustaining and the transport rate is highly nonlinear allowing the process to transport large amounts of material during short periods of activity [Bagnold, 1941]. The process of saltation induced dust entrainment is not capable of explaining the regular and persistent entrainment of dust seen in the Martian atmosphere or the mechanisms of dust devil formation [Ferri et al., 2003, Greeley et al., 2003]

2.3 Surface particle detachment

Initiation of saltation requires the wind induced detachment of sand sized surface particles. This is referred to as the static threshold and is higher than the wind speed required to maintain active saltation, referred to as the dynamic threshold. The difference is due to the process of “splash” where sand grains returning to the surface can eject secondary particles thus maintaining transport. Previous work on saltation has shown that the dynamic threshold is about 20% lower than the static threshold. On Earth it is typically understood that the entrainment of dust happens as a result of the splash events occurring during saltation which can eject dust grains [Bagnold, 1941]. However, dust transport on Mars is observed at wind speeds below the saltation threshold and dust is observed to be removed from sand beds without disturbing them (more in Chp. 3). Another transport mechanism is required to explain these phenomena.

One possible transport mechanism involves the aggregation of dust, a process in which dust sized surface particles loosely collect into sand-sized surface particles possibly under the influence of electrostatics [Greeley, 1979, Merrison et al., 2004]. The reduced mass density of these aggregates should allow for easier detachment under the influence of wind. Aggregates lifted into suspension are seen to readily break apart [Merrison et al., 2007] resulting in large amounts of dust particles being airborne without the need for saltation. The physics governing surface particle detachment was studied in detail by Merrison et al. [2007] and will be summarized in this section.

Fig. 2.2 illustrates the four forces affecting the detachment of spherical surface particles under the influence of a wind gradient generated in the surface boundary layer. The wind shear generates two components of force, specifically lift (F_l) and a moment of torque (F_T) which acts to remove the particles. These are counteracted by the gravitational force (F_g) and inter particle adhesive (F_{ad}) forces which keep the particle anchored:

$$F_g + F_{ad} = F_T + F_l \quad (2.5)$$

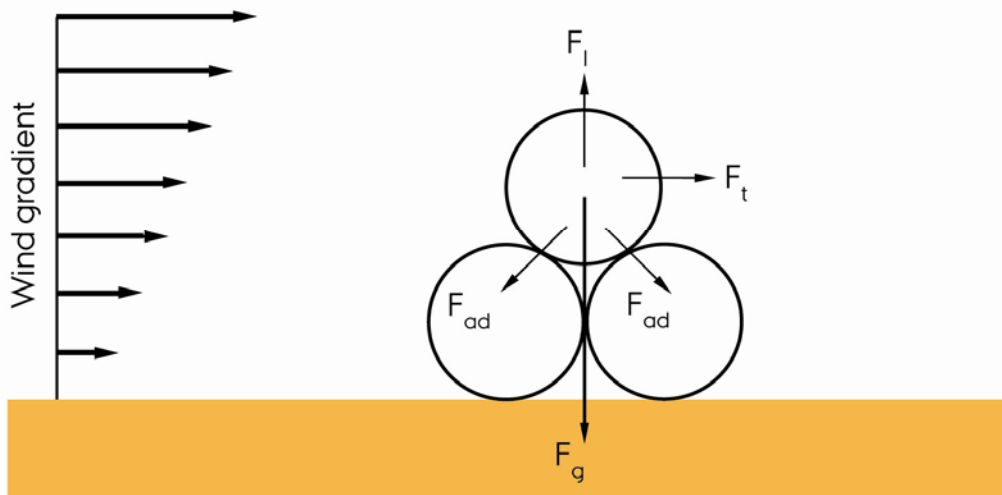


Fig. 2.2: An illustration of the forces acting upon particles situated on the surface with wind blowing by. F_g is the gravitational force, F_{ad} is the inter particle adhesive force, F_l is the lift caused by the wind and F_T is the moment of torque caused by the wind.

2.3.1 Gravitational force

The gravitational force for a spherical particle of radius r , or diameter d , is easily described theoretically:

$$F_g = mg = V\rho_{par}g = \frac{4}{3}\pi r^3\rho_{par}g = \frac{\pi}{6}g\rho_{par}d^3 \quad (2.6)$$

where m is the particle mass, V the particle volume and g is the gravitational acceleration. ρ_{par} is the particle density, which on Mars is based on best estimates for the bulk densities of the surface materials encountered by the Viking mission. It was estimated to be between 1.1 and 2.6 g/cm³ with an average of 1.6 g/cm³ [Moore and Jakosky, 1989]. When simulating Martian surface materials on Earth, experiments must compensate for the reduced gravity, which can be achieved by choosing lower density particles. Merrison et al. [2007] chose glass spheres of 2.7, 0.6 and 0.15 g/cm³ which correspond to, respectively, common quartz particles on Earth, the average bulk material density on Mars, and a mass density which simulates dust aggregates under Martian conditions (0.4 g/cm³).

2.3.2 Adhesive force

Inter-particle adhesive forces are the combination of van de Waal forces, electrostatic forces as well as liquid (water) and chemical bonding [Shao and Lu, 2000]. Adhesive forces are seen to have a linear dependency on particle diameter, leading to the general expression:

$$F_{ad} = C_{adh}d \quad (2.7)$$

where C_{adh} is the adhesion coefficient.

2.3.3 Drag force

The drag force is a wind-induced force responsible for both the lift and torque on a stationary surface particle, as well as being the opposing force to gravity for a particle in free fall. It is ordinarily given by:

$$F_{drag} = \frac{1}{2} C_d \rho u^2 A \quad (2.8)$$

where ρ is the density of fluid, in this case an atmosphere, C_d is the drag coefficient, u is the mean wind speed and A is the characteristic area affected. The drag coefficient for a spherical particle is dependent on the Reynolds number as displayed in Fig. 2.3.

For small Reynolds numbers ($Re < 1$) we are in the Stokes regime, where there exists a linear relationship as given by Stokes law [Fox and McDonald, 1985] leading for example to a linear relationship between settling rate and grain size for fine particles [Greeley and Iversen, 1985]. For $Re > 5000$ we have Newtonian flow where the drag coefficient can be approximated to a constant value. Between these two regimes the relationship is an unknown function of fluid density, viscosity and characteristic sizes and lengths. This is the regime one often works in when dealing with sand sized particles at detachment wind speeds on both Earth and Mars. To accommodate for this case, the drag force should be expressed by a power law:

$$F_{drag} = C_d' \rho^{1-n} u^{2-n} d^{2-n} \quad (2.9)$$

where n can be an empirical fitting parameter.

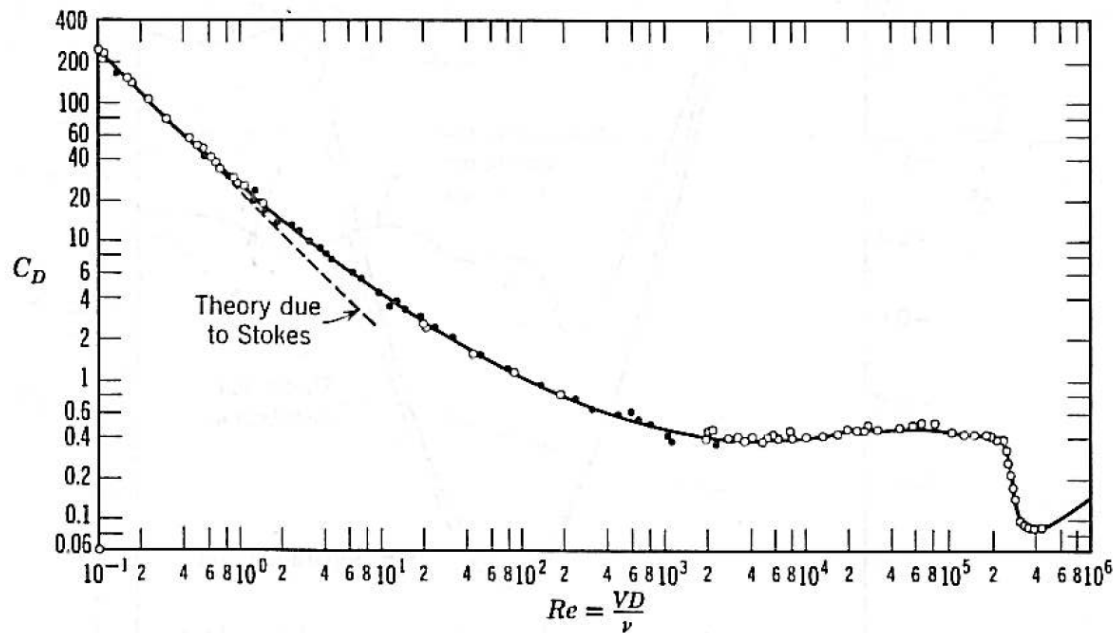


Fig. 2.3: The drag coefficient of a sphere as a function of Reynolds number [Fox and McDonald]

2.3.4 Lift force

The lift force is a result of the drag which despite many efforts has not been accurately determined [Greeley and Iversen, 1985]. It can be modeled empirically in the same manner as the drag force using a coefficient of lift instead of drag:

$$F_L = C_L \rho^{1-n} u_*^{2-n} d^{2-n} \quad (2.10)$$

2.3.5 Moment of torque

The wind gradient will enforce a differential drag force over the height of a particle leading to a torque. The torque is calculated as a length scale, which is about a particle diameter, multiplied by the drag force:

$$F_T = C_T \rho^{1-n} u_*^{2-n} d^{3-n} \quad (2.11)$$

C_T is thus a coefficient of torque to be determined experimentally.

2.3.6 Results

By equating the wind forces (*i.e.* drag and lift) to those of gravity and adhesion an expression for the wind induced threshold for lifting spherical particles emerges:

$$\rho^{1-n} u_*^{2-n} \approx \frac{\frac{\pi}{6} g \rho_{par} d^3 + C_{adh} d}{C_L d^{2-n} + C_T d^{3-n}} \quad (2.12)$$

where the left side is an expression for the threshold shear stress, τ , exerted on the surface by the horizontal wind component. The various constants of force as well as the precise power law dependencies should be determined experimentally.

Merrison et al. [2007] performed experiments at 30 mbar with atmospheric air and under Martian conditions at 6-30 mbar CO₂ gas at -14°C. The results obtained for both cases were similar, displaying a decrease in the shear stress needed for detachment of aggregates. Applying the results to Martian surface conditions of 9 mbar pressure, temperature of -60°C and using a surface roughness height of 3 mm and a measuring height of 1.6 m produced Fig. 2.4. The detachment wind speed for aggregates is about a third of that for solid sand particles which places it in the range of the higher wind speeds measured on Mars making dust aggregation a plausible transport mechanism on Mars. The values for surface shear stress at which dust entrainment occurs for this aggregate model can be calculated to be about 0.01 N/m², which also agrees with values used in global (and mesoscale) circulation modelling for dust lifting [Newman et al., 2005].

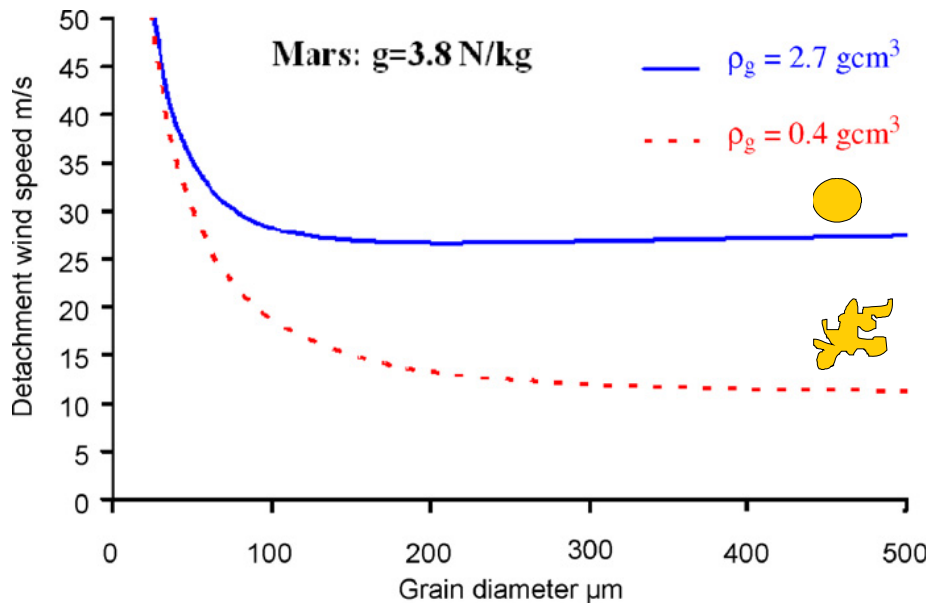


Fig. 2.4: Predictions of the detachment threshold wind speed on Mars measured at 1.6 m height, assuming a pressure of 9 mbar, a temperature of -60°C and a surface roughness of 3 mm [Merrison et al., 2007]

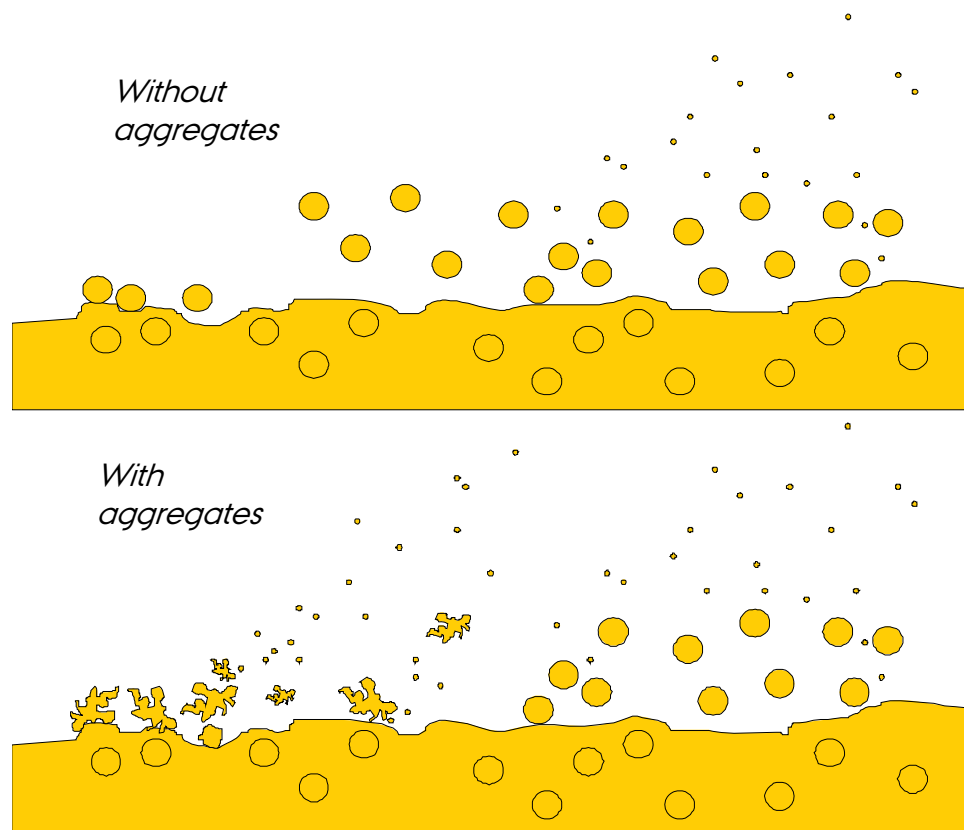


Fig. 2.5: (Upper) The conventional picture of particle transportation on Mars with sand particles being lifted through high wind speeds. The onset of saltation lifts more sand and suspends dust. **(Lower)** A new look at particle detachment when aggregates are included. Aggregates are lifted by lower wind speeds and will break apart in the atmosphere decomposing into their original dust particles. This will add dust to the atmosphere much more readily than saltation [Merrison, private communication].

2.4 Modification to particle transportation modes

With the addition of the dust-aggregates model to describe dust entrainment the picture of aeolian dust movement can now be redrawn to resemble Fig. 2.5. This is a modification of the standard model for dust transport used on Earth (Fig. 2.1) which is more likely to describe Martian aeolian activity. It is still unclear whether the model for saltation on Mars also requires modification as some theoretical work suggests the enhanced affect of “splash” may reduce the dynamic saltation threshold drastically [Almeida et al., 2008, Kok, 2010]

Chapter 3 - Aeolian Mars

Aeolian activity on Mars is not easily understood as hinted in the previous chapter. Larger events, such as dust storms and dust devils, are observed along with numerous variations of aeolian surface features. They are found planet-wide in a variety of shapes and sizes and can reveal information regarding the past and current history of aeolian activity on Mars.

3.1 Dust storms

The most prominent aeolian phenomenon is undoubtedly the dust storms which could be seen by early earthbound telescope observations from Earth as color changes to the Martian surface [Kieffer et al., 1992]. During the time of spacecraft observation five planet-wide dust storms have been observed [Gierasch, 1974, Martin, 1974, Snyder, 1979, Smith et al., 2002] all lifting large quantities of dust into the atmosphere (cf. Fig. 3.1). The Viking landers have measured wind speeds of up to 25 m/s in such storms [Ryan and Henry, 1979], making it likely that saltation can be activated and play a major role in dust loading of such storms.

All observed planet-wide dust storms occur with the recession of the south polar ice cap, close to the time of maximum solar influx to the southern hemisphere (perihelion) [Martin and Zurek, 1993]. As a consequence this time of year has been dubbed “dust storm season” [Zurek and Martin, 1993]. They seem to develop from regional dust storms in the southern hemisphere but the mechanism for going from regional to global storms is unknown [Strausberg et al., 2005]. Regional and local dust storms are seen to develop regularly in both hemispheres on Mars though most commonly in the southern and no planet-wide dust storm has been seen to develop from dust storms in the northern hemisphere [Martin and Zurek, 1993].

3.2 Dust devils

On a smaller scale of dust phenomena we find the dust devils, or thermal vortices, which are whirlwinds made visible by entrained dust [Balme and Greeley, 2006]. Their cores have a lower pressure and higher temperature than the surrounding air [Ferri et al., 2003, Ellehøj et al., 2010] and on Mars they can reach sizes up to a few kilometres height and hundreds of meters in diameter [Thomas and Gierasch, 1985, Stanzel et al., 2008].

They were first “detected” by temperature, pressure and wind speed changes in the meteorological observations made by the Viking landers, thus inferring their passage [Ryan and Lucich, 1983]. As a dust devil passes the instruments measure increased wind speeds and large, rapid wind direction change from the edges, followed by the pressure drop and temperature rise in the center [Rayn and Lucich, 1983, Balme and Greeley, 2006].

As they speed along the surface, they entrain dust implying that the horizontal wind speeds at the edges of the dust devils are at least sufficient to lift aggregates. Their entrainment lifts dust into the atmosphere and they are at least partially responsible for maintaining the atmospheric dust loading [Ryan and Lucich, 1983, Ferri et al., 2003, Greeley et al., 2003]. High wind speeds, as

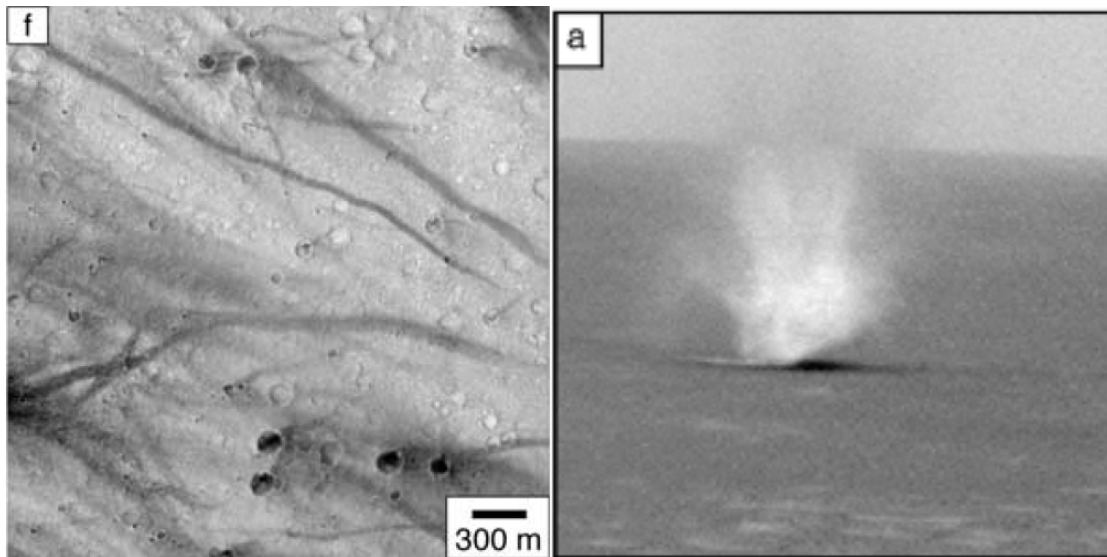


Fig. 3.2: Left: The dark streaks are inferred to be dust devil tracks as seen from orbit. Right: Active dust devil as viewed by the Mars Exploration Rover Spirit [Greeley et al., 2006].

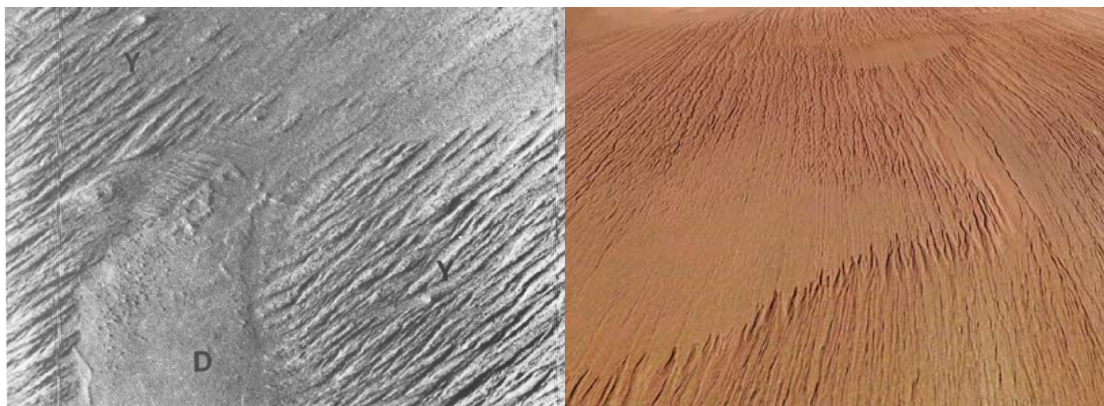


Fig. 3.3: Yardangs as imaged by the Viking lander (left) and the Mars Express High Resolution Stereo Camera (right). The left image is approximately 18 km across and the non-eroded plateaus in the right image measure 17 by 9 km [Ward, 1979, ESA yardangs]

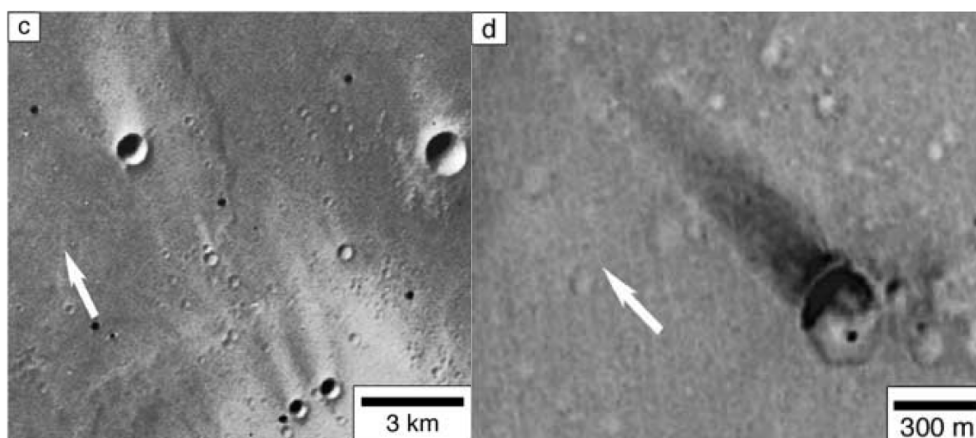


Fig. 3.4: Bright streaks (left) and dark streaks (right) as observed in Gusev crater. The formative wind direction is indicated by the arrow [Greeley et al., 2006]

3.4 Wind streaks

Mariner 9 and the two Viking missions observed variable surface albedo patterns which proved to be wind streaks associated with topological features such as craters and ridges [Sagan et al., 1973, Greeley et al., 1992, Greeley, 2006]. Observations made by later missions have found these streaks near the landing sites of both Mars Pathfinder and Spirit [Greeley et al., 1999, Greeley et al., 2004] and orbiters have imaged them over vast regions of Mars. Studies of these elongated aeolian features categorized them by their shape and color-contrast with the Martian surface.

3.4.1 Dark streaks

Dark streaks are mainly associated with topographical features such as craters, ridges and scarps¹. When the association is well-defined they are named splotch-associated streaks due to the dark irregular appearance of the topographical features. Deposition of material from the topographical features or erosion of surface dust leaving behind dark sand is believed to be the source of these streaks. Dark streaks are the most variable type, appearing and disappearing over a matter of weeks [Thomas and Veverka, 1979, Greeley and Iversen, 1985].

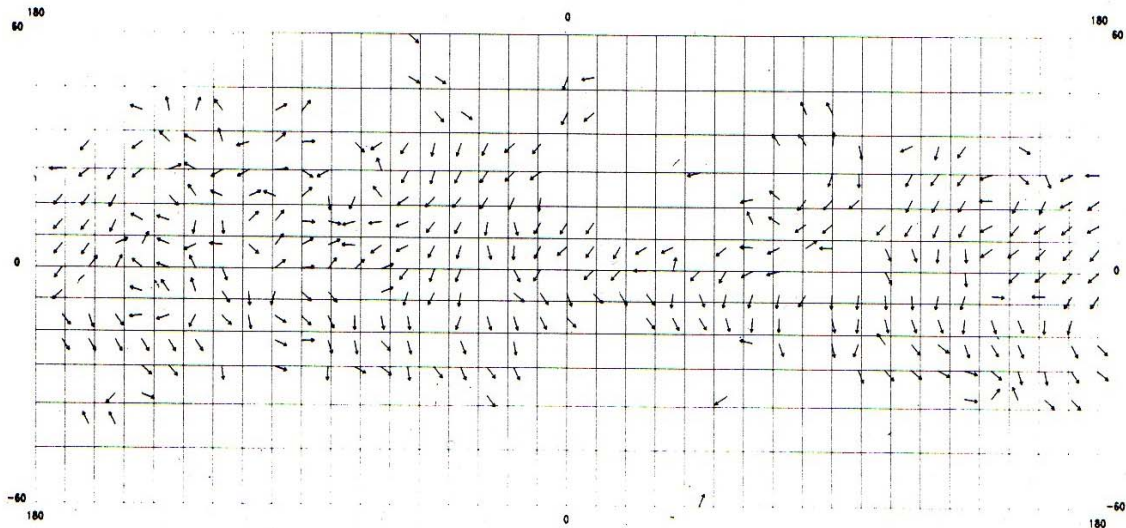


Fig. 3.5: Wind directions inferred by crater-related bright streaks. The Tharsis region is to the left where the circulation pattern is disturbed [Greeley et al., 1992].

3.4.2 Bright streaks

Bright streaks account for about three quarters of all streaks and are the most stable type. They are found in all terrains and at many craters they appear together with the dark streaks [Greeley and Iversen, 1985]. Their method of formation is not well understood but is believed to be deposition of suspended dust under conditions of high atmospheric dust content [Greeley et al., 1992]. Due to their stable nature, bright wind streaks can disclose information on the wind regime in recent times when mapping the formative wind directions as deferred from the direction of the streak. This produced the global wind map

¹ Scarp: a line of cliffs formed by the faulting or fracturing of the crust

seen in Fig. 3.5 which shows predominant wind directions from west in high northern latitudes, from northeast just north of the equator rotating to come from northwest when south of the equator. The pattern was reproduced by Lewis et al. [1999] using Global Climate Models indicating that the streaks can be formed during the dust storm season.

3.4.3 Other streaks

The three remaining categories are mixed streaks, dune streaks and frost streaks. Mixed streaks are a combination of both dark and bright streaks originating from the same topographical feature. Dune streaks are mainly found in the northern polar dune field and seem to be associated with craters in that area. Frost streaks are seen in both polar regions and follow the seasonal CO₂ frost cap [Greeley and Iversen, 1985].

Recent observations of south polar region by the High Resolution Imaging Science Instrument (HiRISE) onboard the Mars Reconnaissance Orbiter (MRO) have followed the creation and evolution of dark frost streaks appearing with the sublimation of the seasonal CO₂ ice cap. It is suggested that the Sun heats the surface beneath the translucent CO₂ slab ice creating pockets of gas. As pressure builds to a maximum the gas escapes by cracking the ice slab

entraining dust particles carried from the surface beneath the ice [Portyankina et al., 2010]. The dark streaks are created as the dust settles on the surface. Images as the one in Fig. 3.6 show the dark streaks surrounded by light blue areas of refrozen and condensed CO₂ which was also carried out by the jets [Thomas et al, 2010].

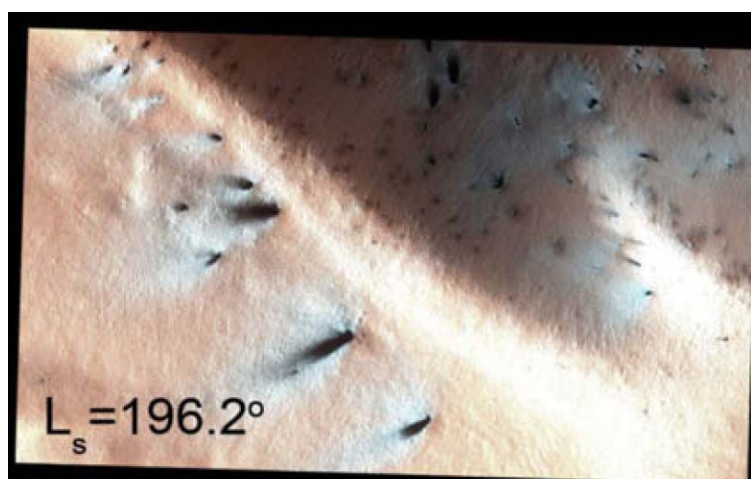


Fig. 3.6: Contrast enhanced image from HiRISE of an area in the south polar region showing dark fan-like dark streaks surrounded by light-blue areas [Thomas et al., 2010]

3.5 Dunes

Martian dune fields are mainly found in two locations: surrounding the north polar ice cap between [77:85]°N and [100:220]°W and in the southern high latitudes, predominantly in craters. Further dune formation is found in topographically controlled areas such as Valles Marineris, Argyre Planitia and Hellas Planitia [Tsoar et al., 1979, Greeley and Iversen, 1985, Hayward et al., 2007]. The globally distributed dunes are dominated by the same type of dune, namely the transverse dune (cf. Fig. 3.7), which are formed by unidirectional winds operating for extended periods of time [Greeley and Iversen, 1985].

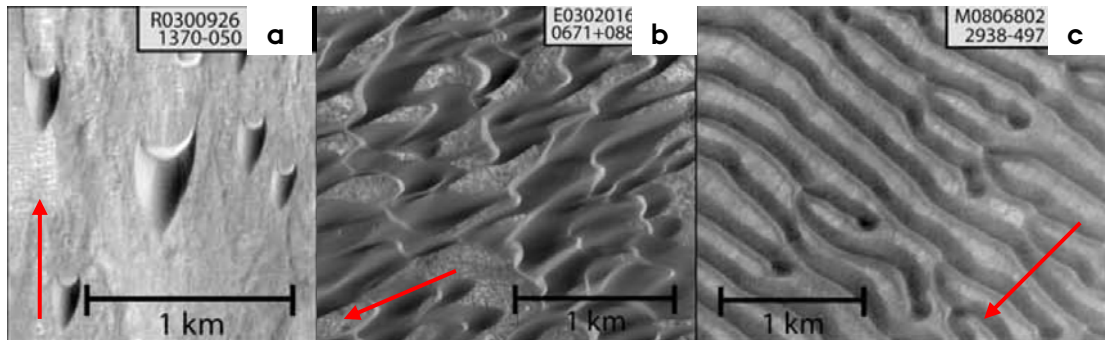


Fig. 3.7: Examples of the three dune types, which dominate the Martian dune fields: barchan (a), barchanoid (b) and transverse ridges (c). Arrows indicate the wind direction needed for formation [Greeley and Iversen, 1985, Hayward et al., 2007]

Analysis of the northern polar dune fields display winds from east north of 80°N and winds from west south of 80°N [Ward and Doyle, 1983]. The symmetric nature of the dunes indicates seasonally reversing wind directions but the details of the directional seasonal change are not agreed upon [Tsoar et al., 1979, Ward and Doyle, 1983, Lancaster and Greeley, 1990].

Singular wind direction analysis of every dune field found in the southern hemisphere has not been performed. Hayward et al. [2007] determined that they are mainly influenced by crater morphology and do not always reflect regional or local wind regimes. This observation is supported by in situ measurements from the Mars Exploration Rover Spirit in Gusev crater ($14^{\circ}30'\text{S}$, $175^{\circ}24'\text{E}$) indicating forming winds from the N-NW corresponding with afternoon up slope winds in the local area. Symmetrical dunes and ridges indicate reverse wind directions at night when wind flows are down slope from crater rim to crater floor [Greeley et al., 2006].

3.5.1 Dune movement

The analysis of dune forms indicates that winds have been very active at some point in Martian history. This does however not seem to be present times as very few reports exist regarding dune movement on Mars and none at all before 2008. Sullivan et al. [2008] performed a very thorough analysis of Spirit's observations of dunes in Gusev crater and Bourke et al. [2008] observed changes in north polar dunes.

The investigations of Spirit's observations in Gusev crater were focussed on understanding the creation and evolution of the various types of ripples in the landing area. Lighter toned ripples at the Spirit landing site were seen to be composed of a bimodal grain-size distribution. The surface component was sand grains of $700\text{-}1800\ \mu\text{m}$ while the interior was laced with $< 100\ \mu\text{m}$ sand particles. None of the observed ripples showed erosional features indicating that winds have not been able to move these features for extended periods of time. This is supported by the presence of the smaller sand particles imbedded in these ripples which would otherwise have been removed suggesting that the ripples move by creep. Close-up investigations of these ripples showed that induration had led to crusted surfaces which inhibits aeolian movement and hints at aeolian inactivity. Induration might even be able to trap air fall dust, which could otherwise agglomerate and be removed by wind. This same type of cloddy and crusted soils were also observed by the Viking landers [Moore and Jakosky, 1989], Mars Pathfinder [Moore et al., 1999], all along the

paths taken by the two Mars Exploration Rovers [Sullivan et al., 2008] and at the Phoenix landing site [Smith et al., 2009] implying that induration occurs globally on Mars.

Induration of soils may however not completely immobilize dune ripples as active saltation was observed at two instances at the darker-toned El Dorado dune field (cf. Fig. 3.8). One event resulted in sand grains up to 300 μm being deposited on the lander deck, 1.6 m above the surface [Greeley et al., 2006]. In the other event a dust storm passed by the area resulting in ripple displacements of up to 2 cm of the dark-toned ripples composed mainly of 200 – 300 μm sands. In both cases this strongly indicates that saltation is indeed active for some aeolian features on Mars, namely darker toned dunes.

Bourke et al. [2008] analyzed 3 Mars-years worth of orbital images of the northern polar dunes revealing the shrinkage and subsequent disappearance of a small number of dark-toned dunes. Neighbouring dunes were not necessarily affected, but the evidence supports the suggestion that threshold wind speeds for saltation are at times exceeded on Mars.

Dust aggregates were seen to cover both the light-toned ripples and the darker-toned ripples in the El Dorado dune field. Imaging with the Microscopic Imager [Herkenhoff et al., 2003] shows the aggregates covering surface features and rocks along Spirit's path. In a fortunate turn of events Spirit observed the passing of dust devils over the El Dorado dune field which left characteristic albedo-changing tracks, but did not disturb the ripples of the dune fields. This indicates that the dust devils can entrain the sand size dust aggregates but not the solid sand particles.



Fig. 3.8: Spirit's first view of the El Dorado crater emphasizing the spectral contrast of the dark dune field as compared to the brighter red terrain surrounding it [Sullivan et al., 2008].

3.6 Summary

The presence of both active and inactive aeolian features on Mars is somewhat contradictory. Observations of dust storms and dust devils along with changes in dust devil tracks and wind streaks demonstrate that dust is currently being entrained, transported and deposited on the surface of Mars. Yet to date there has only been two observations of changes in bedforms, both strongly indicating that saltation does occur on present-day Mars, although very infrequently [Cutts and Smith, 1973, McCauley, 1973, Snyder, 1979, Greeley et al., 2006, Sullivan et al., 2008]. It is possible that only the highest wind speeds at the Martian surface are occasionally close to the threshold for saltation and only for the narrow size distribution of sand grains in the rare dark dune formations. Soil investigations by the Viking landers and the

Mars Exploration Rovers have seen indurated and cloddy surface soils which can further inhibit aeolian activity.

The rarely observed saltation of sand cannot explain the extremely active transport of dust on Mars [Kieffer et al., 1973, Sullivan et al., 2008]. However the wind induced detachment and breakup of loosely bound sand-sized dust aggregates is a possible solution to that part of the puzzle. The aggregates break apart once they have been entrained and can stay lofted for extended periods of time. The observations of dust devils entraining aggregates at the El Dorado dune field combined with the vast quantity of dust devil tracks seen on the surface make dust devils the most likely candidate for lofting this fine atmospheric dust.

Understanding the many physical aspects which go into the puzzle that is aeolian activity on Mars has been a research field for well over 50 years at present time. The research performed in this Ph.D. examines new facets of this puzzle through observations and analysis of winds on Mars and experimental research into the effects of wind on dust removal as well as the combined effects of wind and electric fields on detachment of sand.

Part Two
The Phoenix mission

Chapter 4- The Phoenix mission

The interest for a landed mission close to the polar region on Mars, and hence the NASA Phoenix Mars mission, was born with the discovery of subsurface water-ice deposits poleward of $\pm 50^\circ$ latitude by Mars Odyssey Gamma-Ray Spectrometer in 2002 (cf. Fig. 4.1) [Boynton et al., 2002, Feldman et al., 2002, Mitrofanov et al., 2001]. Valuable scientific insight into the water on Mars could be gained by a lander capable of penetrating the surface and sampling the ice-table. Phoenix was specifically designed to look for and examine ice by digging a trench at the landing site and analyzing the excavated materials with mass-spectrometer and microscopes. These investigations were aimed at answering the main mission objectives: to study the history of water in all its phases, to search for evidence of a habitable zone and to assess the biological potential of the ice-soil boundary [PHX].

The Phoenix Mars lander became the first of NASA's Scout missions [Smith et al, 2009] and was launched August 4, 2007. It touched down on Mars on May 25, 2008 at 68.22° N, 234.25° E, becoming the first spacecraft to successfully land in the northern polar regions of Mars. The mission lasted 152 Martian days (called sols) from Ls $\sim 75^\circ$ to 150° , spanning from late spring to late summer in the northern polar region. The landing site was north of the Arctic Circle on Mars so the Sun didn't set until Ls $\sim 120^\circ$, however the Sun's maximum angle decreased rapidly hereafter. The Phoenix Mars lander was dependent on solar panels so the setting of the Sun meant less power for daily activities. A lack of power due to a combination of low solar altitude and decreased solar influx from a dust storm finally ended the Phoenix mission.

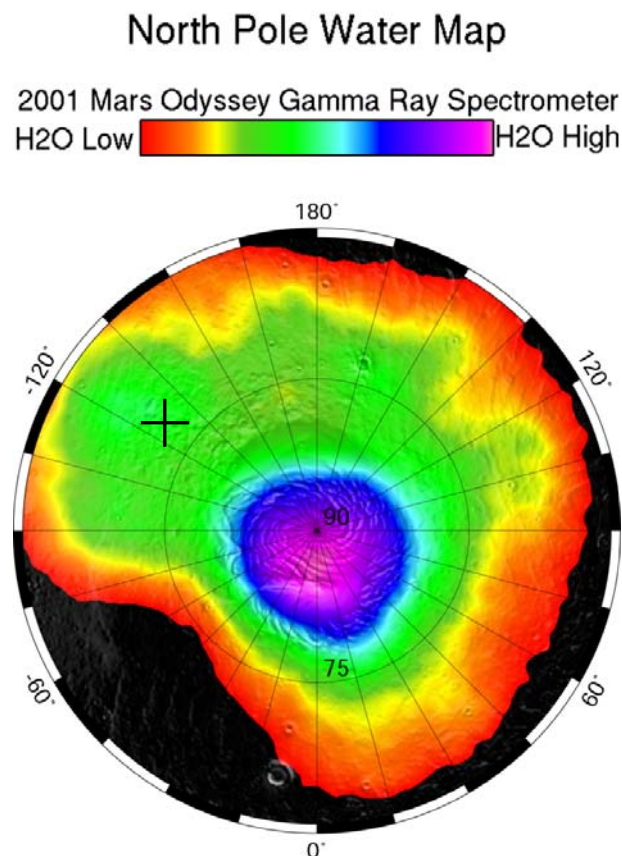


Fig. 4.1: Map of the sub-surface ice at the North Pole of Mars as measured by the Gamma Ray Spectrometer onboard the Mars Odyssey spacecraft [GRS]. The cross indicates the Phoenix landing site.

4.1 Meteorological investigations

With Phoenix being the first lander in a polar region on Mars the landing site was of high meteorological interest in order to monitor the atmospheric interaction between the polar region and lower latitudes. A suite of meteorological instruments was thus included for analysis of the weather conditions. The main meteorological goal was to determine the daily and seasonal variations in weather at the landing site, with weather being defined as temperature, dust opacity, pressure and humidity. The second meteorological goal was to determine the exchange of water vapour with the subsurface, including D/H ratios of the atmosphere and surface samples, near-surface air temperature and surface temperature, and atmospheric water vapour abundance throughout the mission. Finally the instruments should determine the bulk atmospheric composition, including isotopic ratios of three major elemental components (namely carbon, oxygen, and argon) [Smith et al., 2008].

None of the above mission goals mention wind because the initial anemometer was descopeed from the Phoenix lander. It was later deemed that wind measurements were essential for reaching the goals set forth for the meteorological instruments [Taylor et al., 2008]. Thus at a late stage in the mission preparation, a mechanical anemometer, the Telltale, was designed and calibrated at the University of Aarhus. With strong constraints on electrical power the Telltale relied on the onboard camera for images used for data analysis providing somewhat coarse, but very important, measurements of wind speeds and directions [Gunnlaugsson et al., 2008].

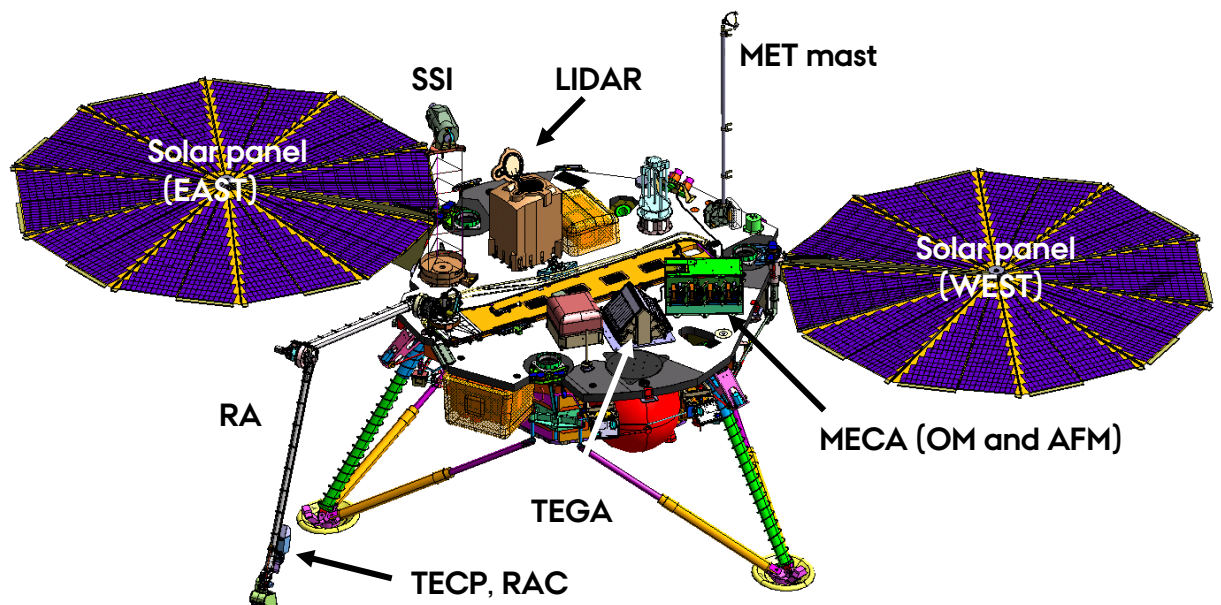


Fig. 4.2: Schematic overview of the Mars Phoenix lander with the major instruments indicated. In the landed configuration South is in the direction of the MET mast and the solar panels are approximately East and West. The landed orientation was intentional such that the workspace was on the northern side ensuring minimal sunlight exposure and thereby sublimation of newly exposed icy soil deposits [Arvidson et al., 2009]

4.2 Scientific instruments

Fig. 4.2 displays the Phoenix lander with its instruments, many of which were inherited from the cancelled 2001 Mars lander and the unsuccessful Mars Polar Lander [Smith et al., 2008]. This reduced the cost of the Phoenix mission and drastically shortened the time needed for preparation. The main bulk of the instruments onboard are naturally focussed on the main mission goals of digging and confirming the presence of ice. Many findings from these instruments link into the understanding of the meteorological mission goals and all the instruments will therefore be introduced to provide background for the meteorological results.

The first step in achieving the mission goals was to acquire soil samples for investigation. The Robotic Arm (RA) (cf. Fig. 4.3) is equipped with the Icy Soil Acquisition Device, which is a scoop with two blades for acquiring dry and icy soil samples as well as a rasp for acquisition of hard icy soils [Bonitz et al., 2008]. Material strengths of the soil and sub-surface ice layers are determined by force assessments from the RA during excavations on Mars.

Also mounted on the RA is the Robotic Arm Camera (RAC) which is one of four imaging capable instruments on the Phoenix lander. The RAC is used for close-up imagery and characterizations of soil samples in the RA and soil patches both around and under the lander. From RAC images of the work space around the Phoenix lander, digital terrain models can be fabricated, providing a coordinate system for the RA to work within [Keller et al., 2008]. This enables delicate operations such as touching the top soils and insertion of the Thermal and Electrical Conductivity Probe (TECP).

The TECP is dependent on the position of the RA for its measurements but can acquire data both in soil and while being held in mid-air. The TECP measures temperature, volumetric heat capacity as well as thermal and electrical conductivity of the material in which the needles are embedded by analyzing the heating and cooling cycles of the needles. In addition the TECP can measure the relative humidity of the atmosphere and can use

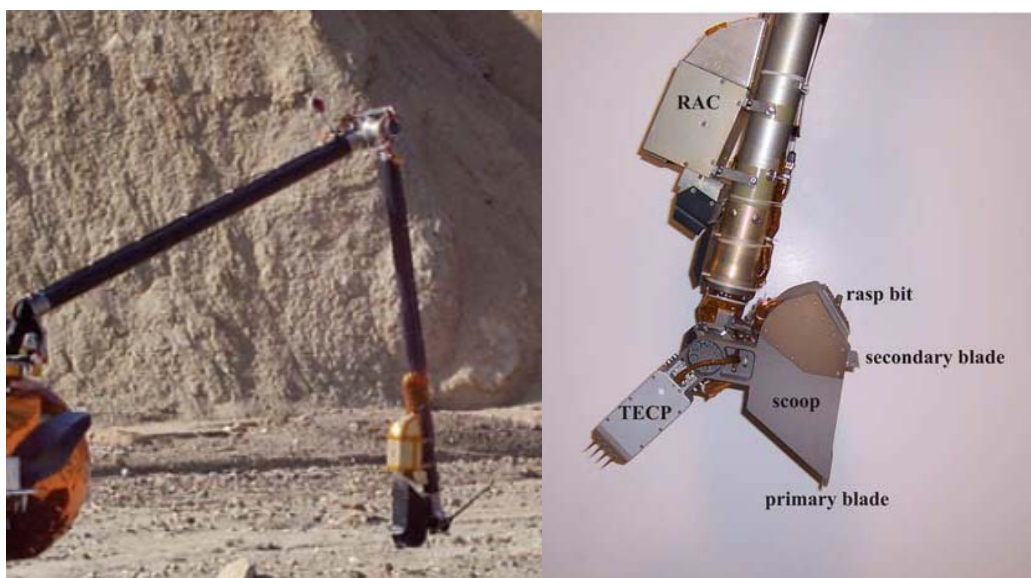


Fig. 4.3: **Left:** The Robotic Arm for the Phoenix lander during field testing on Earth [Factsheet]. **Right:** The instrument suite at the end of the RA including the rasp which was used for ice extraction [Bonitz et al., 2008]

measurements of electrical conductivity and dielectric permittivity to detect and quantify the population of mobile water molecules in the regolith [Zent et al., 2009].

4.2.1 Dedicated soil analysis

The soil samples acquired by the RA are delivered to one of two scientific instruments: the Thermal and Evolved Gas Analyzer (TEGA) or the Microscopy, Electrochemistry and Conductivity Analyzer (MECA) (cf. Fig. 4.4).

TEGA has eight small ovens, each of which can receive a small soil sample from the RA. The samples are heated to 950°C and the heat flow is compared to that of an empty oven. Differences in the heat flows will be caused by phase transitions of the minerals in the soil which can be identified by their transition temperatures. The primary interest of TEGA is to determine the abundances and isotopic ratios of water and carbon dioxide. Soil analysis by TEGA will also try to constrain the amount and nature of the soil oxidant found by Viking in the Martian soil [Boynton et al., 2001].

The MECA instrument has three parts: the TECP, the Wet Chemistry Laboratory (WCL) and two microscopes; the Optical Microscope (OM) and the Atomic Force Microscope (AFM). Where the TECP is located on the RA, an instrument box on the lander deck contains WCL and the two microscopes (cf. Fig. 4.2). RA delivers soil samples to the four crucibles that make up WCL. These soil samples are put in solution and a suite of different sensors measure the ionic concentrations of the solution, thus determining pH and examining the aqueous chemistry and reactivity of the soil sample [Kounaves et al., 2009]. Soil samples are also delivered to a sample wheel contained in the MECA instrument box. The sample wheel consists of ten sets of six substrates, each containing a strong and weak magnet, a “sticky” silicone disk, two microbuckets for bulk sampling and a textured silicon target. The sample wheel can also obtain atmospheric samples by leaving it exposed for an extended period of time allowing particles from the atmosphere to accumulate on the substrates. For every delivery a set of substrates is exposed and captures submillimeter particles by means of geometric, chemical and magnetic adhesion. The sample wheel rotates down to the OM and AFM which analyze the sample for grain shapes, surface texture, sizes and size distribution [Hecht et al., 2008].

4.2.2 Visual investigations

Every landed Mars mission has included a version of a multi-spectral camera with diverse applications and on Phoenix this is the Surface Stereo Imager (SSI) (cf. Fig. 4.5). Combining the imaging capabilities of the four imaging systems on the Phoenix lander (SSI, OM, AFM and RAC) provides the largest scale range for studying Martian particles on any Mars lander to date (cf. Fig. 4.6).

The SSI consists of two apertures (or “eyes”) each with 12 optical filters allowing the SSI to obtain stereo images and perform multispectral imaging of the workspace and landing site. These imaging qualities, along with digital elevation maps and documentation of samples delivered to the instruments

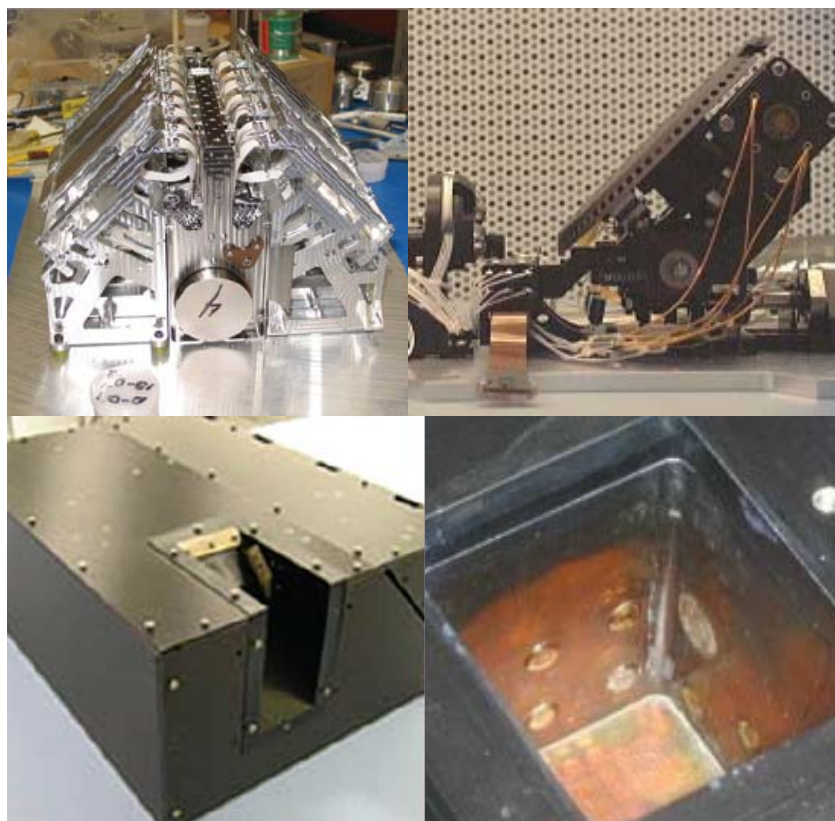


Fig. 4.4: **Top left:** Image of the Thermal and Evolved Gas Analyzer (TEGA) [Factsheet]. **Top right:** The sample wheel from the Microscopy, Electrochemistry and Conductivity Analyzer (MECA) instrument with the microscopes at the bottom of the wheel [MECA]. **Bottom left:** The opening in the MECA instrument box which is situated on the lander deck. The sample wheel is rotated to expose a sample set. The RA drops soil samples and the sample wheel can be rotated back into the box for analysis [Factsheet]. **Bottom right:** A MECA crucible used by the Wet Chemistry Laboratory (WCL). Four of these were included on the Phoenix lander, and their openings can be seen at the top right edge of the MECA instrument box [Kounaves et al., 2009].

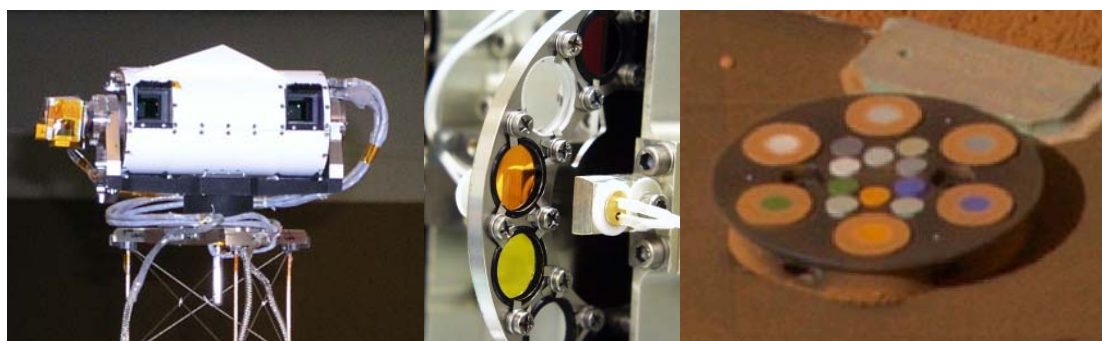


Fig. 4.5: **Left:** The Surface Stereo Imager (SSI) [PHX]. **Middle:** The filter wheel for the SSI [PHX]. **Right:** One of three iSweep magnet experiments on the Phoenix lander taken on sol 104 ($L_s \sim 124.5^\circ$) [Drube et al., 2010]

on the lander deck, support the in-depth soil analysis performed by TEGA and the MECA instrument [Lemmon et al., 2008].

Colour images taken by the SSI of the work space and landing site are calibrated using the colour references on the iSweep magnets (cf. Fig. 4.5). Similar ring magnets on previous Mars missions have shown that hardly any non-magnetic particles find their

way to the centre of the ring magnets, keeping the colours clean and suitable for calibration use [Drube et al., 2010]. The iSweep experiment also complements the findings from MECA's magnetic substrates with information on the magnetic properties of the airborne dust [Leer et al., 2008].

4.2.3 Meteorological instruments

The multiple filters and two degrees of freedom for the SSI allowed it to function as a meteorological instrument. Daily mission operations required measurements of optical depths and images of the horizon allowed for dust devil searches and cloud tracking. Series of SSI images toward zenith produced Zenith Movies in which aerosols and clouds could be tracked over the lander. Images taken with the SSI pointed towards the Sun allowed for measurements of atmospheric water vapour content and dust and ice opacity using specific narrow bandwidth optical filters [Lemmon et al., 2008, Moores et al., 2010, Tamppari et al., 2010]. The SSI observations serve as a supplement to the data recorded by the dedicated meteorological instruments on the Phoenix lander (cf. Fig. 4.7).

The LIDAR (Light Detection And Ranging) emits laser light pulses and analyzes the backscattered laser light as a function of time to measure extinction coefficients and height profiles in the atmosphere. Combining this information determines the distribution of dust and ice above the Phoenix landing site [Whiteway et al., 2008].

Pressure was measured by a pressure sensor on the lander deck. Three temperature sensors, or thermocouples, on the meteorological mast (MET mast) measure the vertical temperature profile at heights of 0.25 cm, 0.50 cm and 1.0 m above the lander deck which is ~1 m above the surface. Pressure and temperature were measured at 2 s intervals continuously throughout the mission. The only breaks stem from when the data transferral between the internal MET memory and the Phoenix lander which last ~20 min each day [Taylor et al., 2008] and when spacecraft anomalies hampered data recording.

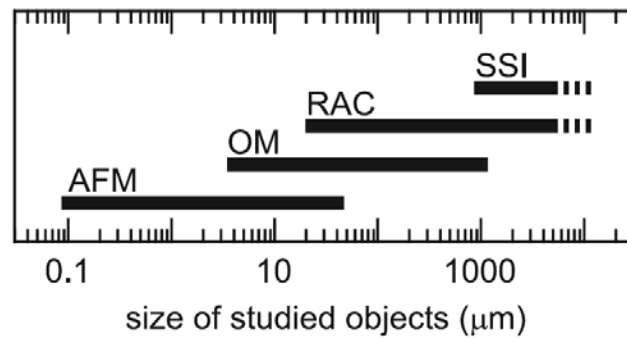


Fig. 4.6: Size range of particles which can be studied with the four imaging systems on the Phoenix lander [Keller et al., 2008]

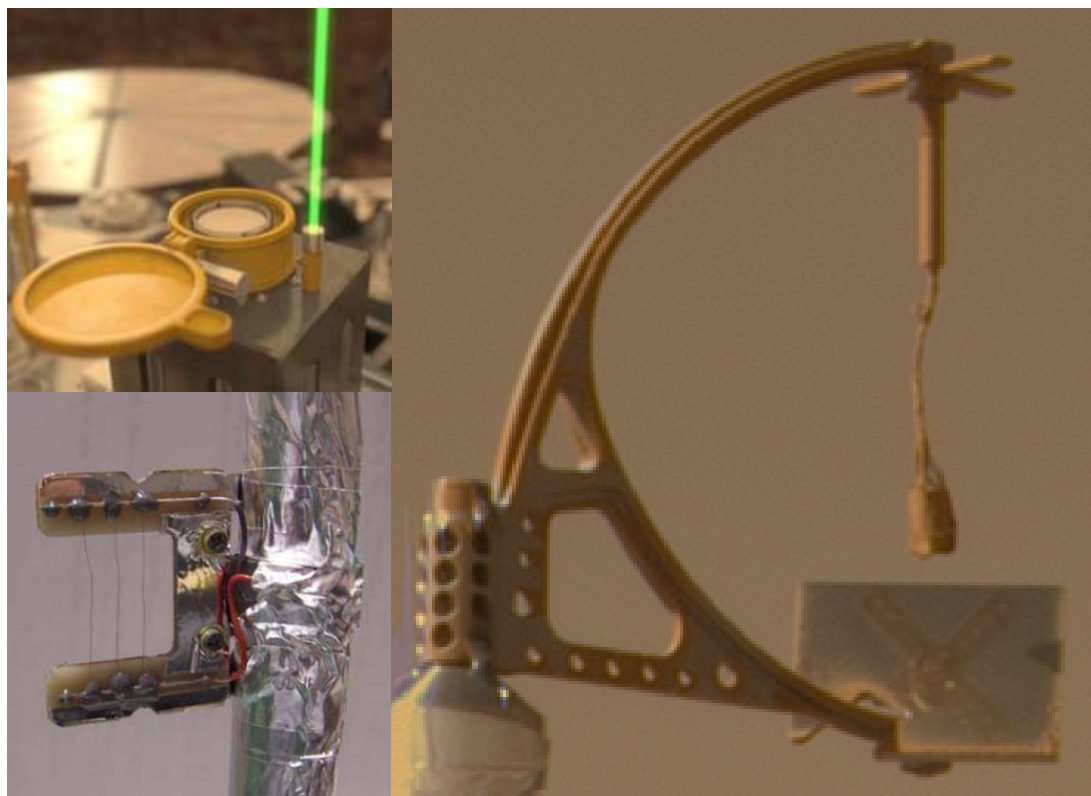


Fig. 4.7: **Top left:** an artist's impression of the LIDAR firing its laser on Mars [CSA]. **Bottom left:** one of three thermocouples attached to the MET mast [Taylor et al., 2008]. **Right:** colour image of the Telltale taken on Mars by the SSI at Ls ~ 110.5°.

An unprecedented campaign of atmospheric coordinated science was performed during the Phoenix mission, in which several instruments onboard the Mars Reconnaissance Orbiter (MRO) performed measurements at the same time, or almost the same time, as the meteorological instruments on the Phoenix lander. Five different campaigns were run to characterize the seasonal variability of dust, water ice, water vapour and examine aerosol properties. The campaigns focussed on answering outstanding questions about the climate of the northern polar region such as the relative roles of the different reservoirs of water, what is responsible for the inter-annual variability in the atmospheric components, if there is a net transport of water out of the region and what the relationship is between dust, water and CO₂ [Tamppari et al., 2010].

During the course of the Phoenix mission the Mars Color Imager (MARCI) camera onboard the Mars Reconnaissance Orbiter (MRO) imaged the north polar region on a daily basis. This allowed for tracking of clouds and storm systems providing daily weather reports to support the Phoenix mission operations [Tamppari et al., 2010]. The images have also provided a unique dataset which allow the observations from the Phoenix lander to be set in a regional context [Holstein-Rathlou et al., 2010].

The Telltale

Wind speeds and directions were measured using a mechanical anemometer, the Telltale [Gunnlaugsson et al., 2008, Lemmon et al., 2008, Taylor et al., 2008]. It consists of a lightweight Kapton cylinder suspended by

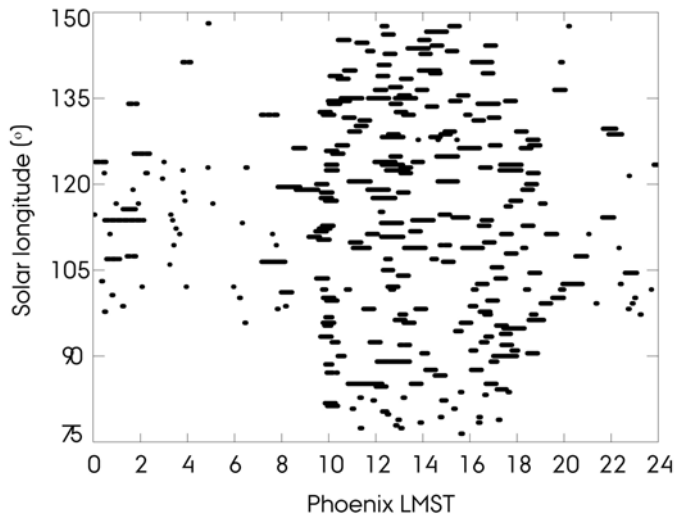


Fig. 4.8: Overview of all Telltale data acquired during the Phoenix mission with time of day plotted against solar longitude [Holstein-Rathlou et al., 2010].

Kevlar fibres designed to be deflected under the action of wind. It is situated atop the MET mast, right above the upper thermocouple.

The Telltale was imaged more than 7700 times by the SSI during the 150 sols of the Phoenix mission. Images were taken in series of, normally, 10 to 30 images with intervals of 50 seconds. A few larger image series were obtained during the mission detailing wind behaviour for nearly an hour at a time. Image analysis was performed using an IDL program

developed on the basis of the calibration data obtained in wind tunnel measurements at the University of Aarhus [Gunnlaugsson et al., 2008, Telltale Calibration Report, 2009].

As the SSI was utilized for a number of various tasks during the mission the wind data is not continuous as can be seen in Fig. 4.8. However, the sheer number of data points provides an excellent degree of seasonal and diurnal coverage. For the hours between 19 and 09 LMST (Local Mean Standard Time) the measurements are far less frequent and the data is mainly constrained to the period between $L_s \sim 95^\circ - 128^\circ$ which is due to operational constraints on the power available to the Phoenix lander. The smaller quantity of wind measurements during nightly hours proved adequate for determining the night rhythm of the diurnal cycle as this time period exhibits extremely stable weather.

4.3 Meteorological results

Phoenix spent 150 sols investigating the Martian polar surface resulting in many exciting new discoveries. Discussing all the results is outside the scope of this thesis and this chapter will focus on the meteorological findings and observations of aeolian activity giving an in-depth picture of the weather and aeolian environment as seen by the Phoenix lander.

4.3.1 Diurnal cycle

Characterizing the diurnal cycle at the landing site was one of the main meteorological mission goals and was achieved by measurements of wind, temperature and pressure.

Wind speeds and directions

Fig. 4.9 shows representative one hour data for the wind speeds, wind directions and temperatures measured from the upper thermocouple from two different sols. Wind directions according to standard meteorological convention as degrees measured clockwise from north from which the airflow is coming. Thus north is at 0° , east is at 90° , south at 180° and west at 270° .

Panes (a) to (c) display variations on the scale of minutes in all three observable due to the convective daytime turbulence (07-19 LMST) [Larsen, 2006]. Panes (d) through (f) show the stable night (19-07 LMST) wind conditions which are characterised by only slight variations in temperature, wind speeds and wind directions indicating a very stable boundary layer. This behaviour was seen to repeat throughout the mission.

The highest wind speeds are seen at midday when the Sun was highest in the sky reaching ~ 6 -8 m/s in the beginning of the mission and rising to more than 10 m/s at the end of the mission, with a maximum wind speed of 16(1) m/s measured on Ls $\sim 147^\circ$. This differs from the earlier wind speed measurements by the Viking landers which saw largest wind speeds in the morning, when the pressure gradient was largest and daily wind speeds up to 7 m/s, with a maximum of 9.5 m/s [Hess et al., 1977].

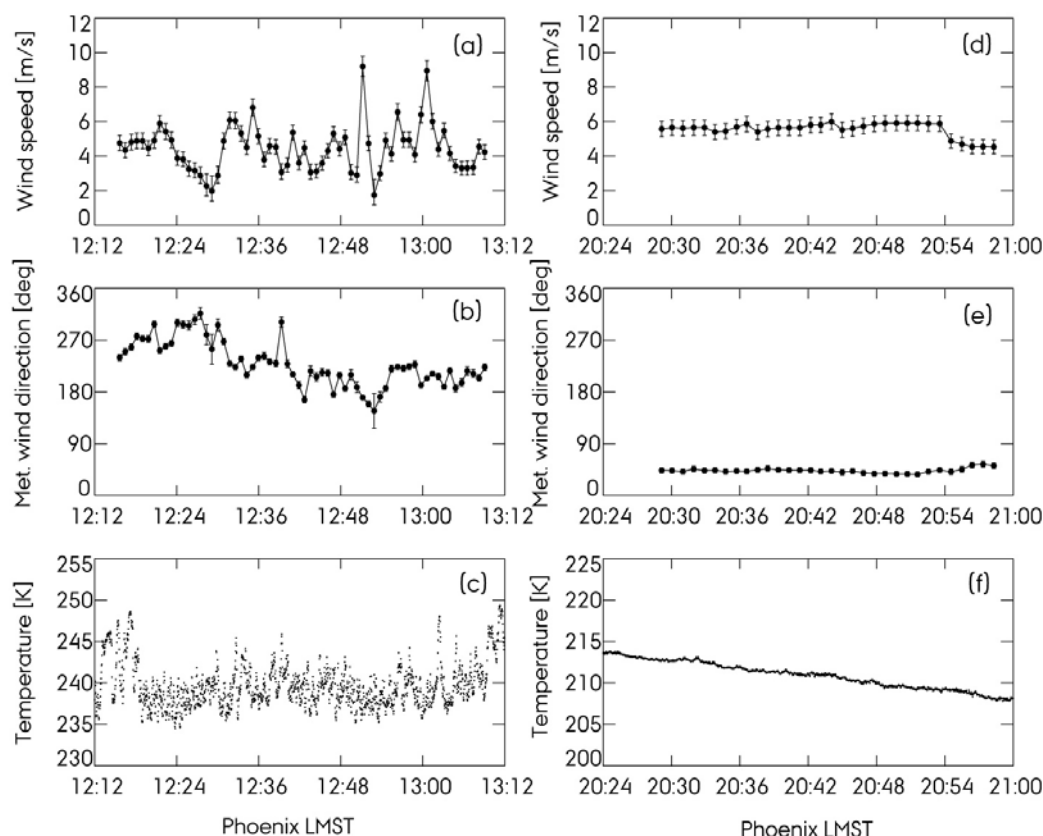


Fig. 4.9: Examples of typical wind data and their corresponding temperature data. (a-c) displays unstable midday conditions, here an example from sol 67 (Ls $\sim 107^\circ$). (d-f) shows the more stable evening and night conditions, here as an example from sol 100 (Ls $\sim 123^\circ$) [Holstein-Rathlou et al., 2010].

During daytime the wind directions at the Phoenix landing site rotate 360 degrees clockwise. This behaviour is mirrored in the Zenith Movies for cloud-moving winds at heights of 1-10 km (cf. Fig. 4.10) [Tamppari et al, 2010, Moores et al., 2009]. The Viking landers also observed a 360° daily rotation but it was respectively counter-clockwise and clockwise for the Viking Lander 1 and Viking Lander 2 sites. This was believed to be due to slope winds which cannot be the explanation for the Phoenix landing site where the slopes are small and clouds aloft mirror the rotation. This could entail a very thick boundary layer or, alternatively, atmospheric diurnal thermal tides could be evoked to explain this behaviour [Gierasch and Goody, 1968; Zurek, 1976; Leovy, 1981]. Wind directions measured by Mars Pathfinder displayed a similar pattern of daily rotation and are likely to be the result of thermal tides although the timing of the wind direction shift is slightly off, probably due to local effects [Schofield et al., 1997, Lewis et al., 1999].

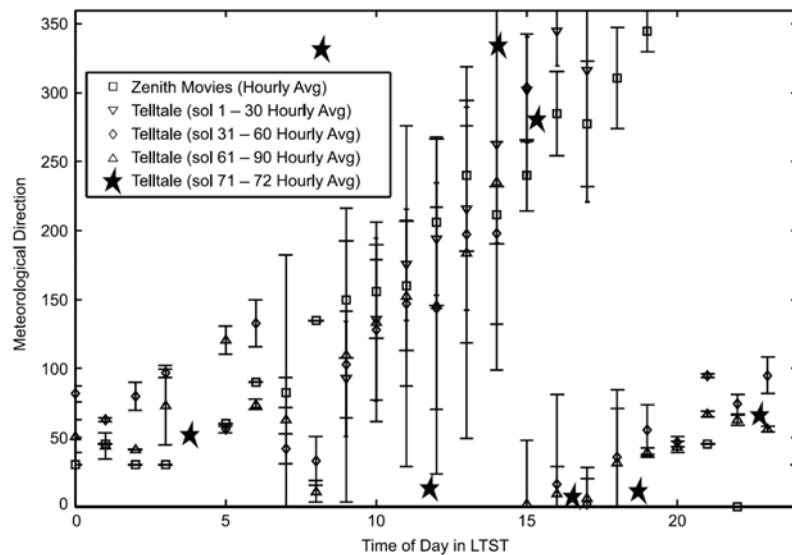


Fig. 4.10: Meteorological wind directions as measured by the Telltale compared to wind directions derived from Zenith Movies. Error bars for the Zenith Movies are 45° or 1 σ , depending on which is greater. For the Telltale the error is always 1 σ [Tamppari et al., 2010]

Temperature and pressure

Regular diurnal temperature cycles (cf. Fig. 4.11) were observed throughout the Phoenix mission in the range of -25°C to -95°C due to seasonal change (more in Sec. 4.3.2). As previously mentioned, daytime temperatures are characterized by turbulent conditions causing large temperature fluctuations. These fluctuations start at ~ 06 LMST and die out at ~ 17 LMST with night temperatures being mostly calm except around midnight. The nocturnal temperature fluctuations repeat until late in the mission and cannot be the result of turbulence. Wind directions are generally from East at the time of these fluctuations. The single largest topographical feature in the vicinity of the Phoenix lander is the Heimdall crater with a diameter of 10 km which is located 20 km east. It is possible that the fluctuations could be generated by

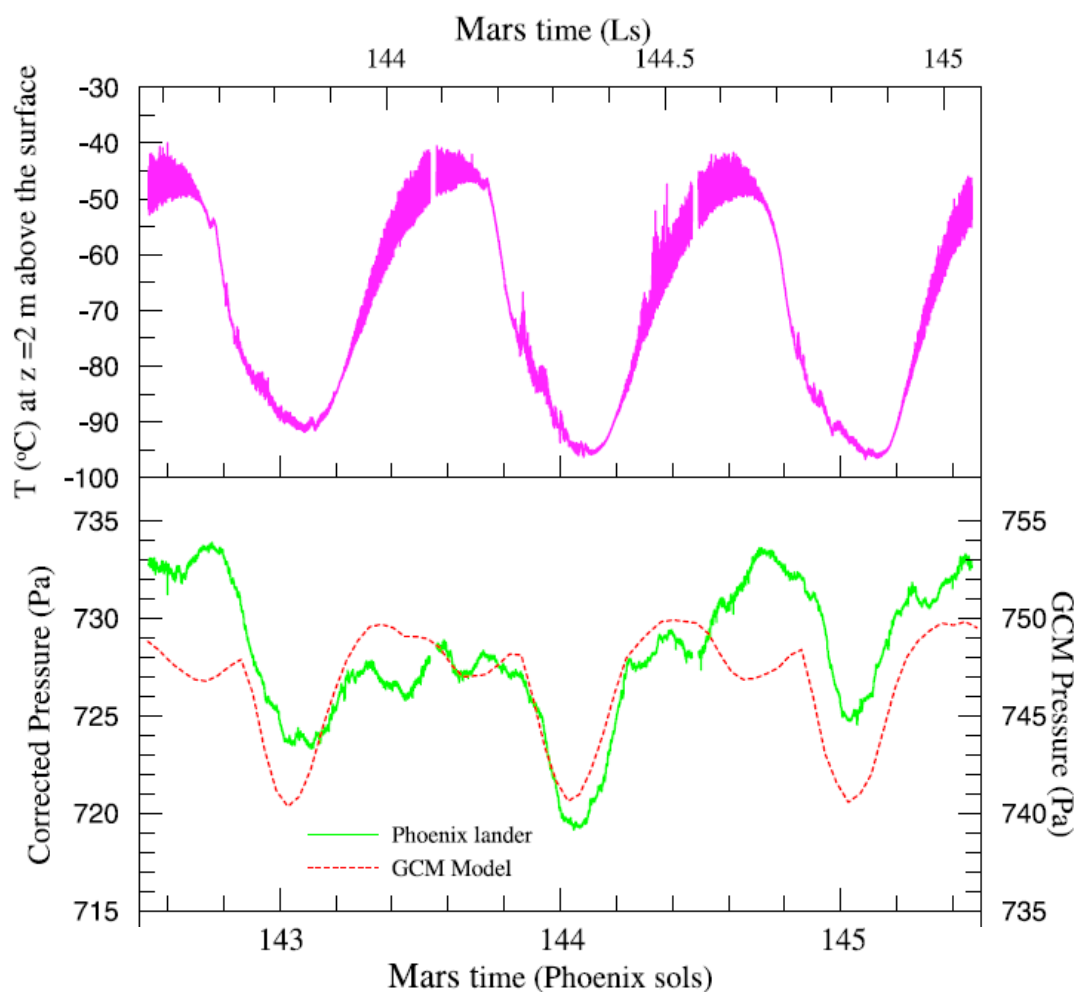


Fig. 4.11: Three sols of temperature and pressure measurements from the Phoenix lander. Results from a Global Climate Model from York University is seen to be a reasonable fit to the pressure data [Taylor et al., 2010].

atmospheric wave disturbances caused by the crater [Holstein-Rathlou et al., 2010].

The pressure displays diurnal and semidiurnal patterns (cf. Fig. 4.11) which have been attributed to a mix of atmospheric tides and waves. The assumption is supported by the fact that the behaviour is reproduced by Mars Global Climate Models albeit with differing absolute values [Taylor et al., 2010].

4.3.2 Seasonal changes

A general seasonal change is observed in measurements of wind, pressure and temperature. The beginning is marked with the first sunset of the Phoenix mission at $Ls \sim 120^\circ$ and after this date the weather changes markedly becoming more interesting from a meteorological perspective.

Wind speeds and directions

In order to view seasonal changes in wind speeds and directions average values have been calculated for each image series resulting in Fig. 4.12 for the wind speeds and Fig. 4.13 for the wind directions. Only the daytime values

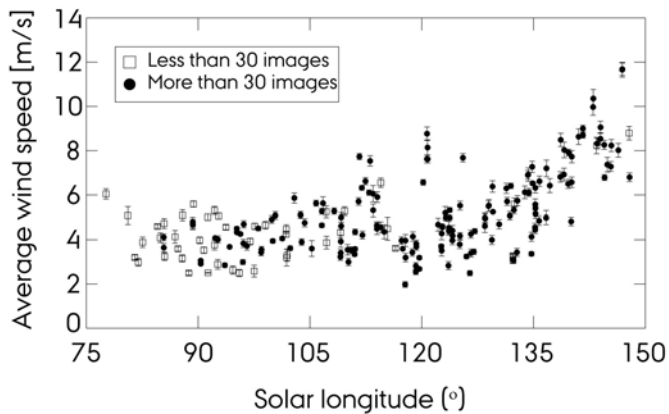


Fig. 4.12: Average wind speeds between 06 and 18 LMST as a function of mission time. Open squares mean the value was calculated from an image series with less than 30 images; closed circles indicate 30 images or more. Error bars indicate one standard deviation [Holstein-Rathlou et al., 2010].

for the average wind speeds are plotted since the nocturnal wind speeds of 4-6 m/s display no change during the mission.

For the first two months of the mission ($L_s \sim 75^\circ - 110^\circ$) the average wind speeds are 2 - 6 m/s with no wind events evident in the data. Wind speeds increase at $L_s \sim 112^\circ$ and 120° probably in relation to heightened dust devil activity and increased atmospheric activity, both of which will be

discussed later in this chapter. For the remainder of the mission the wind speeds increase steadily with the maximum wind speed of 16(1) m/s measured on $L_s \sim 147^\circ$.

Daytime average wind directions display large error bars (cf. Fig. 4.13 left) as a consequence of the daytime turbulent atmospheric behaviour. The very stable nocturnal boundary layer almost eliminates the error bars for the nocturnal wind directions (cf. Fig. 4.13 right). Both sets of wind direction data display the same seasonal behaviour. In concurrence with the change in wind speeds at $L_s \sim 100^\circ$, the wind directions shift to come from west, overriding the daytime diurnal cycle seen earlier in the Phoenix mission. Winds from west were predicted for this region based on analysis of dunes in the northern polar region (see Chp. 3) however seeming that the dunes are currently inactive the concurrence of wind directions is not necessarily associated with formative winds for dunes in the northern polar region south of 80°N .

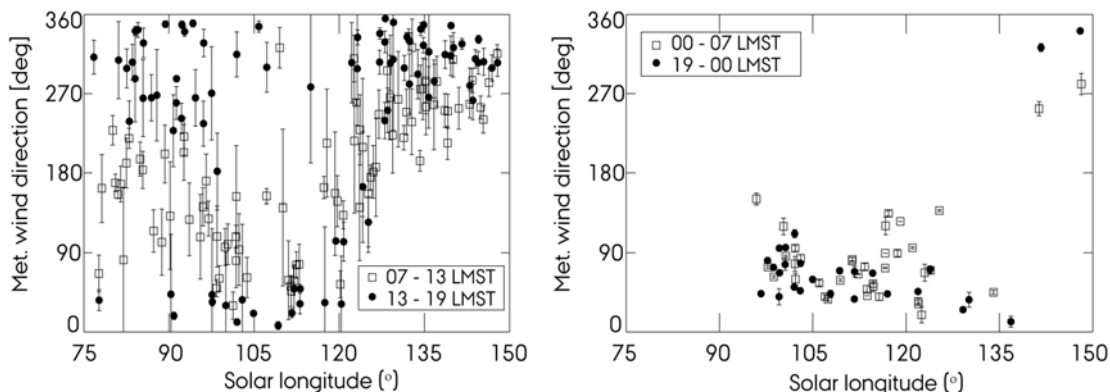


Fig. 4.13: Average wind directions during daytime (left) and night (right) as a function of mission time. In each case, the time period is split into early (open squares) and late periods (filled circles) in order to view differential behaviour. Each point represents the average wind direction of a Telltale image series with more than 10 images. Error bars represent one standard deviation [Holstein-Rathlou et al., 2010].

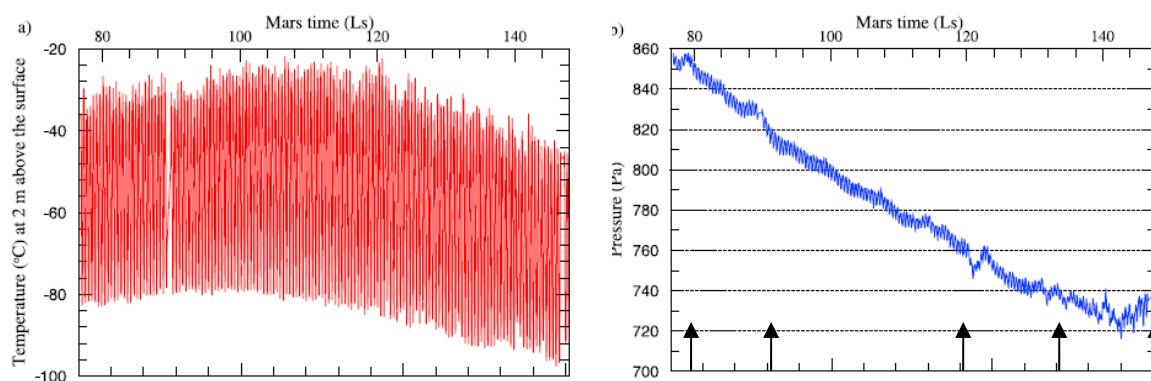


Fig. 4.14: Temperature (left) and pressure (right) as measured during the Phoenix mission as a function of mission time (Taylor et al., 2010). The arrows in the pressure graph point to the pressure peaks and dips caused by atmospheric phenomena.

Temperature and pressure

The temperature range increases slightly until Ls $\sim 100^\circ$ where after it steadily decreases for the remainder of the mission dropping an average of 15°C (cf. Fig. 4.14 left). Only the data from the upper thermocouple is plotted as correlations between wind directions and temperature difference between the lower and upper thermocouples have shown that the lower thermocouple is directly influenced by heat given off by the heating of instruments on the lander deck being blown in the direction of the MET mast [Holstein-Rathlou et al., 2010].

The pressure at the Phoenix landing site is seen to decrease during the mission (cf. Fig. 4.14 right) in accordance with the pressures observed by the Viking landers (cf. Chp. 1) due to the accumulation of CO_2 ice onto the South Pole. At two instances in the beginning of the mission (Ls $\sim 80^\circ$ and 90°) the pressure displays a small peak and at Ls $\sim 120^\circ$ a large depression is seen. These events are reactions to heightened dust devil activity and increased atmospheric activity similar to the ones observed in the average wind speeds.

4.3.3 Weather systems

During the Phoenix mission several large weather systems are seen in meteorological data. These are indicated by arrows in the pressure data (cf. Fig. 4.14) at Ls $\sim 80^\circ$, 90° , 120° , 135° and 150° . With the use of an additional three data-sets it is possible to define these different events.

The first set is the optical depth measurements from the SSI (cf. Fig. 4.15 left) in which the first two events are seen to correspond to increased optical depth. Combined with data from MRO it is indicated that dust is lofted higher into the atmosphere during these events resulting in the higher dust opacity observed [Tamppari et al., 2010].

The second dataset is the dust devils counted during the Phoenix mission (cf. Fig. 4.15 right). These were observed as short pressure drops of 15-20 s duration in the continuous stream of pressure data which entails that they have passed over or close by the lander deck [Ellehoj et al., 2010]. This dataset highlights the latter three events. Consultation with Fig. 4.12 shows that the events are correlated with increased wind speeds.

The final dataset are the images taken by MARCI which display the weather events quite clearly. When combining these images with the information from the wind speeds, pressure, optical depths and dust devils, two types of weather systems emerge.

The first type of event is observed early in the mission at $L_s \sim 80^\circ$ and $L_s \sim 90^\circ$ and is characterised by slightly elevated pressure levels and increased optical depths. No increase in wind speeds are observed in connection to these events. When these events are traced back in MARCI images (cf. Fig. 4.16) they are seen to originate when the CO_2 frost evaporates from the polar region. The increase in pressure can be interpreted as evidence for atmospheric input of gaseous CO_2 from the evaporated frost. Two possible explanations for the events are that either the dust below the CO_2 ice layer is easily put into suspension by the local winds or that the sublimation of the remaining CO_2 frost lifts dust into suspension. Observations of the south polar

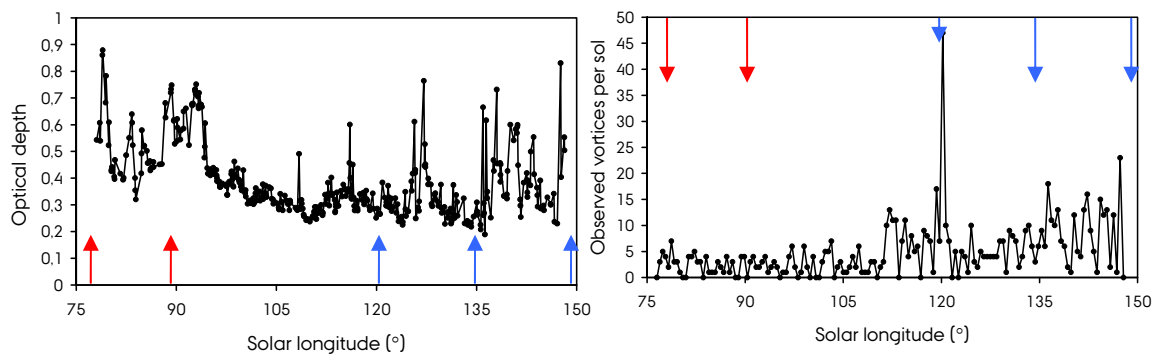


Fig. 4.15: **Left:** Optical depths as measured by the SSI during the Phoenix mission. **Right:** Number of vortices (dust devils with and without dust) as deduced from analysis of rapid pressure drops in the Phoenix pressure data [Ellehoj et al., 2010].

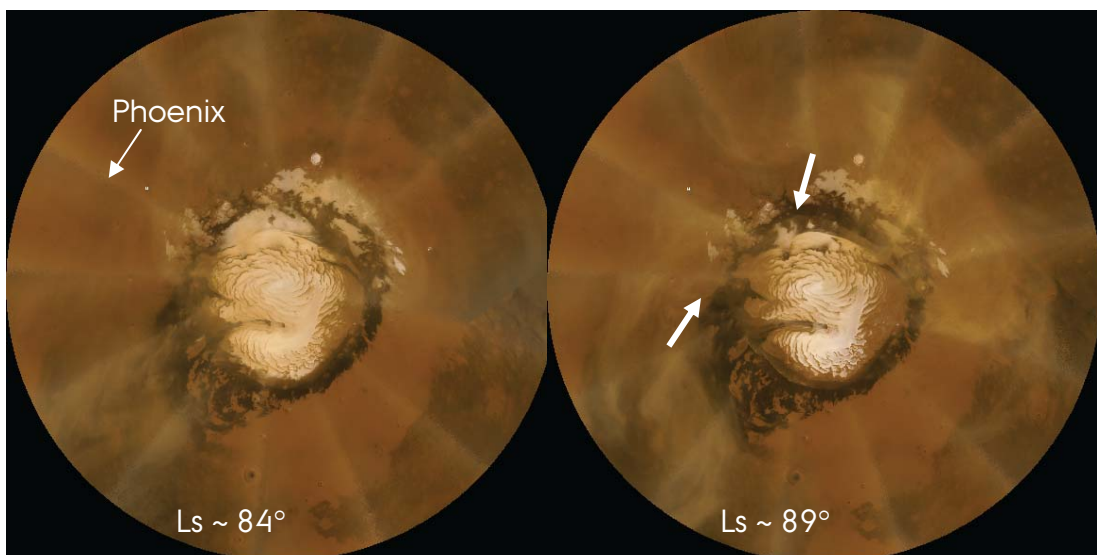


Fig. 4.16: MARCI images of the north polar region taken at the solar longitudes indicated. CO_2 frost is seen to have evaporated in the areas indicated by the arrows.

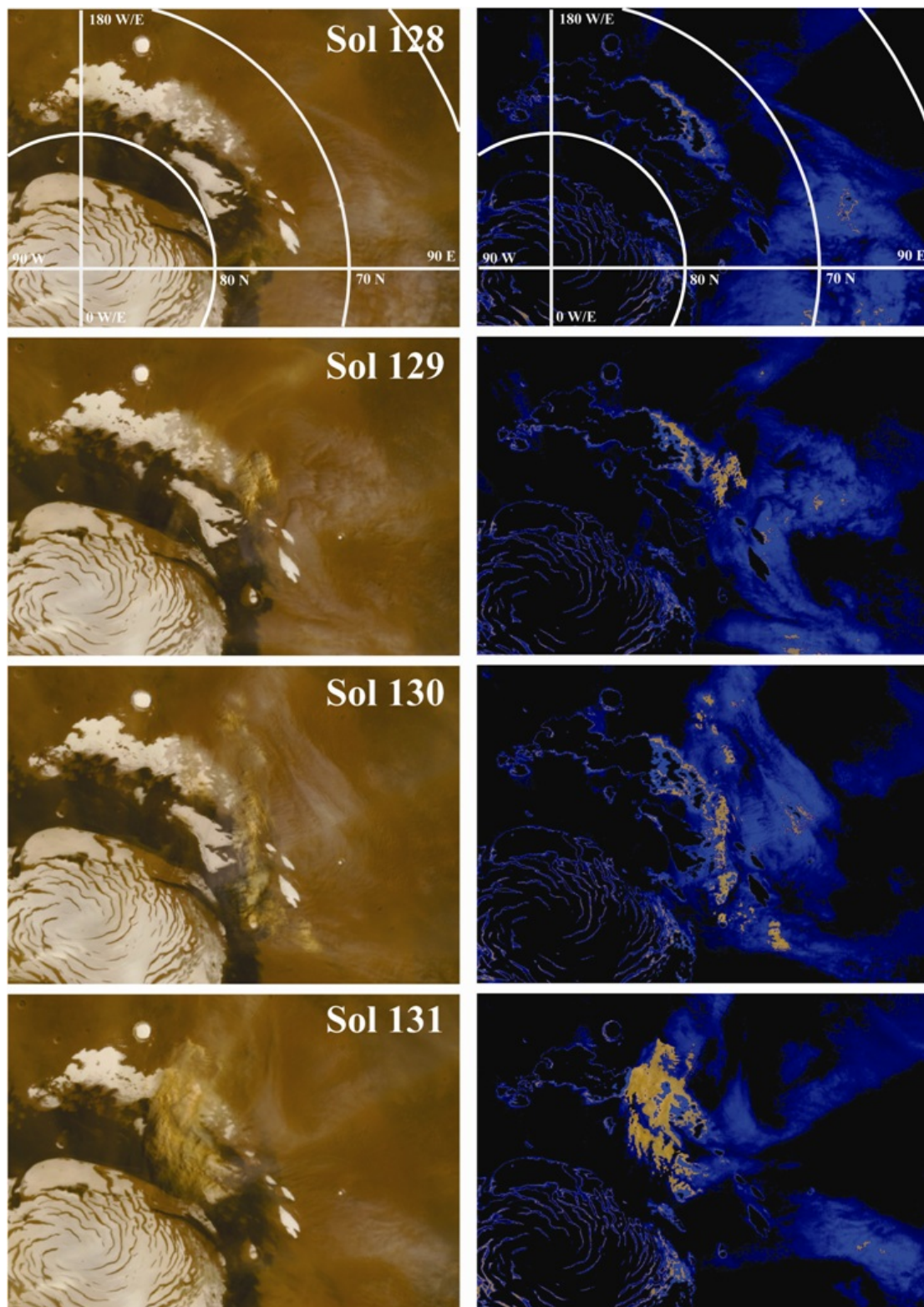


Fig. 4.17: (Left) Time series showing MARCI colour images from sols 128–131 ($L_s \sim 137^\circ$ – 138°). The color images are composites generated using 420 nm, 550 nm, and 600 nm filter band images. They have been polar stereographically projected at resolution of 2 km. The north pole is toward the bottom left in the image surrounded by the dark dune fields. **(Right)** We have picked out specific features in the original colour images. Condensate clouds are shown in blue, and bright reddish areas correspond to suspended dust. The Phoenix landing site is outside the image frame toward the left (68.22°N , 116.45°W) [Holstein-Rathlou et al., 2010].

region has seen formation of vents initiated by solar induced basal sublimation of the translucent north polar CO₂ ice (cf. Chp. 3) [Kieffer et al., 2006; Thomas et al., 2010]. However, this is likely to carry too little dust to explain the observations in the north polar region (N. Thomas, private communication, 2009).

The second type of event occurs only after Ls ~ 110° and is characterised by elevated wind speeds, elevated dust devil activity and dips in the otherwise declining pressure. The strongest pressure dip is seen at Ls ~120° concurrent with the strong peak in the average wind speeds and the maximum dust devil count on a single sol. In Marci images, these events are seen to coincide with condensate clouds passing over the landing site. Clouds travelling south of 70°N are not related to dust raising activity, but as the clouds approach the dark albedo dune fields in the north polar region dust raising events occur. An example of the latter event, occurring at Ls ~ 136.5° - 138°, is illustrated in Fig. 4.17 and a similar event at Ls ~ 148° was ultimately responsible for the loss of communications with the Phoenix lander. This latitudinal dependant behaviour of the condensate clouds has at least two possible explanations. Either there is simply more dust available for lifting in the north polar region or the frontal winds are enhanced by thermally generated winds along the boundary of the ice cover outliers and the surrounding dark frost-free terrain.

4.3.4 Atmospheric water exchange

The condensate clouds observed in connection with the second type of weather system were only regularly occurring in the final half of the Phoenix mission [Moore et al., 2009]. Prior to Ls ~ 121° LIDAR measurements showed moderate dust loading evenly distributed throughout the boundary layer. No clouds were observed by the LIDAR, but Zenith Movies and the similar horizon movies show evidence of various types of dust and ice clouds throughout the entire mission. The clouds were most prominent in morning images, consistent with observations of higher morning optical depths [Tamppari et al., 2010]. They seemed to dissipate by midday or early afternoon, an observation backed by the LIDAR measurements [Moore et al., 2009, Whiteway et al., 2009].

The presence of dust and water-ice clouds has been known since the early days of Mars exploration [Snyder, 1979] but the interaction between the atmospheric water vapour and surface was unknown until the Phoenix mission. Water vapour column abundances measured by SSI, TECP and instru-

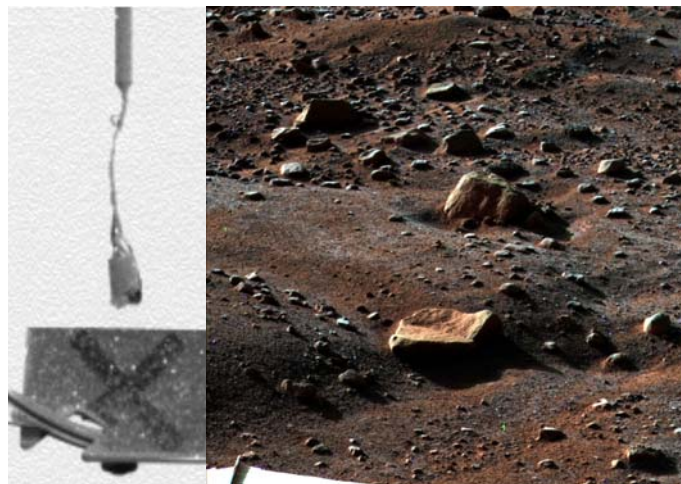


Fig. 4.18: Frost observations from the morning of sol 79/80 (Ls ~ 113°) on the Telltale mirror (left) [Holstein-Rathlou et al., 2010] and on the soil and rocks (right) [PHX].

ments onboard MRO showed a steady increase until summer solstice at $L_s \sim 120^\circ$ after which it drops off rapidly [Tamppari et al., 2010]. Just prior to this drop off ($L_s \sim 113^\circ$) a surface based cloud formation at midnight resulted in the only instance of frost formation observed during the Phoenix mission in which the atmospheric water condensates onto the Telltale and the ground (cf. Fig. 4.18) [Whiteway et al., 2009]. LIDAR and SSI horizon movies observe the first fall streaks from water ice clouds at $L_s \sim 120^\circ$ - 122° , but the precipitation evaporates before reaching the ground. Snowfall on Mars is finally observed on $L_s \sim 127^\circ$ (cf. Fig. 4.19) when the cloud layer is seen to descend in height during night, with fall streaks reaching the ground just prior to 06 LMST [Whiteway et al., 2009, Moores et al., 2009].

On a diurnal basis, the water vapour is seen to drop off around 21 LMST and increase again near 04 LMST [Tamppari et al., 2010]. This cannot be explained by frost formation as this was only seen once. Correlation of temperatures and frost points measured by the thermocouples and TECP, respectively, provides clues to where the water is going (cf. Fig. 4.20) [Zent et al., 2010]. About an hour before midnight the frost point is seen to reach a plateau indicating the condensation of atmospheric water above the surface, as witnessed by the LIDAR's surface clouds. This can however not explain the early removal of water from the atmosphere as it happens as early as 19 LMST on certain occasions [Zent et al., 2010].

Two hypotheses have been set forth dependent on the results from other Phoenix instruments. One hypothesis relates to MECA's discovery of perchlorate molecules in the soil [Hecht et al., 2009]. These molecules can adsorb six to eight water molecules each, making them a very effective sink for the water [Zent et al., 2010]. However, TEGA measured less than $\sim 1\%$ per

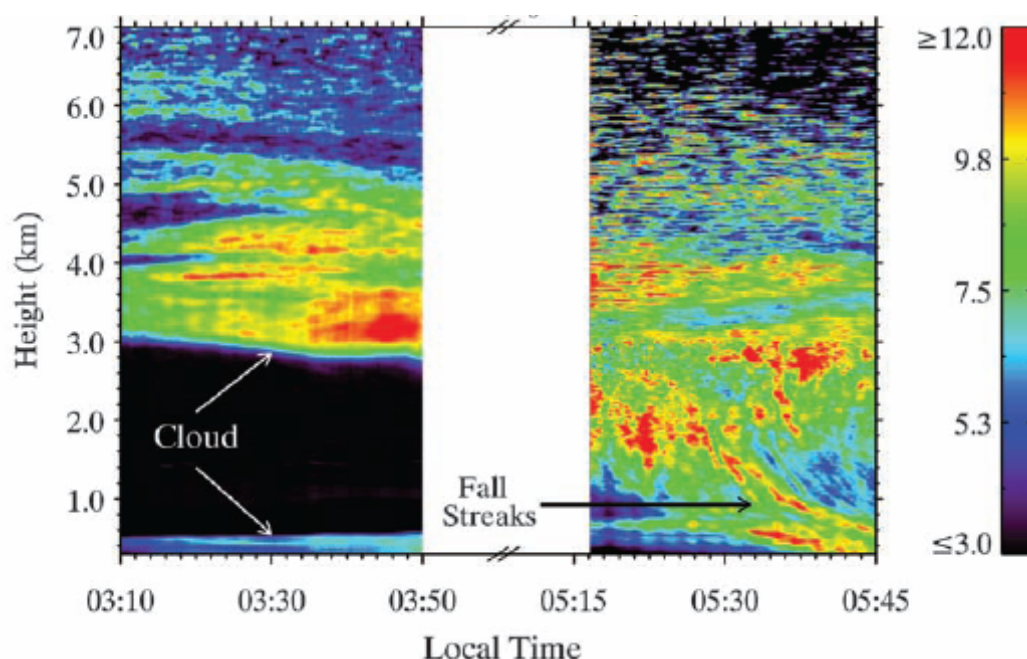


Fig. 4.19: Contour plots of backscatter coefficients derived from the LIDAR signal of sol 109 ($L_s \sim 127^\circ$) as a function of local mean standard time. They show water ice clouds and fall streaks above the landing site, features consistent with ice crystals precipitating from the clouds and eventually reaching the ground [Whiteway et al., 2009].

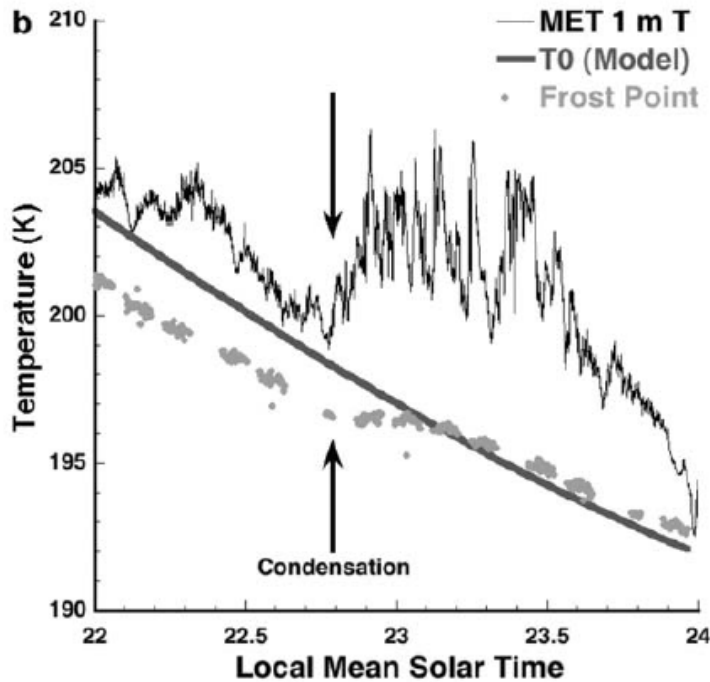


Fig. 4.20: Atmospheric frost point (grey points) and temperature from the top thermocouple (MET 1 m T) as a function of local mean solar time. T0 is a modelled surface temperature for a horizontal surface assuming the presence of ground ice at 4 cm depth [Zent et al., 2010].

weight of water in the soil indicating a very dry surface with no hydrated perchlorate molecules [Smith et al., 2009]. The other hypothesis is that the water goes into the soil, but again the dry soils measured by TEGA interfere. However if multiple layers of water molecules are adsorbed onto the surface grains it should not present as a water signal for TEGA making this more probable [Arvidson et al., 2009]. Adsorbed water is believed to be responsible for the increased cohesiveness of the soils dug up

and deposited in piles on the surface by the RA [Shaw et al., 2009] as well as being among the contenders for the aqueous process responsible for creating the calcium carbonate discovered by TEGA and confirmed by WCL [Boynton et al., 2009].

4.4 Observations regarding aeolian transport

Besides the dust devils, no signs of aeolian surface activity were seen during the Phoenix mission. Even then, it was only after $L_s \sim 125^\circ$ that the dust devils could be imaged by the SSI, as they had been dust-less devils prior to this point in time [Ellehoj et al., 2010]. Orbital observations of the landing area prior to landing revealed very few dust devils tracks and wind streaks indicating a very aeolian quiet area [Ellehoj et al., 2010]. This might be due to the cohesiveness of the soils or the presence of subsurface water-ice deposits which were confirmed by TEGA after excavation of samples with the RA [Smith et al., 2009]. Ice-cemented soils will thaw and freeze on a seasonal cycle shaping the polygonal patterned ground seen everywhere in the Phoenix landing area [Mellon et al., 2009].

The Telltale data was used to calculate surface roughness heights of 5.5(3) mm which results in a maximum friction velocity of ~ 1.1 m/s (cf. Chp. 2) [Holstein-Rathlou et al., 2010]. This gives a shear stress of 0.02 Pa which should be sufficient to move dust aggregates with diameters of around 150 μ m or above [Merrison et al., 2008]. Imaging by the Optical Microscope indicates that the building blocks for dust aggregates exist at the landing site [Smith et al., 2009]. Embedded within these building blocks are larger, slightly rounded,

sand particles (cf. Fig. 4.21) indicative of aeolian erosion over an extended period of time [Goetz et al., 2010]. The maximum shear stress of 0.02 Pa is far from the shear stress of 0.07 Pa needed to detach sand grains [Merrison et al., 2008]. Thus, the relative flatness of the landing site, resulting in the low surface roughness height, combined with the presence of active polygon formation [Mellon et al., 2010] may hamper aeolian dust and grain movement at the landing site. As a consequence no dunes are present in the area as the possible formation of dunes may take place at a rate slower than modifications of the surface due to underlying ice.

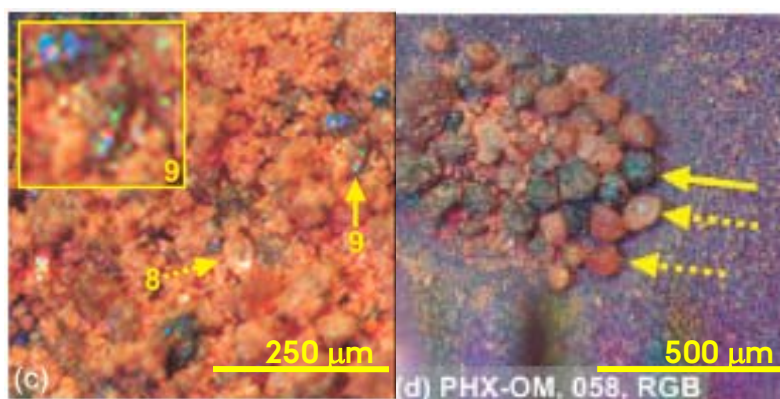


Fig. 4.21: Optical Microscope images of the soils at the Phoenix landing site showing larger particles embedded within the smaller building blocks for aggregates (left). The larger particles are seen to be slightly rounded (right) [Goetz et al., 2010].

4.5 Conclusion

The Phoenix mission was the first Mars mission to successfully land in a polar region and its 151 sols of operation provided a unique perspective on the Martian polar weather. Measurements from a suite of meteorological instruments onboard the Phoenix lander was complemented by observations from the SSI. A series of coordinated science measurements between Phoenix and MRO were run providing simultaneous orbital and surface measurements.

Diurnal and seasonal cycles were observed in the wind speeds, wind directions, temperature and pressure. The diurnal behaviour of the pressure and temperature was similar throughout the entire mission. Nocturnal temperature fluctuations are believed to be caused by the nearby Heimdall crater. Temperatures started to drop about halfway through the mission while the pressure was in constant decline due to the accumulation of CO₂ ice onto the South Pole.

The diurnal behaviour of the wind speeds was similarly unchanged throughout the mission although the average wind speeds increased during the mission. Wind directions at the start of the mission rotated 360° during the day and were steady from the east during night. Towards the end of the mission wind directions gradually changed to come from west during the entire sol.

Two types of weather systems capable of lifting dust were identified based on observations made from the Phoenix lander and MARCI on MRO. The first is related to evaporation of the seasonal CO₂ ice and is observed up to Ls ~ 95°. These events are not associated with increased wind speeds. The second

mechanism is observed after $L_s \sim 110^\circ$ and is related to the passing of weather systems characterized by condensate clouds in orbital images and higher wind speeds as measured with the Telltale.

Clouds were observed during the entire Phoenix mission with water-ice clouds being more prominent in the latter half. Snow fall was observed on Mars for the first time as fall streaks from water-ice condensate clouds. The atmospheric water content was seen to disappear much earlier in the sol than could be explained by condensation. Two possible hypotheses are the hydration of perchlorate molecules in the soil or the multi-layer adsorption of water molecules onto surface grains. The latter is most probable as it can be reconciled with measurements from TEGA of less than $\sim 1\%$ water per weight in the soil.

The only evidence of aeolian activity during the Phoenix mission was the measurements and observations of dust devils. Microscope images show slightly rounded sand particles indicative of possible earlier aeolian activity. Surface shear stresses are too low to allow sand grain detachment, but will allow aggregates to be lifted. Along with the flatness of the landing site aeolian activity probably happens at rates much slower than the surface modifications due to the seasonal freeze-thaw cycle of the ice-cemented soil.

Chapter 5 - Telltale dust accumulation

During the Phoenix mission it was observed that the contrast in images of the Telltale fibres changed with time possibly due to time dependent accumulation and removal of atmospheric dust on the fibres [Holstein-Rathlou et al., 2010]. Under Martian conditions it is difficult to remove dust from surfaces although the presence of sand-sized dust agglomerates lowers the threshold wind speed by a factor of two (see Chp. 2). Contrast changes of the Telltale fibres are however seen even when the average wind speeds at the Phoenix landing site are below the expected threshold.

Previous observations of dust removal from the magnets on the Mars Pathfinder mission concluded that wind speeds of 20-50 m/s were needed for removal [Gunnlaugsson et al., 2004] and it was suggested that this happened during the passing of a dust devil at the landing site causing wind speeds in the vicinity of ~30 m/s.

The removal of dust from the Telltale fibres could be related to high wind speed events from *e.g.* dust devils which are possibly not recorded in the intermittent data record of the Telltale. It was thus decided to study the time dependent dust accumulation in more detail and in particular evaluate the wind speeds needed under Martian conditions to remove dust from the fibres.

5.1 Analysis of Telltale fibre contrast

This analysis was performed on images closely spaced in time such that the amount of dust is roughly constant in order to see the effects of solar flux and shadowing, and to address any optical properties of the fibres and dust. Data is chosen from sols with several series of Telltale images spaced evenly throughout the sol. SSI images are assigned a pixel value, or data number (DN), from a 12 bit number read out by the CCD and the exposure duration in milliseconds can be found as the exposure duration count multiplied by a factor of 5.1. For the analysis the minimum data number of the fibres is found and the value is normalized with respect to exposure duration count and plotted with respect to the Local Mean Solar Time (LMST). The results are seen in Fig. 5.1.

The data shows two peaks, one around 03 LMST and one at 15 LMST. The first peak is when the Sun is behind the SSI, shining directly at the Telltale thus fully illuminating it creating a maximum reflection (cf. Fig. 5.2). Another peak is observed at 15 LMST when the Sun is directly behind the Telltale resulting in maximum background illumination. If the dust layer on the fibres was optically thick this should have resulted in the fibres being completely black, but the non-optically thick properties of the fibres and dust allow for a portion of the background sky-light to shine through.

Around 15 LMST the data also displays the temporal dependent accumulation of dust on the fibres. Before $L_s \sim 100^\circ$ (green marks) more light penetrates the fibres than after (red marks) since less dust on the fibres allows for more sunlight to pass through resulting in the higher values of DN/exposure duration.

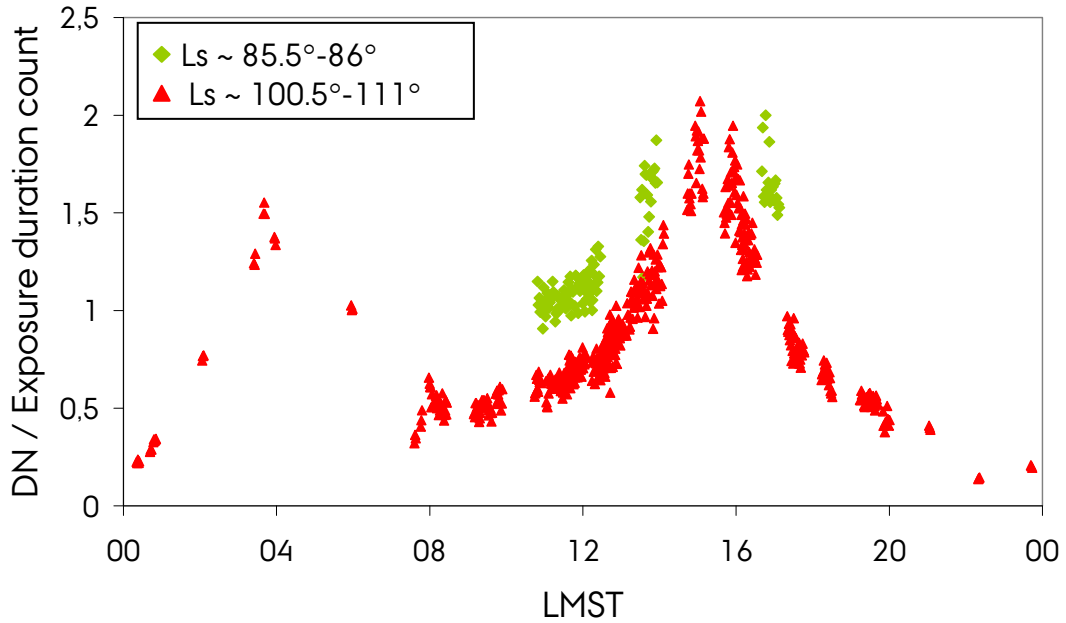


Fig. 5.1: Minimum data number of fibres over exposure time as a function of LMST (Local Mean Solar Time). The time period from Ls $\sim 100.5^\circ$ to 111° contains data from five separate sols (Ls $\sim 100.5^\circ$, 101.5° - 102° , 103° , 108.5° - 109° and 110.5° - 111°).

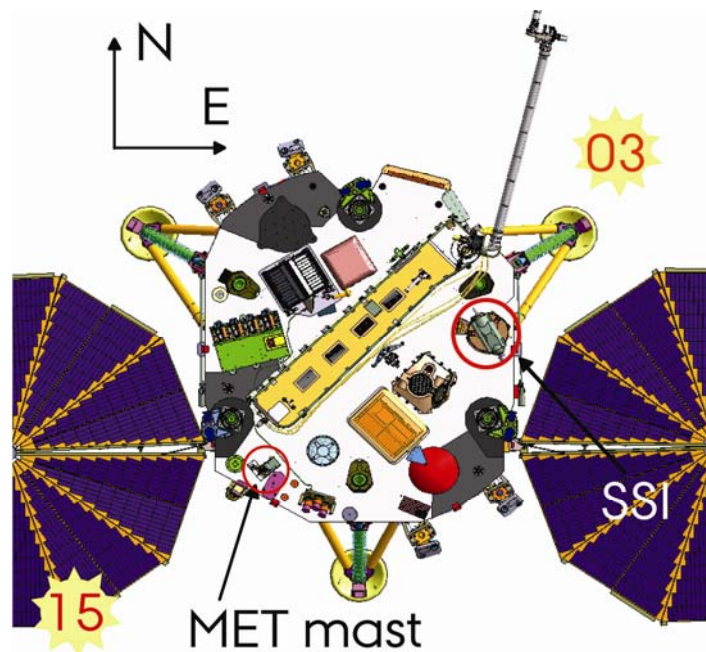


Fig. 5.2: Overview image of the Phoenix lander with the positions of the SSI and the MET mast indicated as well as the position of the Sun at about 03 and 15 LMST.

With the choice between two peaks in illumination the latter one is favoured since there are more Telltale images in the hours surrounding 15 LMST than 03 LMST (see Chp. 4). Visual inspection of the contrast change of the Telltale fibres thus used late afternoon images. In Fig. 5.3 it can be seen that the contrast increased, *i.e.* the fibres seemed darker, until Ls $\sim 100^\circ$ reaching a somewhat stable level of accumulated dust. This lasted until Ls $\sim 114^\circ$ where

after the contrast seemed to return to the level seen at and shortly after landing. The remainder of the mission showed some accumulation on the fibres, though not reaching the mid-mission level again [Holstein-Rathlou et al., 2010].

The analysis of the temporal behaviour of the dust accumulation on the fibres exploits the non-optically thick properties of the dust and fibres by examining the exponential absorption through the fibres and dust (cf. Fig. 5.4):

$$I = I_0 \exp(-d_d - d_f) \quad (5.1)$$

where I is the intensity of the fibres with dust, I_0 the intensity of the sky as recorded just behind the fibres, d_f the optical thickness due to the fibres, and d_d the optical thickness of the dust, also termed the dust factor. I_0 is calculated as an average value of the background intensity in the vicinity of the fibres in the Telltale images. The intensity of the fibres with dust was calculated both as the average data number over the fibres, as well as the minimum data number over the fibre. Both sets of data showed the same trend in dust accumulation and this study uses the average value of these numbers which was shown to have less scattering.

Upon calculating the dust factor a scaling factor, C , must be included to account for the varying intensities of the fibres in the course of one sol:

$$d_d = C \left(-d_f - \ln \left(\frac{I}{I_0} \right) \right) \quad (5.2)$$

This factor is determined from the data seen in Fig. 5.1 and varies from 1.2 to 1.05 between 12 and 18 LMST.

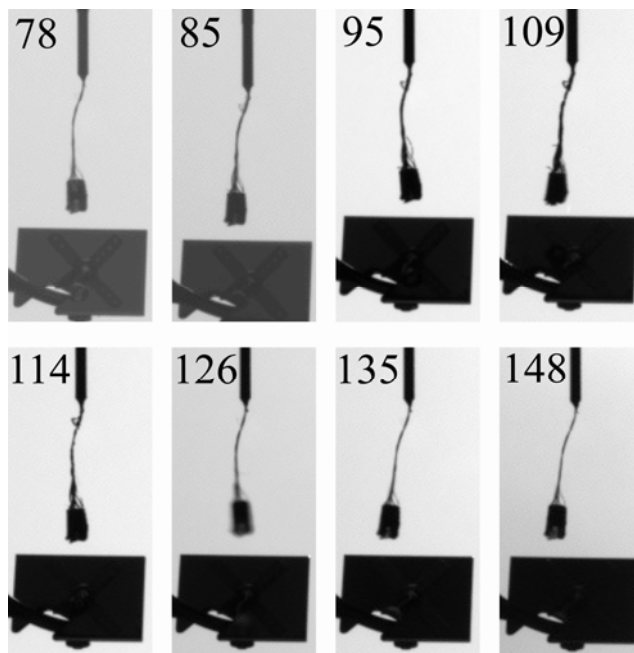


Fig. 5.3: Images of the Telltale taken at 15:35 LMST with solar longitudes indicated in the individual images [Holstein-Rathlou et al., 2010]

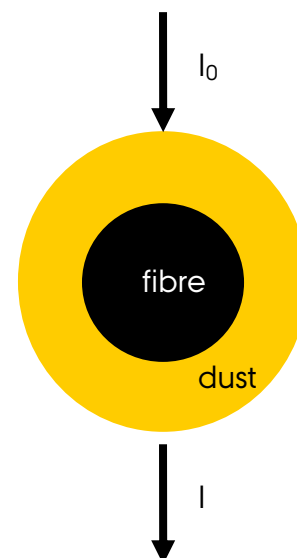


Fig. 5.4: Schematic drawing of the exponential absorption by the dust and fibres

The value of d_f was estimated to be 0.7 by assuming that d_d is zero at the time of landing, when the fibres are presumably free of dust. Some dust would have been expected to have been raised during landing but the magnets onboard Phoenix showed negligible dust accumulation at this time [Drube et al., 2010], suggesting that the assumption is sound. The result is seen in the top pane of Fig. 5.5.

A gradual accumulation of dust on the fibres from the beginning of the mission until $L_s \sim 100^\circ$ mirrors the visual inspection from the Telltale images (cf. Fig. 5.3). At this time dust accumulation slows and possibly stops all together resulting in the plateau seen. At the same time the optical depth drops (cf. Fig. 5.5, pane 2) suggesting that there is less dust in the atmosphere available for accumulation. There is also the possibility that the fibres have become saturated, but this should have led to clumps dropping from the fibres since more dust would continuously have tried to accumulate on the string overburdening the adhesive forces of the dust particles. This would have resulted in partially cleaning of the fibres, which is not seen in the data. Lastly there is the possibility that the absorption factor might simply not change with the accumulation of a sufficiently thick dust layer. A quick calculation shows that at maximum dust accumulation only about 70% of the background light is absorbed making this possibility unlikely.

From $L_s \sim 110^\circ$ to $L_s \sim 120^\circ$ the dust factor drops dramatically ending at values close to zero indicating that the fibres are more or less completely cleaned. This coincides with the beginning of the dust devil season and with the rise of the mean wind speed (cf. Fig. 5.5, pane 3 and 4). After $L_s \sim 120^\circ$ the dust accumulation onto the fibres displays an erratic behaviour with rapid accumulation and removal events probably due to the shift in weather conditions at the landing site at this time (see Chp. 4). The overall tendency is however a slow rise indicating that dust does accumulate despite the atmospheric conditions suggesting more dust in the atmosphere.

The correspondence of the mean wind speeds, dust devil counts and the rapid drop and subsequent irregular behaviour of the dust factor is the focus of this study. Is the removal of dust from the fibres dependent on very high wind speeds as can be observed in dust devils or are regular wind gusts sufficient? The highest tangential wind speed inferred from the dust devils was measured on $L_s \sim 120^\circ$ to be 14 m/s [Ellehoj et al., 2010]. The Telltale measured average wind speeds of 8-10 m/s at this time, only exceeding the maximum dust devil wind speed after $L_s \sim 120^\circ$. The cleaning of the Telltale fibres around $L_s \sim 120^\circ$ could thus be solely accounted for by dust devils if we discount the possibility of agglomerate formation on the fibres. If this occurs, wind speeds of only 10 m/s are needed (cf. Chp. 2) making winds an equally likely candidate for dust removal.

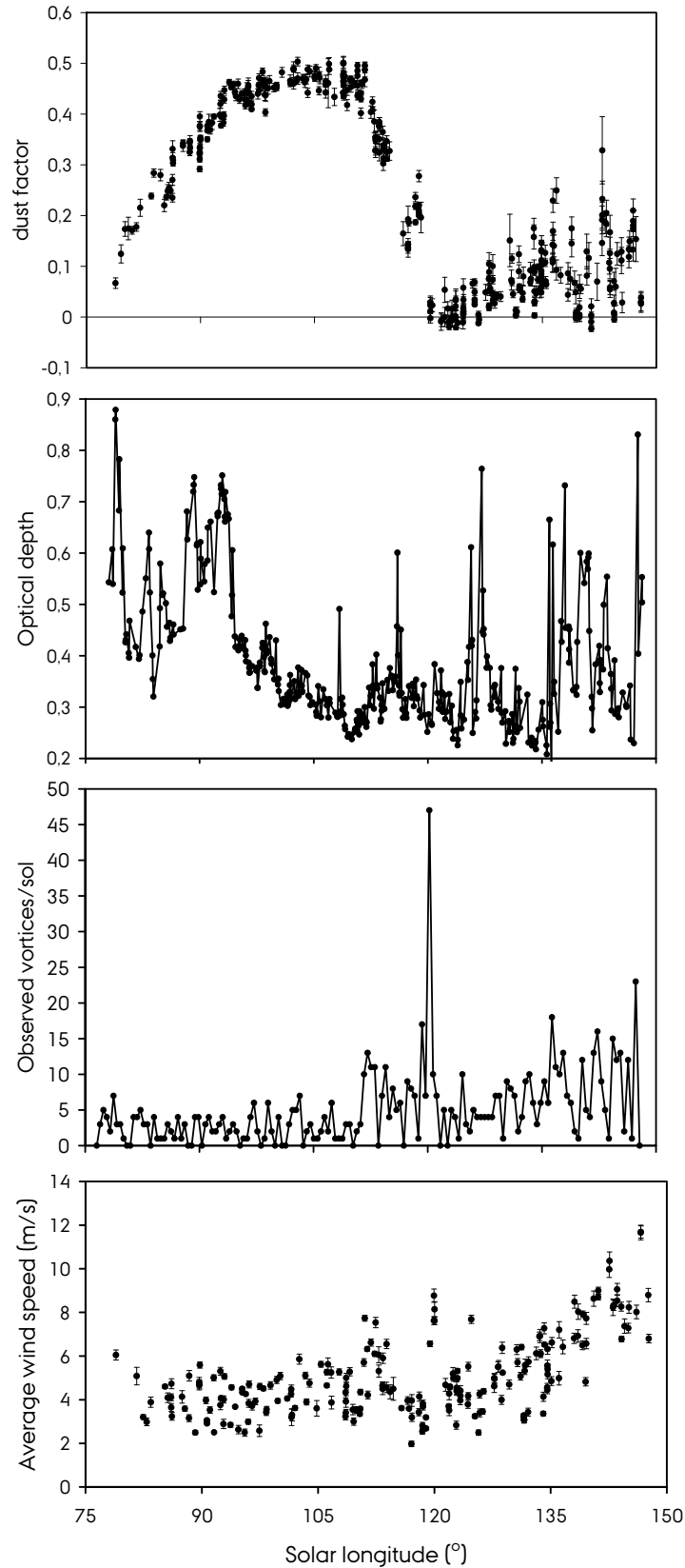


Fig. 5.5: This figure shows data and analysis results from the Phoenix Mars mission as a function of solar longitude. From top to bottom: The dust factor of the Telltale fibres as calculated from the exponential absorption. Optical depths measured from solar absorption by the SSI [Tamppari et al., 2010]. The number of vortices per sol observed at the Phoenix landing site by characteristic 5-20 sec. drop in the pressure [Ellehoj et al., 2010]. Average wind speeds from the Telltale [Holstein-Rathlou et al., 2010].

5.2 Wind tunnel facility and dust analogue

To determine the wind speeds needed for removing accumulated dust from the Telltale fibres experiments were performed in the Aarhus Mars Simulator wind tunnel (cf. Fig. 5.6). The re-circulating wind tunnel has an inner chamber diameter of 0.4 m and length of 1.5 m, encased in a vacuum chamber. The chamber can be evacuated and re-pressurized to Mars equivalent pressures. To simulate different planetary atmospheric environments the temperature can be lowered and the gas mixture exchanged. An axial mounted fan is responsible for the re-circulation from the wind tunnel to the outer chamber and can maintain wind speeds of 0-20 m/s, depending on the internal pressure. A dust injection system is located at the top of the wind tunnel allowing rapid injection of the dust along with a small volume of atmosphere [Merrison et al., 2008]. This raises the pressure slightly and in the course of experiments with many dust injections the pressure must be adjusted regularly.

Wind speed calibration was performed using a commercial Laser Doppler Anemometer (LDA) with a high spatial and temporal resolution to measure flow velocity and turbulence. The instrument makes measurements by a split frequency shifted laser beam that is subsequently focussed to produce a millimeter-sized probing volume. Within the volume the interference produce planes of high light intensity, called fringes, whose spacing provides information on the distance travelled by a particle in the volume. Particles passing through the volume will scatter the light and produce a Doppler-shifted signal detectable by a photo detector. Conversion and enhancement of the signal intensity in the detector gives the Doppler frequency, which is proportional to the travel time. With time and distance known, the velocity of the individual particles is found as an average over 16 pulses and the turbulence is the uncertainty for this average [DanTec].

For the study a Danish Mars dust analogue, Salten Skov, was used. This dust analogue has a size distribution of around 2 μm , which is in the size range reported for airborne dust on Mars [Merrison et al., 2007, Tomasko et al., 1999, Lemmon et al., 2004]. The optical properties of the Salten Skov dust are also similar to spectra made of Martian dust by Mars Pathfinder [Nørnberg et al., 2009]. This study utilizes the amount of dust accumulated due to practical reasons as detailed in Sec. 5.3.

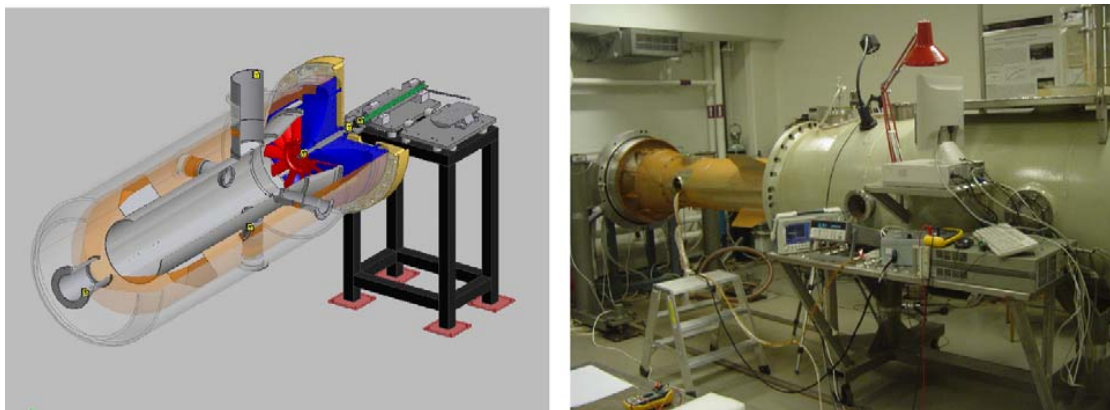


Fig. 5.6: **Left:** Schematic drawing of the Aarhus Wind Tunnel Simulator, **Right:** Picture of the partially opened wind tunnel [Merrison et al., 2008]

5.3 Laboratory experiments

A Kevlar fibre was braided to resemble the Telltale fibres [EIDP] and suspended in the wind tunnel. The string was kept taut for the sake of analysis by adding weight (cf. Fig. 5.7). An added benefit of the extra weight is a more stable string at higher wind speeds ensuring fewer blurry images of the string which would otherwise severely hamper the analysis.

An experimental challenge was presented with the lighting of the strings. The optimum situation of exponential absorption as used in the previous analysis proved to be practically unsuited for the camera equipment available. In the end reflected light was used by letting six LED lights reflect off white paper thus illuminating the strings with diffuse light. This simulates the lighting conditions at 03 LMST rather than 15 LMST which makes no difference to the experiment.

Dust accumulation was simulated by injecting ~ 600 mg portions of Salten Skov at low wind speeds to keep the dust suspended in the wind flow. At wind speeds of 1.5 m/s dust concentrations in the wind tunnel fall off exponentially with a time constant of 200 s [Merrison et al., 2008]. A new portion was injected every 120 s ensuring that there was an almost continuous amount of suspended dust available for accumulation. A total of 30 portions were injected for each experiment which was seen to be enough to produce an amply thick dust layer on the string.

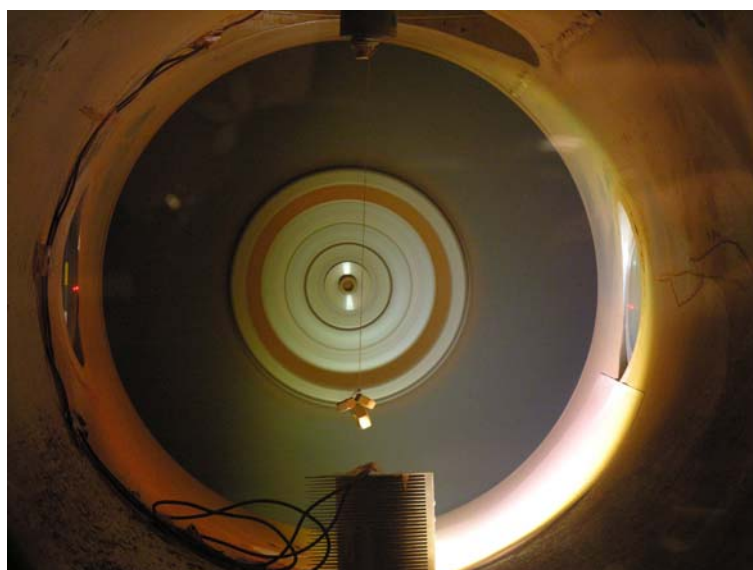


Fig. 5.7: Experimental setup of string with bolts attached for added weight in the wind tunnel. The LED lights reflect off the white paper in the right side of the wind tunnel.

Comparing the injected dust amount in the wind tunnel to the accumulated dust on the fibres is not a straightforward matter. The only known quote for the atmospheric particle density on Mars is 1-10 particles/cm³ [Hargraves et al., 1977] which is far too uncertain to use for comparison. Another way of roughly estimating this number is by dividing the column number density by the gas scale height. The first number has only been estimated for data from the Mars Pathfinder mission [Tomasko et al., 1999] and the latter is assumed to be about 11 km (M.T. Lemmon, personal communication). Scaling this to the

optical depths measured during the Phoenix mission results in an average atmospheric particle density of ~ 5 particles/cm³, which is in agreement with the quoted numbers from Viking. This number can be converted into an hourly dust rate of $\sim 7.3 \cdot 10^6$ grains cm⁻² hr⁻¹ by use of the average wind speed of ~ 4 m/s (see Fig. 5.5) as measured by the Telltale during the first 90 sols of the Phoenix mission. From measurements with the LDA the particle density per injected mg of Salten Skov dust is known to be $\sim 4.5 \cdot 10^4$ grains cm⁻² mg⁻¹ (J.P. Merrison, private communication). By dividing the hourly rate by the particle density of the wind tunnel the quantity of dust needed to simulate one hour of atmospheric dust exposure on Mars is found to be ~ 160 mg. Thus one injected portion corresponds to almost 4 hours exposure at the Phoenix mission landing site during the first 90 sols. The total injected dust amount thus corresponds to 5 sols on Mars. This is an acceptable amount seeming that it provides a suitable layer of dust for the removal process and is not enough to saturate the strings.

With the dust deposited on the string the removal process could begin. Wind speeds in the wind tunnel were ramped up in intervals of two minutes from ~ 1.5 m/s to ~ 17 m/s in steps of ~ 0.25 m/s. This allowed each wind speed to remove as much dust as possible so that the effects of the next higher wind speed would be evident. The cycle was documented for analysis with images for every new dust portion and wind speed interval.

The experiment was repeated with atmospheric air at four pressures (9, 11, 14 and 20 mbar) which can be converted using the ideal gas equation to the corresponding Martian atmospheric pressures of 4 to 9 mbar at temperatures of -50°C . In the first 90 sols of the Phoenix mission this was the mean daytime temperature and with pressures measured to between 7.6 and 8.6 mbar [Taylor et al., 2010], the experiment covers a slightly larger range than what was experienced at the Phoenix landing site.

5.3.1 Analysis

In the laboratory we used reflected light to estimate the dust accumulation. The first conception was to measure the intensity of reflected light from the fibres and accumulated dust. This idea was discarded because during the removal phase, the increasing wind speeds suspended additional dust from the walls of the wind tunnel, making it increasingly difficult to discern the reddish string from the red airborne dust.

The analysis therefore concentrates around determining the width of the string with and without dust to determine a fractional number for the amount of dust accumulated. To acquire a reasonable number for the width of the string in an image an average over the length of the string was used due to variable accumulation and removal over the length of the string. In the analysis only the red filter was viable due to the

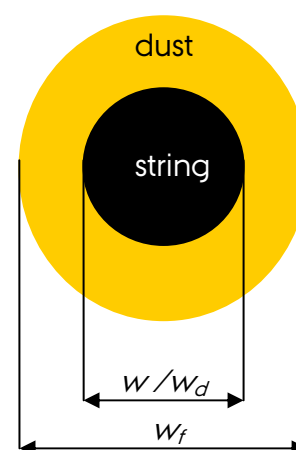


Fig. 5.8 : Schematic drawing showing the geometry used for the experimental analysis.

optical properties of the Salten Skov dust, making the string blend into the background in the green and blue filters. The final calculation used for every image was:

$$\alpha = \frac{W - W_f}{W_d - W_f} \quad (5.3)$$

where w is the width of the string with dust in the image being analyzed, w_f is the width of the string alone (cf. Fig. 5.8) which is determined from images taken before dust was accumulated on the string (cf. Fig. 5.9) and w_d is the width of the string with the maximum amount of accumulated dust, which is found from the images taken immediately after the wind speed is set to zero after the final dust portion has injected in the wind tunnel. The final number, α , is thus an indicator of the percentage of dust on the string as seen relative to maximum accumulation.

According to Eq. (5.3) α should be between 0 and 100% but loose threads such as those seen in Fig. 5.9 (middle image) can give slight differences leading to values of slightly over 100%.

The final value of α never becomes equal to the initial value due to the inability of the wind shear at the wind speeds used to remove the final layer of micron-sized dust on the string (cf. Chp. 2). The situation is illustrated in the color difference between the left and right image of Fig. 5.9 in which the string is, respectively, completely devoid of dust at the beginning of the experiment and covered by the fine layer of dust at the end of the experiment.

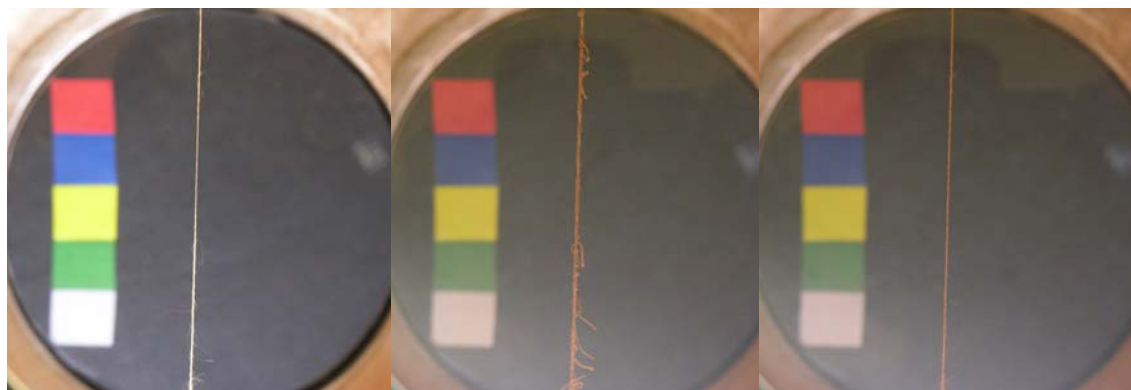


Fig. 5.9: Images of three different stages in the experiment. **Left:** first image taken (before accumulation) used to determine w_f . **Middle:** an image from after accumulation and before removal used to determine w_d . **Right:** a final image when the wind has removed as much dust as possible. In the background can be seen a color reference which was not used after all, since the final analysis concentrated on the width of the string, rather than the initial idea of examining color change.

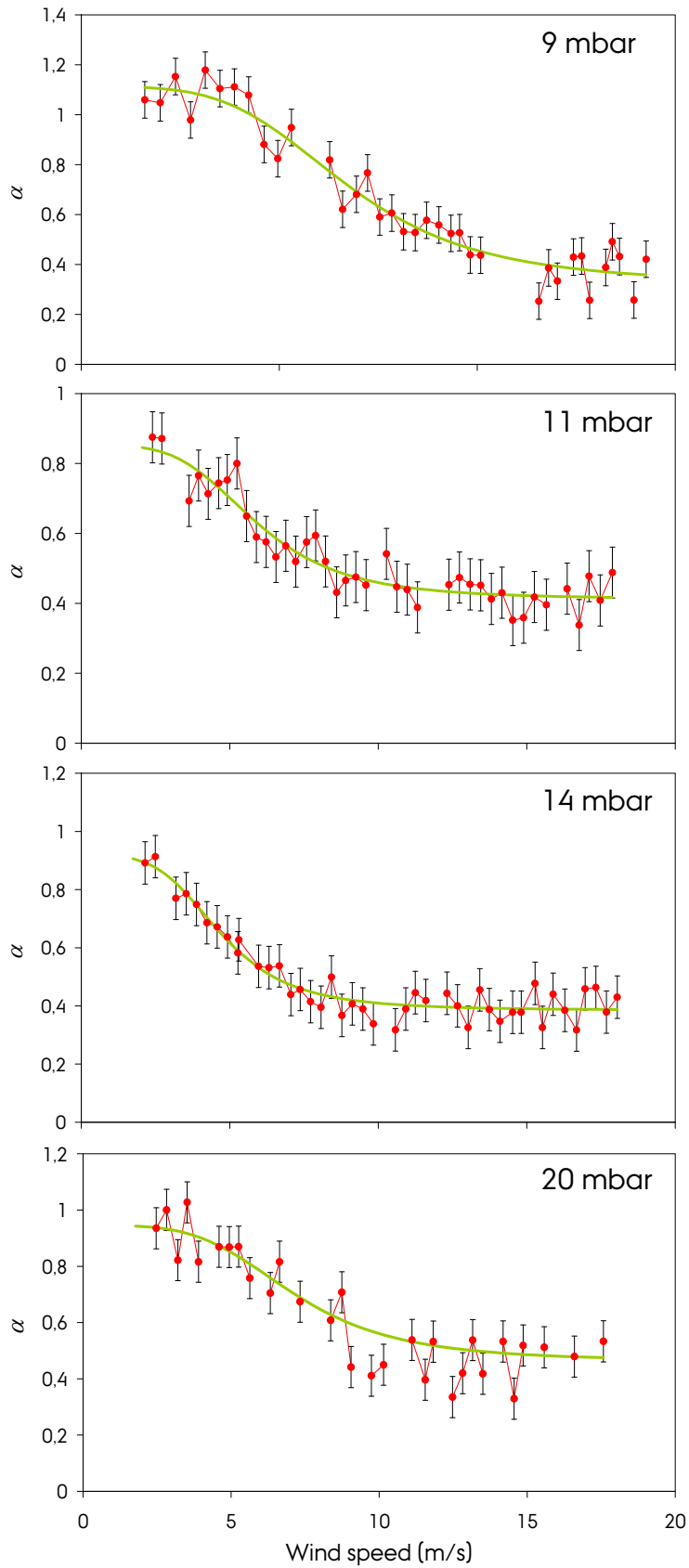


Fig. 5.10: Fitted experimental data for the dust removal phase for 9, 11, 14 and 20 mbar atmospheric pressure (4, 5, 6 and 9 mbar equivalent CO_2 pressure) (from top to bottom). The error bars are one sigma deviations.

Analysis of the dust removal phase resulted in the four graphs of Fig. 5.10. At high wind speeds the added weight was not always enough to keep the string steady and without a high speed camera, sharp images were not possible. Analyses of a blurred string led to unnaturally large values of the string width and the data from these images were therefore deleted by hand. The data was fitted to:

$$\alpha = \frac{A}{1 + \left(\frac{v}{v_{1/2}}\right)^B} \quad (5.4)$$

where A and B are fitting constants which influence the shape of the curve, v is the wind speed where the curve flattens at the end of the run indicating that dust is no longer being removed and $v_{1/2}$ is the removal wind speed, corresponding to where half of the dust has been removed from the string. The results are summarized in Table 5.1.

An additional two experiments were run at room temperature with 100 mbar atmospheric air and 9 mbar CO₂ (corresponding to, respectively, 49 and 6.7 mbar CO₂ at -50°C). The experiment run at 9 mbar CO₂ closely resembled the similar experiment run in air, proving the validity of the experiment in another atmosphere. At high pressure the analysis was difficult due to the large oscillations of the string, but analysis found a removal wind speed of about 4 m/s. This is consistent with a denser atmosphere providing a larger wind shear stress making it easier to remove dust from the string.

Table 5.1: The removal wind speeds as calculated from the removal phase of the experiment.

P [mbar]	$v_{1/2}$ [m/s]	$\Delta v_{1/2}$ [m/s]
9	6.74	0.32
11	5.90	0.45
14	4.69	0.28
20	6.86	0.35

5.4 Discussion and conclusion

The initial belief that very high wind speeds were needed to remove the accumulated dust from the Telltale fibres has been effectively laid to rest. This study has showed that wind speeds less than 10 m/s are sufficient. Wind speeds of this magnitude are measured by the Telltale on a regular basis in the latter half of the Phoenix mission [Holstein-Rathlou et al., 2010] where the removal of dust is seen to happen frequently. Thus winds alone would be sufficient for removing dust from the fibres.

The role of dust devils in the removal of dust from the fibres hinges on them actually passing the Telltale in order to affect any changes. During the Phoenix mission many dust devils were measured to pass over the lander and a few passed the Telltale [Ellehoj et al., 2010]. As their number increases at the same time as the wind speeds increase, it is most likely that they have assisted in the dust removal from the Telltale fibres, but they are not necessary for dust

removal. The large dust removal event at $L_s \sim 120^\circ$ is most likely the result of the passage of a few dust devils with very high tangential wind speeds. The maximum for dust devil wind speeds was measured on $L_s \sim 120^\circ$ and this one event could have been responsible for the final clearing of dust at this time.

During the removal phase of the experiments, the dust was seen to come off in chunks rather than single particles, which is interpreted as agglomerates breaking off. The low wind speeds needed for removal are below the threshold for detachment of agglomerates (cf. Chp. 2) which could indicate that dust agglomerates forming on the surface of the string are very loosely bound to the string by adhesive forces. The physics governing wind flow around a cylinder, such as the string, are not fully understood [Alves et al, 2001, Rajani et al, 2009] but the process of agglomeration would effectively lower the shear stress necessary for removal of the accumulated dust. At the end of the experiment the string is still covered by a thin layer of dust indicating that all the agglomerates have been removed. The final layer of dust particles would require extreme high wind speeds to remove due to the adhesive forces between the dust particles and the string.

The fact that the dust removal only starts past $L_s \sim 110^\circ$ shows that no major wind events have been missed by the intermittent Telltale data recorded on the mission. Had there been high wind speed events prior to this time, it would have been reflected as drops in the dust content of the fibres. This verifies that the collected Telltale data does indeed correctly display the wind speed and directional patterns in the northern polar regions of Mars.

Part Three
Electric Field Assisted Detachment

Chapter 6 - Electric Field

Assisted Detachment

Aeolian processes are responsible for massive dust movement on both Earth and Mars. In naturally occurring dust lifting phenomena on Earth, such as dust devils, dust storms and windblown dust, electric fields of 30-166 kV/m have been measured [Schmidt et al., 1998, Farrell et al., 2004, Jackson and Farrell, 2006]. To date no missions on the surface or in orbit of Mars have seen or been able to measure any indications of electrification in dust phenomena [Farrell and Desch, 2001], but recent Earth-based studies claim to have seen electrical discharge events from a Martian dust storm [Ruf et al., 2009] indicating that electrification might happen on Mars.

Experiments performed by Kok and Renno [2006] have demonstrated that electric fields lower the threshold friction wind speed for aeolian sand transport and can directly lift mineral particles (20-300 μm) from a metal surface. Rasmussen et al. [2009] examined wind and electric field interaction from a sand bed, showing that an electric field lowers the threshold wind speeds necessary for dust lifting. However, the mass transport rate was seen to diverge from the theoretical expression for electric fields between 160-190 kV/m, being lower than expected. Furthermore, when an electric field was applied to the sand bed, small piles were seen to form (cf. Fig. 6.1) probably due to dielectric particle chain formation in isolated areas [Jones, 1995, Merrison, private communication]. In combination, these effects show that the granular material may not be behaving like a conductive material.

The focus of this study is to quantify the electric field dependency of sand transport and how this is affected by the conductive properties of the surface. From basic electrostatic arguments it is believed that conductive surfaces will aid the removal of material from the surface, whereas the insulating (*i.e.* dielectric) surfaces will inhibit wind induced removal. Both conductive and insulating granular materials will be used in the study to further examine any influence of the electrical properties of the granular material in relation to the various surfaces.



Fig. 6.1: Close-up image of the sand bed showing the small piles which formed when an electrical field was applied [Merrison, private communication]

6.1 Electric field construction and discharge

Dust events on Earth, such as dust devils and dust storms, become electrically active by means of triboelectrification (contact electrification) [Eden and Vonnegut, 1973, Melnik and Parrot, 1998]. As grains collide, either via saltation or during suspension, they exchange electrons leading to size-dependent charging [Kok and Lacks, 2009]. The process leaves smaller grains negatively charged and larger grains positively charged [Forward et al., 2009]. Due to the difference in gravitational pull the smaller, negatively charged particles will remain suspended and the larger, positively charged particles will be dragged towards the ground creating a dipole moment, which results in an electric field (cf. Fig. 6.2) [Farrell et al., 2004].

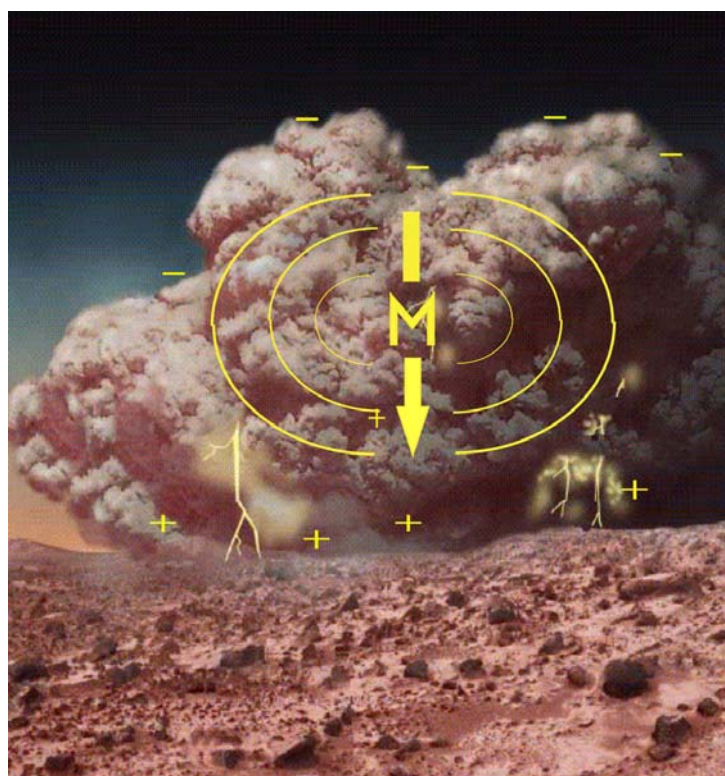


Fig. 6.2: An illustration of the dipole moment of an electrically charged dust storm with possible discharges [adapted from Farrell et al., 2001 and Farrell et al., 2004]

The same process is believed to happen on Mars, with a large degree of aeolian dust activity observed on the planet [Farrell et al., 2004, Merrison et al., 2004]. Experiments with Mars analogue dust have shown that the electrified grains consist of equal amounts of positive and negative charges [Merrison et al., 2006]. Particles in a Mars like atmosphere may charge as high as $10^4 e^-$ [Eden and Vonnegut, 1973] leading to the possibility of electrical breakdown and discharging in the dust event. The Martian arctic regolith was measured to have virtually no electrical conductivity by the Phoenix lander [Zent et al., 2010]. The lack of conductivity inhibits cloud-to-surface discharging, forcing the discharges upward creating cloud-to-ionosphere discharging [Farrell et al., 1999]. These events should be detectable from Earth by the emission of non-thermal microwave radiation, an event possibly observed by Ruf et al., [2009].

No spacecraft in orbit or on the surface of Mars has yet had the capability to measure electrified particulate charges or signs of electrical discharging and none have imaged such processes occurring in dust events on Mars [Farrell and Desch, 2001].

Electrical breakdown is a concern for laboratory experiments dealing with the electrification of particulates, regardless of the type of grain or atmospheric gasses used in the experiments. The significant parameter used when quantifying the threshold breakdown voltage within a gas is the product of the gas pressure and the electrode separation, a fact which was stated in Paschen's Law in 1889. It reflects the Townsend breakdown mechanism in gases, in which electron collisions between the electrodes lead to a cascade effect resulting in the discharging [Wiki - Townsend]. Townsend formulated a breakdown criterion from which the breakdown voltage can be determined [Husain and Nema, 1982]:

$$V_B = \frac{BPd}{k + \ln(Pd)} \quad (6.1)$$

where P is the pressure, d is electrode separation, B is a constant and k is defined as:

$$k = \ln(A/\ln(1+1/\gamma)) \quad (6.2)$$

where A is a constant and γ is the secondary ionization coefficient defined as the number of electrons released from the cathode of an ionization chamber per initial ionizing collision in the gas [Free Dictionary]. A , B and γ are experimentally determined for each specific type of (atmospheric) gas. For this study the breakdown voltage of interest is for atmospheric air at a pressure of 1013 mbar and an electrode separation of 5.5 cm, resulting in breakdown voltages of about 150 kV. However this result is only valid for polished surfaces as a larger surface roughness results in lower breakdown voltage due to the existence of microscopic field regions with electric fields larger than the macroscopic field [Pedersen, 1975, Misu et al., 2009, J. Böttiger, private communication]. In the case of this study breakdown was seen at voltages above 26 kV due to the use of a metal grid and two different types of roughened surfaces (see Sec. 6.4).

Fig. 6.3 shows the distinctive shape of the Paschen curve for CO_2 , the major constituent of the atmospheric gas on Mars. The breakdown curve for a Mars gas mixture was measured at low pressures due to a specific interest for Martian electrical discharging events [Snyder et al., 2008]. The breakdown values strongly depend on the type of event considered due to the difference in sizes between inter-particle discharging and atmospheric discharging. Breakdown voltages between lofted sand particles have characteristic length scales of hundreds of micrometers resulting in Pd values of less than one. In this region the breakdown voltage goes towards infinity making it difficult to create discharge between singular sand particles.

When viewing a dust devil or dust storm, we can easily have a characteristic height scale of several kilometers leading to Pd larger than those graphed in

Fig. 6.3. Exploiting the linear dependence of the Paschen curve at high values of Pd the breakdown voltage are calculated to be 25-40 kV/m for pressures of 5 to 7 mbar. If atmospheric discharge events were detected by Ruf et al. [2009] this implies that these values must have been exceeded.

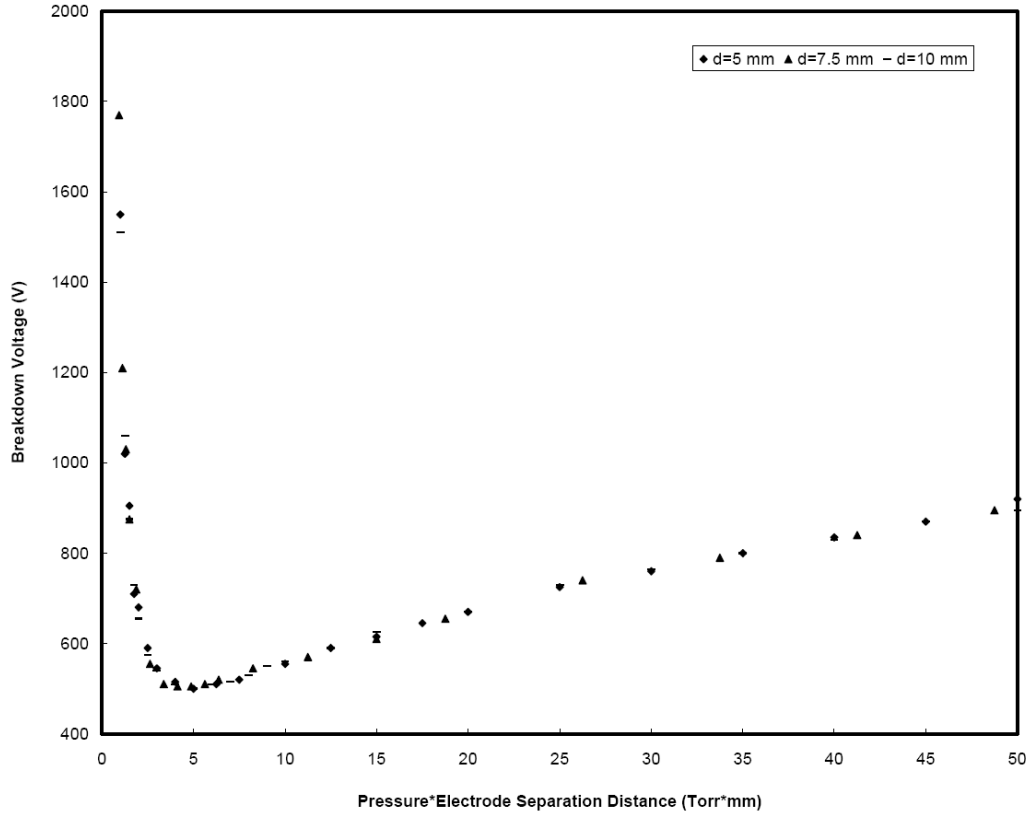


Fig. 6.3: Paschen curve illustrating breakdown voltages in Mars gas mixture at low pressures of 5.7 to 17.8 Torr (or 7.6 to 23.8 mbar) [Snyder et al., 2008].

6.2 Granular materials

Three granular materials were chosen for this study (cf. Fig. 6.4) based on size, electrical properties and morphology. The glass spheres, quartz particles and copper particles are all sand-sized with diameters of $\sim 100\text{-}125\ \mu\text{m}$ ensuring that they are dominated by gravity and not adhesion (see Chp. 2).

The main consideration for the electrical properties was to have both dielectric and conductive granular materials. Conductive materials have no internal electric fields due to the movement of free electrons within the material which leads electric charges. Copper was chosen for this study due to its conductive quality. Dielectrics become polarized rather than leading electric charge and have finite values of susceptibility. Usually the relative permittivity (or dielectric constant), ϵ_r , of the material is quoted, which is related to the susceptibility as [Griffiths, 1999]:

$$\epsilon_r = 1 + \chi_e \quad (6.3)$$

The glass spheres and quartz particles are both dielectrics with ϵ_r of 3.1 and 4.2, respectively [Clipper Controls]. In comparison, the bulk relative permittivity



Fig. 6.4: Microscope images of the three materials used in the study. From left to right: glass spheres in the size range 102-124 μm , quartz particles and copper particles of sizes 106-125 μm . All three pictures are on the same scale.

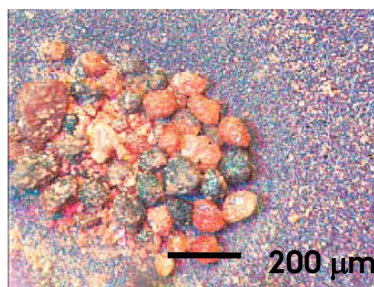


Fig. 6.5: Color composite image from the optical microscope onboard the Mars Phoenix mission [Goetz et al., 2010].

of the soils at the Mars Phoenix landing site was 2-3.5 [Zent et al., 2010], well within the dielectric range and comparable to the glass spheres and quartz particles. .

The glass spheres are the primary material in this study due to the extensive use of spherical particles in theoretical calculations of electrical properties. Electric force calculations have *e.g.* only been performed on spheres. The glass spheres have a mass density of 2.7 g/cm^3 , similar to quartz grains on Earth [Merrison et al., 2007], one of the components of silica, which is the most abundant type of mineral on all the terrestrial planets [de Pater and Lissauer, 2004]. The

quartz particles were chosen as a companion to the glass spheres to examine morphological differences in the behaviour of particles in electric fields. Interestingly the Mars Phoenix mission microscope has recently obtained images of the regolith particles (cf. Fig. 6.5) which show non-spherical particles, where most display rounded edges, probably due to aeolian processes [Goetz et al., 2010]. Thus morphological influence of the electric field on grain detachment on Mars should be illuminated by a combination of the results for the glass spheres and the quartz particles.

6.3 Electric particle theory

When working with electric fields we can categorize almost all materials as either conductive or dielectric [Griffiths, 1999]. This study will simulate a conducting or an insulating surface by means of a copper and a plastic sheet of material. To make it as difficult as possible for particles to roll over the surfaces, they have been roughened with sandpaper (size 60) resulting in a surface with a particular roughness height of about $265 \mu\text{m}$ [Wiki - Sandpaper]. The surfaces are inserted in a parallel plate electrode system (see Sec. 6.4) which supplies the electric field, making the conductive surface a part of the capacitor. The dielectric material will act as an insulator within the capacitor and will effectively change the permittivity of the capacitor [Griffiths, 1999]. The granular materials selected simulate dielectric and conductive materials, respectively, and in combination with the choice of surfaces they represent the four situations illustrated in Fig. 6.6.

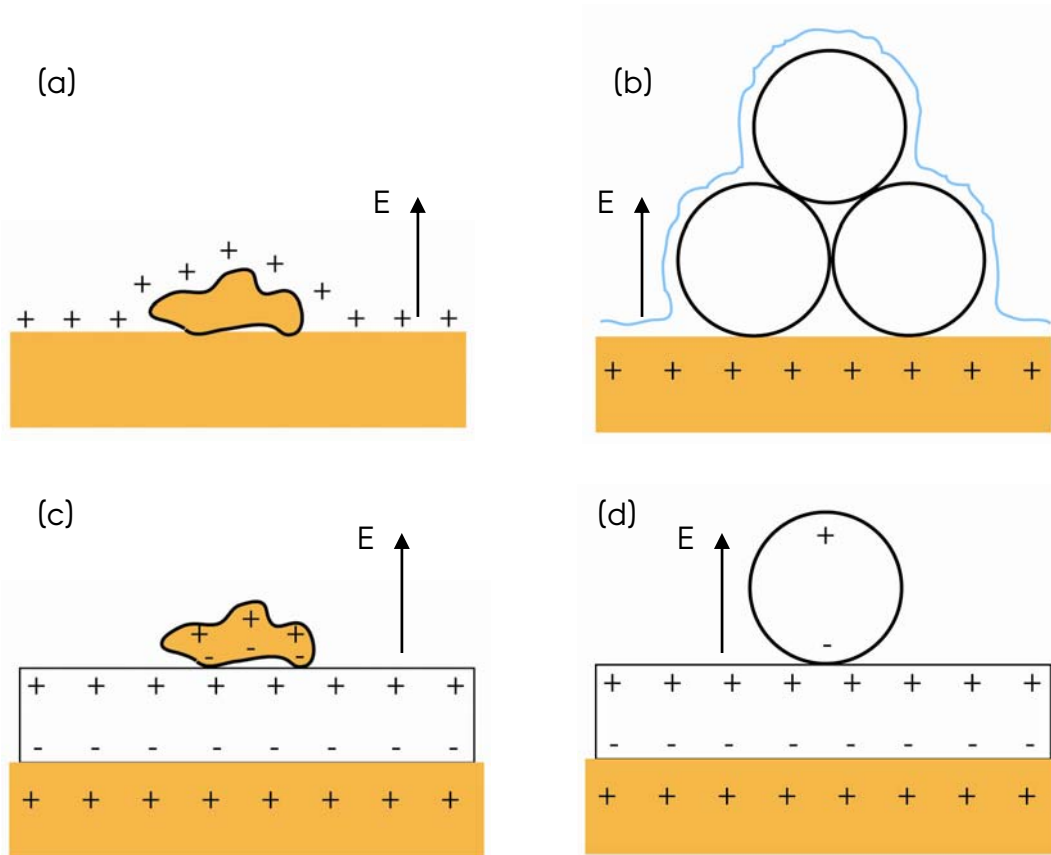


Fig. 6.6: Illustration of the four situations encountered at the lower plate of the parallel plate capacitor. The orange slab illustrates a conductive surface at a positive potential and the white slab is the dielectric material. In (a) and (c) we have a conductive particle (*i.e.* a metal) on the surface, while (b) and (d) display *e.g.* spherical glass spheres as the dielectric material.

In Fig. 6.6 (a) both the surface and grain are electrically conductive. The grain is electrically connected to the surface and therefore obtains the same charge density and the same sign as the surface. Since the particle is in the electric field which induced the charge originally it will experience an upward pointing electric force, which will facilitate the lifting of the particles [Kok and Renno, 2006]. This force gives rise to an electric stress felt by the grains of [Griffiths, 1999, Kok and Renno, 2006]:

$$\tau_E = \frac{F}{A} = \frac{\epsilon_0}{2} E^2 \quad (6.4)$$

where ϵ_0 is the permittivity of free space and E is the electric field in which the particle is located.

In Fig. 6.6 (b) the surface is conducting, but the grains are insulating. In these experiments however this becomes effectively the same case as (c). Due to the relative humidity of atmospheric air (typically around 60%), water molecules will adhere to the surface of most materials. Because liquid water normally contains ions, it is capable of carrying electric current and allows the otherwise insulating particles to become conductive to some degree [Griffiths,

1999]. Effectively the dielectric particles will behave like a conductive material on the surface thus getting the helpful lift from the electric forces.

Fig. 6.6 (c) demonstrates the case of a conductive particle separated from the charged conductive surface by a dielectric layer. Compared to the particle, the dielectric surface can be seen as thick and extending off to infinity in all directions, thus effectively blocking all paths for the electric field to reach the particle. The dielectric surface is placed inside the capacitor which leads to charge separation inside the dielectric. The particle does not obtain a net electric charge since the dielectric has no free electrons. Free electrons within the metal will be transported in order to eliminate the electric field produced by the capacitor within the metal and a dipole is thus created [Griffiths, 1999].

Fig. 6.6 (d) illustrates dielectric particles on a dielectric surface. As in the previous case the dielectric surface is polarized, but in this case the dielectric particle will also be polarized by being in the electric field. In effect the polarization will result in multipolar effects from both dielectrics, which will change the electric field, thus changing the polarization of the dielectrics, and so on [Jones, 1995]. Analogous to two magnetic dipoles, the induced electric dipole in the grain and the electric dipole of the surface will lead to a net attractive force between the two [Jones, 1995]. This is the case in figures (c) and (d) where the negative charges in the particle are closer to the positive layer of the surface than the positive charges of the particle leading to a net downward force making it more difficult for the wind shear to move the particle. The attractive force between the dielectrics can be calculated assuming the dielectric surface is not smooth and behaves like a layer of dielectric particles, an assumption met by the roughened dielectric surface of this study. The case of two dielectric spheres touching has been theoretically treated by Stoy [1995] and he calculates the attractive electric force using a multipolar approach:

$$F = F_{\infty}(\chi_e)\varepsilon E_0^2 R^2 \quad (6.5)$$

where F is the resulting attractive force, F_{∞} is the normalized force, ε is the permittivity of the medium outside the sphere, E_0 is the field strength of the electric field and R is the radius of the dielectric sphere. The normalized force can be obtained from the graph in Stoy [1995] of susceptibilities versus normalized force in the range $10^{-1} \leq \chi_e \leq 10^2$ (cf. Fig. 6.7). The area over which the shear stress affects the particle can be approximated to πR^2 resulting in a shear stress of:

$$\tau_E = F_{\infty}(\chi_e)\varepsilon E_0^2 / \pi \quad (6.6)$$

Determining susceptibilities of the granular materials used in the study is not a straight forward matter. Several databases provide generic numbers for various materials which are used as a proxy in this study to further the interpretation of results. Using an online database from [Clipper Controls] our granular materials fall nicely in the above mentioned range with susceptibilities of 2.1 and 3.2 for glass spheres and quartz particles,

respectively. Equation (6.5) is only applicable for the glass spheres for which the normalized force can be discerned to be about 1.1 N when consulting Fig. 6.7.

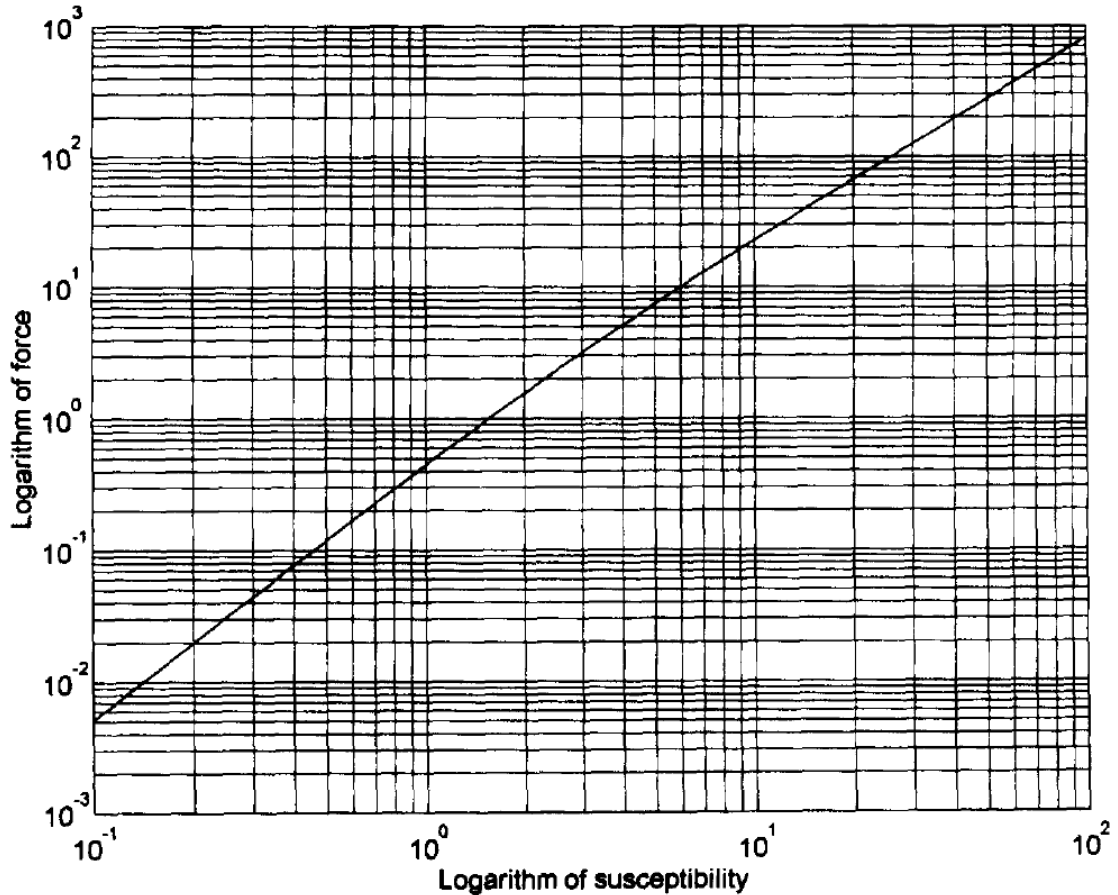


Fig. 6.7: Log-log graph of the attractive force between two touching spheres as a function of susceptibility ($10^{-1} \leq \chi_e \leq 10^2$) [Stoy, 1995]

6.4 Laboratory experiments

With the exception of the electrode system (a parallel plate capacitor type) the experimental techniques used in this study have all been presented in previous work. Fig. 6.8 pictures the parallel-plate capacitor which is used to generate a uniform electric field both schematically and fastened in the inner chamber of the Aarhus Mars Simulator wind tunnel (described in Chp. 5). A metal grid and aluminium plate constitutes the capacitor's top and bottom plate, respectively. The metal grid is overlain with a glass plate, to allow a clear view to the granular materials placed within the electric field. The schematic drawing illustrates the case of the conductive surface, with the copper plate being atop the plastic plate. The case of the insulating surface is achieved by switching the plastic and copper plates. The copper and aluminium plates are connected to the ground before a voltage, U , of 0-20 kV was set to the metal grid by means of the high voltage connection (*cf.* Fig. 6.8, bottom). This created a uniform electric field between the two plates over a distance, d , of 0.055 m. The electric field strength (kV/m) at the surface inside

the capacitor is calculated as U/d . A limit of 20 kV was set to avoid further discharging in the experiments.

With the chosen surface in place, four to six uniform circular deposits (spots) of the chosen granular material were deposited with 10 mm diameter and set apart by a distance of 10 mm. Excess material was removed to ensure that all spots were of the same height. Due to slight electrification of the particles during deposition the granular material was left undisturbed for two hours before experimentation. This was intended to be time enough to ensure that the materials were no longer charged, but not long enough for humidity in the air to cause cementation effects.

The electrode system with the granular samples was inserted into the wind tunnel and fastened to the sides of the chamber, ensuring minimal movement of the setup at high wind speeds. With the voltage set, the wind speeds were increased every 2 minutes in steps of 0.6 m/s from 1.3 m/s to between 5 or 8 m/s, depending on the experiment. The wind was turned off 4 minutes after the spots of material were observed to be removed.

A camera was used to document the experimental process by taking pictures every 30 seconds from when the electric field was turned on until after the wind had gone through the whole cycle. Calibration of the electric field strength was performed using a high voltage probe (Brandenburg Solid State HV Meter, model 88M) and wind speeds were calibrated using the LDA (described in Chp. 5).

Experiments were performed with each of the respective granular materials on the conductive plate where the wind tunnel was not started. Here the voltage was increased in single kilovolt steps in order to determine the threshold electric field strength needed to lift the particles from the surface. Table 6.1 provides a collected view of the experiments performed in this study.

6.4.1 Analysis

For the analysis the relevant part of the images taken during the experiments was the optical reflection of the spots of granular material as seen in the mirror. Examples of such images throughout an experiment can be seen in Fig. 6.9 (a-c). In (a) the spots are clearly visible, since we are below the threshold wind speed capable of moving these particles. In (b) the spots seem less clear, which is a result of a top layer of material being removed. This process was seen in all experiments, possibly indicating that the lower most grain layer is adhered more to the surface. This probably constitutes a source of systematic error in this study. In (c) The right most spot is completely removed and the rest are beginning to disappear or are almost gone. The process of removal typically started with the spots to the right, due to a slight tilt upward in the setup, resulting in higher electric field strengths to the right and slight asymmetry in the wind flow resulting in higher wind speed from right to left within the wind tunnel.

Table 6.1: Overview of the experiments performed. The first column is the type of granular material used, second column is the surface chosen and the third column is the voltage set for the individual experiment. “No field” means the experiment was run with wind alone while “Varying” means the experiment was run with no wind while the voltage was increased. The asterisk on the voltages show which experiments were performed by Brædstrup [2010].

Material	Surface	E [kV]	Material	Surface	E [kV]	
Glass spheres	Conductive	No field*	Quartz	Conductive	No field	
		6*			10	
		8*			Varying	
		10			Insulating	No field
		11				11
	Varying*	16				
	Insulating	No field*	6	Copper	Conductive	Varying
			9			20
			12			No field
			13			Insulating
14			No field			
16						
18						

For each experiment the first image was used to determine the area covered by each spot as can be seen in Fig. 6.9 (d). The average value of each pixel box (*e.g.* each spot) was then calculated for the red, blue and green filter for all images related to one experiment (a series). Even though the wind tunnel is cleaned before the experiments, high wind speeds can lift the small amounts of residual dust left in the wind tunnel. This can lead to changes in the color of the spots which are not related to the areal coverage in the single boxes. To overcome this problem a small box above every spot is used to calculate the average background intensity. To calculate the relative color index for each spot the average areal coverage was divided by the average background intensity.

An example of the resulting graph is seen in Fig. 6.10 for the right most spot in the experiment with glass spheres performed at 12 kV. For each color filter the difference between the average values at the beginning and end of the experiment was calculated. The color filter with the maximum difference was chosen in order to most precisely determine the image number corresponding to the median value of the relative color index. The image number found was correlated with logbooks to determine the removal wind speed, $U_{1/2}$.

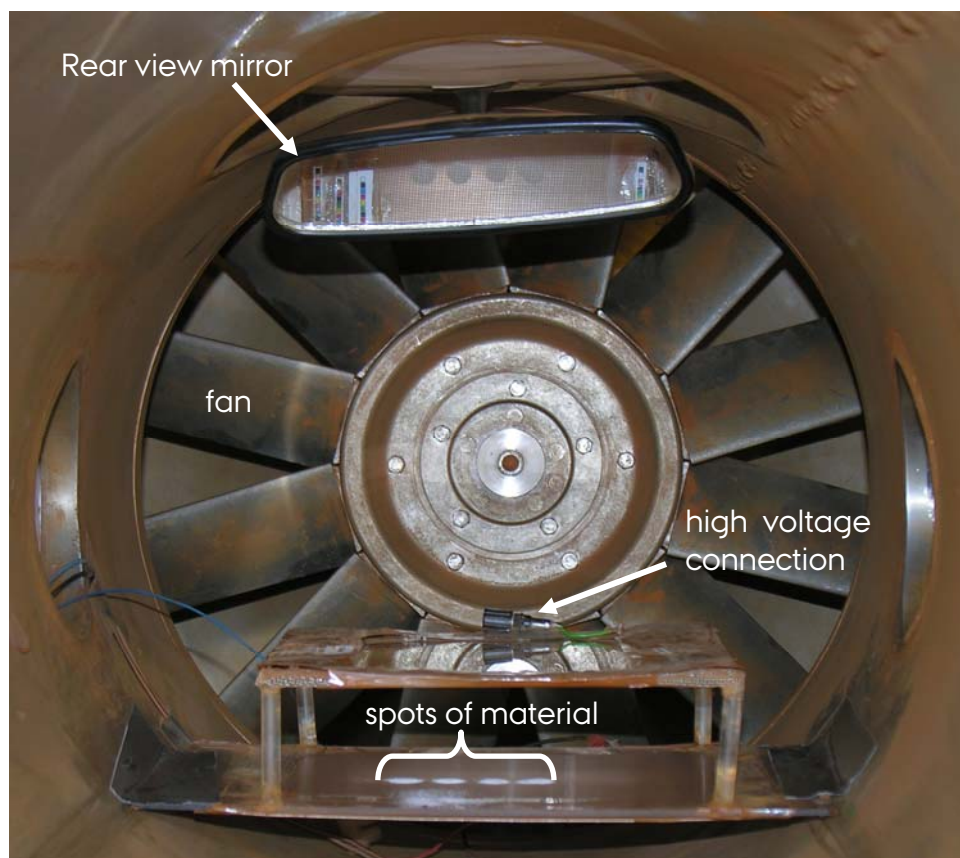
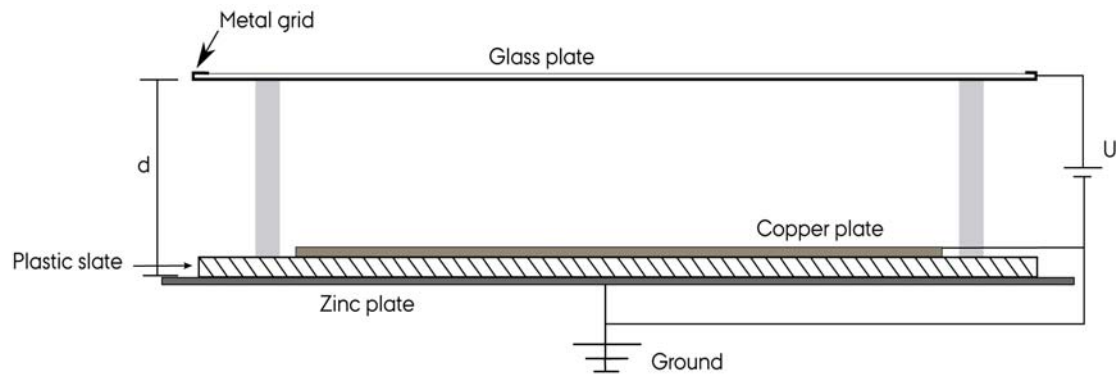


Fig. 6.8: Experimental setup for the electric field assisted detachment experiment. **Upper:** a schematic drawing of the setup used for this study with a conductive surface [Brædstrup, 2010]. U symbolizes the voltage received from the high voltage generator. The distance between plates, d , is 5.5 cm on average. **Lower:** picture of the setup securely fastened to the inside the wind tunnel in preparation for high wind speeds. The sample on the copper plate is reflected in the mirror. The wind tunnel fan is seen in the background.

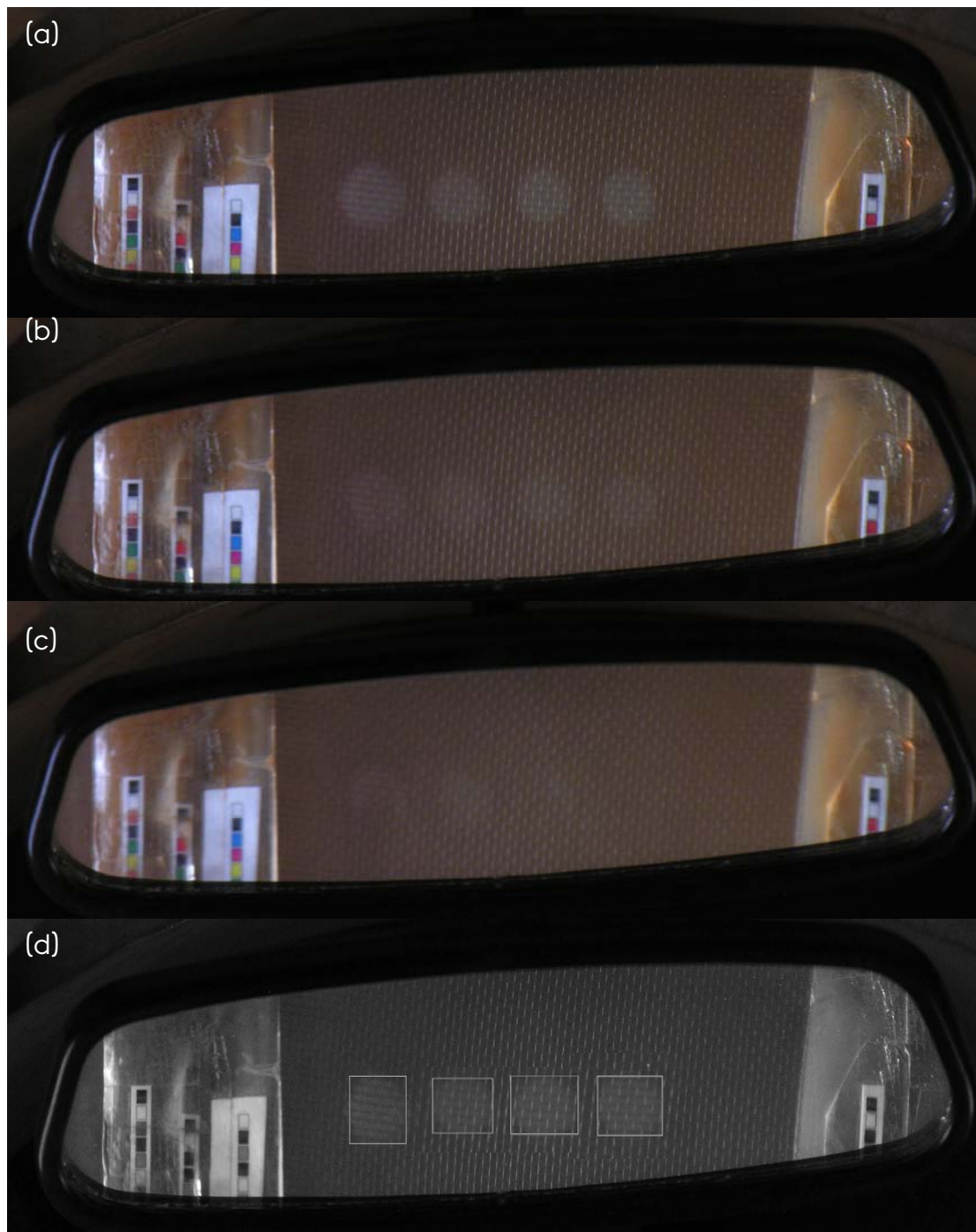


Fig. 6.9: Images through the mirror of three stages during an experiment (a-c) and from the analysis (d) with the glass spheres at 12 kV. **(a)** at 3 m/s no change is yet seen in the spots. **(b)** at 5.6 m/s a top layer seems to have been removed. **(c)** at 6.3 m/s the spots are being removed by the wind. The spots were always swept away in a right to left order. **(d)** an example of the boxes used in the analysis of the spots.

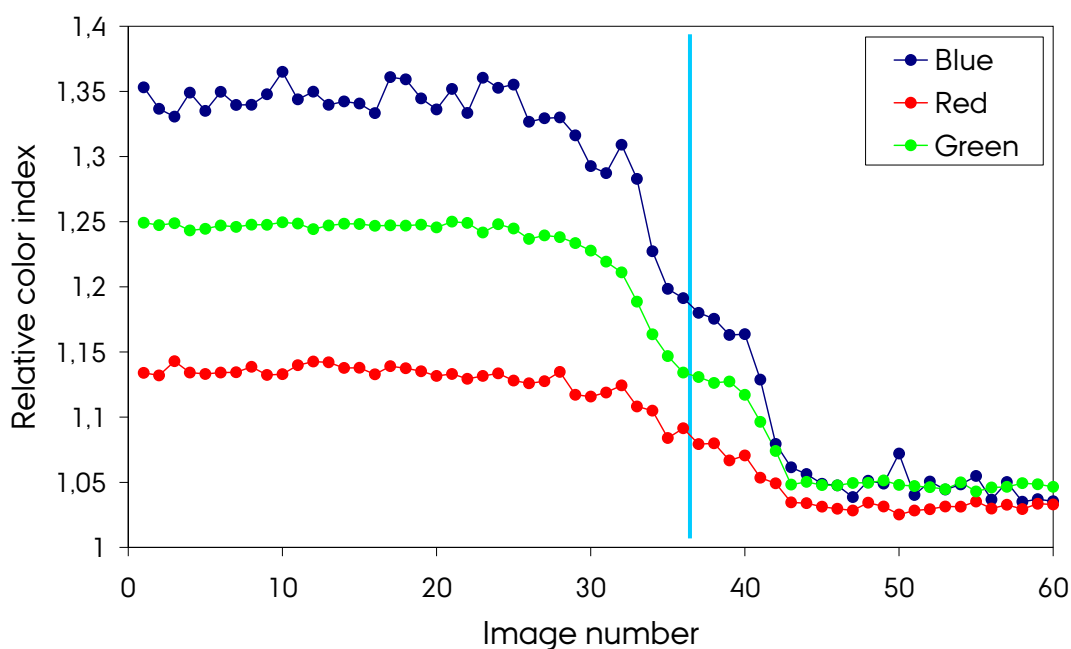


Fig. 6.10: Analysis data for the experiment with glass spheres at 12 kV for the right most spot of the four deposited. The colors indicate which filters have been analyzed and the light blue line indicates the image number found for half removal.

6.5 Experimental results and discussion

The left-to-right asymmetry in wind speeds along with the slight tilt of the setup results in a systematic shift in absolute shear stress, and thus removal wind speed, $U_{1/2}$, between the spots. Therefore the results can be summarized by viewing the data for one spot of each material. The optimum result would be a plot of shear stresses from wind and electric field, respectively.

In this study direct experimental determination of the susceptibility of the dielectric samples (glass and quartz) was not made. The generic values taken for the susceptibility of these materials constitute uncertainty in the absolute value of the normalized force. This is only the case for insulating particles on the insulating surface, but is a factor that prevents absolute stress values from being determined. For both conductive and insulating surfaces the electric field generated shear stress will be proportional to the square of the field strength and thus this quantity is plotted as a proxy for shear stress (see Sec. 6.3).

Calculating the wind shear stress is bound to a correct calculation of the friction wind speed, which is not easy to determine accurately [Merrison et al., 2007]. With a particle Reynolds number of 17 the drag coefficient is a complex function of the Reynolds number (and therefore the friction velocity) and empirical fitting should be employed (see Chp. 2). Earlier work by Merrison et al. [2007] employs such empirical fitting but at pressures of only 30 mbar, which makes the results invalid for this study as the parameters of the fit are pressure dependent. More work is needed in this area of aeolian processes before the wind shear stress can be calculated absolutely. As with the electric shear stress this study therefore uses the square of the wind speed as a proxy for the wind shear stress (see Chp. 2).

Fig. 6.11 summarizes the experiments with glass spheres using the data for the third spot from the left for the conductive and insulating surface, respectively. As the electric field is increased the difference in detachment wind speeds becomes evident. For the conductive surfaces, higher electric fields result in the particles becoming easier to detach from the surface, whereas the opposite effect is true for the insulating surface. Similar behaviour is seen for the quartz and copper particles (cf. Fig. 6.12 and Fig. 6.13) as would be expected.

This is an important observation as it implies that the electrical properties of a planetary surface must be determined in order to predict if electric fields will aid or hinder grain detachment. Previous experiments in assisted grain detachment have only dealt with conductive surfaces, a fact which means the results are applicable for only one type of surface. This study has shown that this would only be half the story since most surfaces are in reality a patchwork of conductive and insulating regions making studies of both cases important for understanding electric field assisted detachment.

In the case of Mars, the Phoenix lander measured no electrical conductivity for the north polar regolith [Zent et al., 2010], so electric field occurrences in dust storms and dust devils should actually further impede their own development by making it more difficult to loft surface materials. Relative humidity measurements from the Phoenix lander did however indicate that monolayers of water were deposited on the surface particles on a daily basis [Smith et al., 2009]. Already present in the soil are various salts [Kounaves et al., 2010] and in combination this could provide the means for inter-particle electric interaction increasing the regolith conductivity. This aspect is especially interesting in the study of Martian local and regional dust storms and their evolution into global dust storms. The south polar region has abundant amounts of hydrogen less than a meter below the surface [Mitrofanov et al., 2002], and assuming a similarity with the Phoenix landing site this could mean sub-surface ice, monolayers of water and plenty of salts in the soil increasing the conductivity. With the closer proximity of the south polar region of Mars to the Sun during the dust activity season (cf. Chp. 1) this might enhance the quantity of monolayers of water and thus salts, allowing the soil to rise above a threshold limit for conductivity enhancing the dust and sand lifting capabilities of already occurring dust storms.

The data for the glass spheres shown in Fig. 6.11 displays a clear suppression of electric field effect on the threshold shear stress, *i.e.* a plateau is seen before the onset of the expected electric field effects. The extent of this suppression is different for the insulating and conductive surfaces.

The cause for this suppression is not clear however it seems likely that it may be related to the use of multiple layers of grains in this study, rather than the ideal use of a single grain monolayer. This is due to the technical difficulty in producing such monolayers. The effect of multiple grain layers may allow for electrical interaction between the layers in response to an electric field, *i.e.* charge transport between the layers, which may complicate the desired electric field dependency. The effect is also seen clearly in the data from quartz particles on an insulating surface but seems absent from the data on copper particles on insulating surfaces, though there is a lack of sufficient data

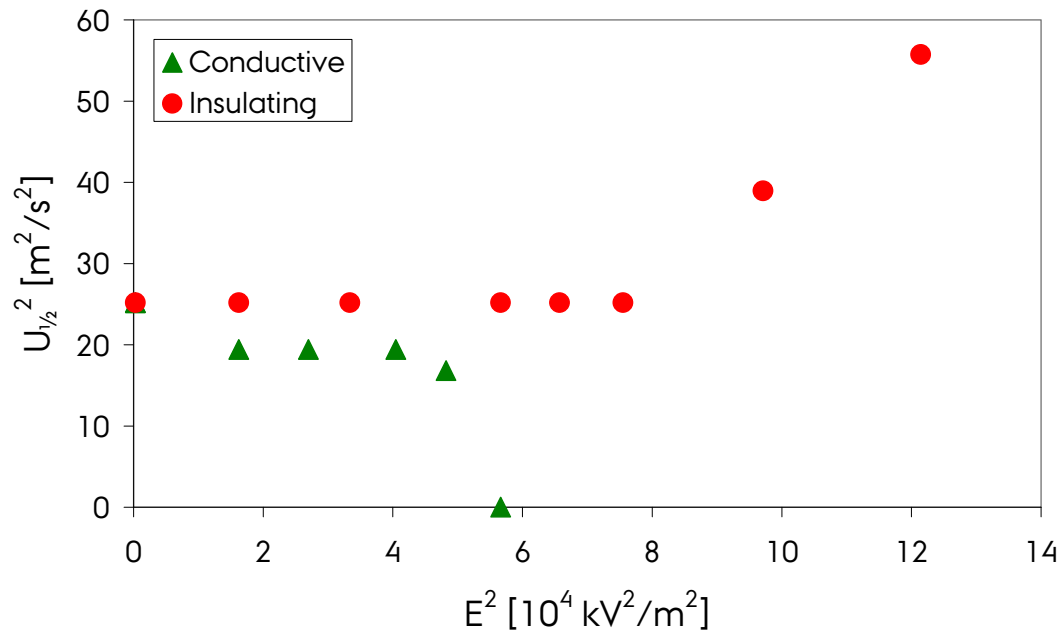


Fig. 6.11: The square of the electrical field plotted as a function of the square of the wind speed for the experiments using spherical glass spheres for the third spot from the left.

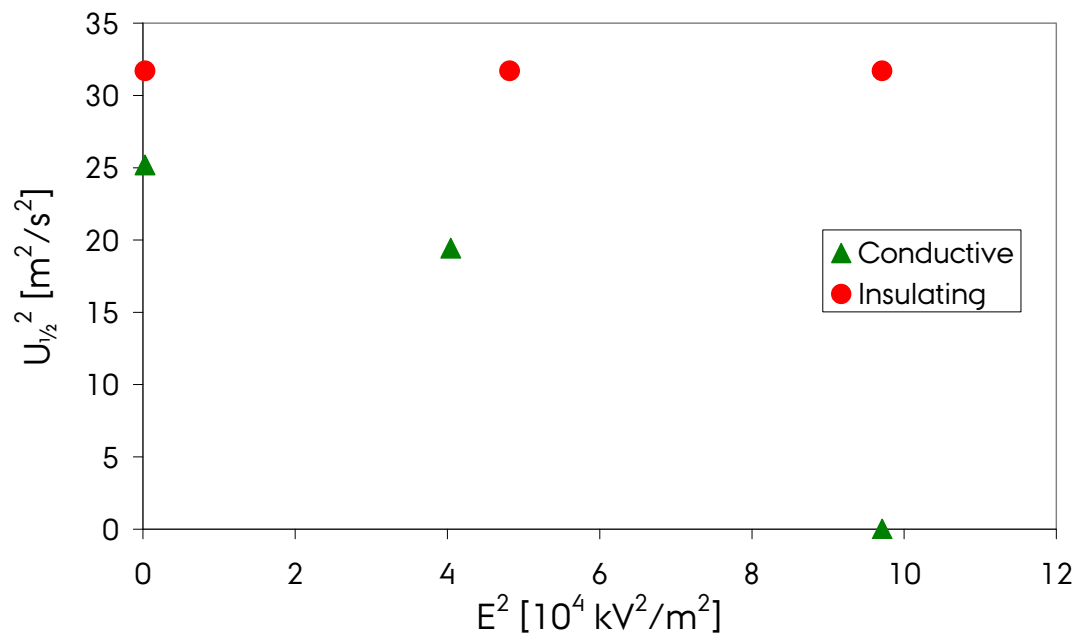


Fig. 6.12: The square of the electrical field plotted as a function of the square of the wind speed for the experiments using quartz particles for the third spot from the left.

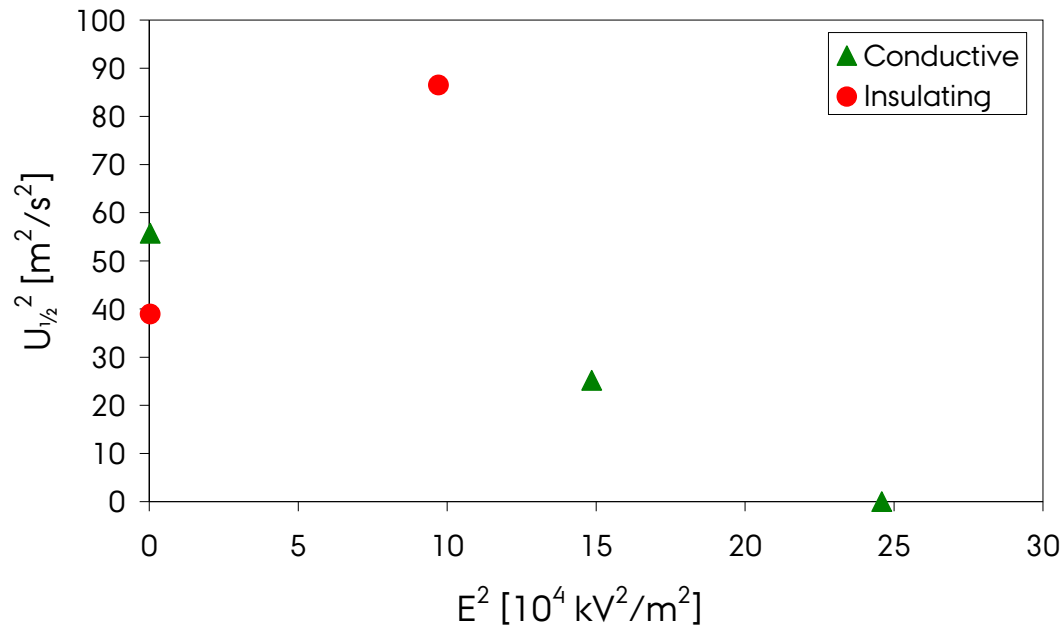


Fig. 6.13: The square of the electrical field plotted as a function of the square of the wind speed for the experiments using copper particles for the third spot from the left.

here. Repeating the experiments with true monolayers might eliminate the effect altogether.

In the experiment performed by Rasmussen et al. [2009] a similar suppression of electric field assisted entrainment was observed and may also be attributed to the use of multiple layers of probably partially conductive, partially insulating layers and regions *i.e.* they might have been seeing this very effect when they experienced lower transport values for mid-range electric fields. The explanation for the good agreement with theory seen in the measurements taken at high electric fields may be due to the electric field being capable of overcoming the insulating barriers *i.e.* an increase in conductivity of the granular material at high electric fields.

6.6 Conclusion

This study has looked into the possibility of different behaviour for electric field assisted detachment of surface materials based on the conductive properties of the surface. Three types of granular material, two dielectrics and one conductive, were deposited in a uniform electric field created by a parallel plate electrode system, which was inserted into a closed-circuit wind tunnel. An electric field was applied and by increasing the wind speeds, detachment thresholds were determined for various electric field strengths.

Analysis showed that there is a qualitative difference based on the electrical properties of the surface. Conductive surfaces were seen to aid in the detachment process whereas a dielectric surface inhibited the detachment. Previous experiments in assisted grain detachment have only dealt with conductive surfaces.

Due to the low humidity and probable low conductivity of the Martian regolith these experiments would suggest that typically electric fields on Mars,

generated for example by dust devils, would be expected to inhibit granular transport. The increased surface water content at the polar regions of Mars may raise the surface conductivity resulting in electric field enhancement. This might be a factor in the evolution of global dust storms in the south polar regions of Mars and should be studied further.

Improvements in this series of experiments could be the more precise deposition of granular materials resulting in monolayers of the materials used. The belief is that this would eliminate the unexpected plateau region in the observed data, which is possibly a result of inter-particle electrical interaction. It would also be interesting to run the experiments with spherical glass bubbles, which resemble aggregates on Mars [Merrison et al., 2007], since much of the lofted dust on Mars is believed to be detached from the surface as aggregates (cf. Chp. 2, 3). To make the experiment further resemble Mars it would be prudent to dry the materials used as the lack of water would change any possible inter-particle electrical interactions and possibly repeat the studies at lower pressure (in CO₂ gas).

In this study it was not possible to accurately determine absolute surface shear stress for the wind induced or electric field induced processes due to experimental difficulties in determining the relevant physical parameters. However the electric field and wind speed dependencies of these stresses are well known and relative comparison has been made here.

Summary

Chapter 7 - Summary

Decades of observations of aeolian activity on Mars has revealed a puzzling combination of active and inactive aeolian phenomena. Wind streaks on the surface of Mars exhibit variable behaviour, appearing and disappearing on time scales of weeks to years. Dust storms and dust devils are currently entraining, transporting and depositing dust on Mars. They are at least partly responsible for the constant resupply needed for the dust-laden atmosphere, but it is still unclear whether they are sufficient. None of the sand-blasted yardangs have shown any change and only a handful of dark sand dunes on Mars have been observed to move. Close-up investigations of dunes show indurated surfaces which hamper aeolian transport of sand and dust devil passages only disturb the surface dust.

Combined, these phenomena clearly indicate that the wind speeds on Mars are sufficient for dust detachment from the surface however sand grains seem to be mostly immobile at present times. Earth-based experiments show that only the highest wind speeds observed are occasionally close to the threshold for saltation and such rare saltation events are not enough to explain the active dust transport on Mars. A possible explanation is the entrainment and subsequent break-up of loosely bound sand-sized dust agglomerates. The building blocks for these agglomerates are seen on the surface and the vast quantity of dust devils could be responsible for making them airborne.

Despite the knowledge gained on aeolian activity on Mars, there are still many questions to be answered. The focus of this Ph.D. thesis has been to examine certain aspects of the wind related evolution of the Martian surface. This has been addressed by a combination of analysis of data from Mars and laboratory experiments performed at Aarhus University.

7.1 The Phoenix mission

The Phoenix mission was an unprecedented opportunity for an in situ exploration of a Martian polar region. Over 7700 images of the Telltale provided a detailed view of the wind regime in the area. The meteorological results showed clear diurnal and seasonal changes in winds, temperatures and pressures, some of which resembled measurements taken by earlier missions and some completely unique to this region. Especially unique are the seasonal changes in wind directions which overpower the previous diurnal cycle.

Observations of water vapour abundances, clouds and ground fog have been made from the beginning of surface exploration on Mars, but the Phoenix mission made great strides in understanding the surface-water interactions occurring in late summer by the observations of fall streaks and the proposal of multi-layer adsorption of water molecule.

The observation and analysis of dust storms occurring in the areas surrounding the north polar ice cap were the first of their kind and had not been possible without the context imaging performed from MARCI. The underlying mechanisms used to explain these were not new, however the

connection with wind speeds were not possible before the completion of the Phoenix mission.

The observations of aeolian activities such as dust storms and dust devils during the Phoenix mission were not followed by observations of aeolian surface features or movement. This was most likely due to the cloddy nature of the soils at the landing site accompanied by the seasonal cycle of freeze-thawing of the polygonal surface structure. Together they inhibit the creation of aeolian features as well as maintain a resurfacing rate too swift for aeolian features to build up.

The post Phoenix experiments on time-dependent dust accumulation (and removal) from the Telltale fibres showed that moderate wind speeds were sufficient to remove the accumulated dust, which seemed to have created agglomerates as it was deposited on the string. It was also shown that the intermittent nature of the Telltale dataset was not a cause for concern as no major events were missed.

7.2 Electric field assisted detachment

The experiments regarding electric field assisted detachment of sand particles showed a definite dependence of the electrical properties of the surface upon which particles reside. No previous experimental work has examined this difference which could be an important factor in electric field assisted dust lifting on Mars which is likely to occur in dust storms and dust devils. Most of the Martian soil is by all accounts very dry, and thus quite insulating, thus actually inhibiting surface detachment for sands.

Soils in the south polar regions might enjoy periods of heightened soil conductivity at perihelion due to extra solar heating as compared with the north polar region. It is suggested that this might be an added factor to the evolution of global dust storms from the local and regional dust storms in the south polar regions.

7.3 Future work

The Phoenix mission has presented many exciting aspects of further research just in the meteorological research area. New observations and analyses of developing dust storms around the North Pole would be beneficial now that another set of MARCI images exist for the recently ended northern hemisphere Martian spring and summer.

Development of a new and improved magnetic Telltale is underway in the Mars Simulation Group and it will hopefully be onboard on the next Mars mission from the European Space Agency.

The Phoenix mission made the first measurement of electrical conductivity of Martian soils in the northern polar region, but additional measurements, especially in the south polar regions are desirable. Measurements of electrical fields or electrical discharges in dust devils or storms on Mars are also a high priority. At present time the neither of the next Mars missions from ESA or NASA have the capability to perform these measurements.

Future efforts into the study of electric field assisted detachment have several prospects for improvements which should be considered. First is the creation of monolayers of sand since the presence of several layers of dust can create dielectric effects which are difficult to model. Elimination of this

effect would create a clearer image of the particle dependence on surface electrical properties.

Performing the experiments with glass bubbles rather than spheres would allow for the simulation of electrical field effects on the detachment of agglomerates on Mars. Seeming that the sand-sized dust agglomerates are the surface particle most likely lifted it would be very interesting to see if they exhibit the same dependence upon the electrical properties of surface soils.

For a better resemblance of Martian conditions the particles should be dried such that the electrical effects of surface water are not present. This is true for most regions on Mars, but it should be kept in mind that when examining dust lifting in the polar regions the Phoenix mission showed that molecular water films might form on surface particles changing the electrical properties of the surface.

Appendix

Appendix A - References

Almeida, M.P., E.J.R. Parteli, J.S. Andrade Jr., H.J. Herrmann (2008) Giant saltation on Mars, *Proc. Nat. Acad. Sci. USA*, *105*, 17, doi: 10.1073/pnas.0800202105

Alves M.A, F.T. Pihno, P.J. Oliveira (2001) The flow of viscoelastic fluids past a cylinder: finite-volume high-resolution methods, *J. Non-Newtonian Fluid Mech.*, *97*, 2-3, doi: 10.1016/S0377-0257(00)00198-1

Arvidson, R.E. et al. (2009) Results from the Mars Phoenix Lander Robotic Arm experiment, *J. Geophys. Res.*, *114*, E00E02, doi: 10.1029/2009JE0034

Bagnold, R.A. (1941) The Physics of Blown Sand and Desert Dunes, *Chapman & Hall*, ISBN: 0-412-10270-6

Balme, M., P.L. Whelley, R. Greeley (2003) Mars: Dust devil track survey in Argyre Planitia and Hellas Basin, *J. Geophys. Res.*, *108*, E8, doi: 10.1029/2003JE002096

Balme, M. and R. Greeley (2006) Dust devils on Earth and Mars, *Rev. Geophys.*, *44*, RG3003, doi: 10.1029/2005RG000188

Briggs, G., K. Klaasen, T. Thorpe, J. Wellman, W. Baum (1977) Martian Dynamical Phenomena During June-November 1976: Viking Orbiter Imaging Results, *J. Geophys. Res.*, *82*, 28, pp. 4,121 - 4,149, doi: 10.1029/JS082i028p04121

Brædstrup, C.F. (2010) Elektriske felters indflydelse på vinddrevet sand transport, Bachelor project, *Department of Physics and Astronomy*, Aarhus University

Bonitz, R.G. et al. (2008) NASA Mars 2007 Phoenix Lander Robotic Arm and Icy Soil Acquisition Device, *J. Geophys. Res.*, *113*, E00A01, doi: 10.1029/2007JE003030

Bourke, M.C., K.S. Edgett, B.A. Cantor (2008) Recent aeolian dune changes on Mars, *Geomorphology*, *94*, pp. 247 - 255, doi: 10.1016/j.geomorph.2007.05.012

Boynton, W.V. et al. (2001) Thermal and Evolved Gas Analyzer: Part of the Mars Volatile and Climate Surveyor integrated payload, *J. Geophys. Res.*, *106*, E8, doi: 10.1029/1999JE001153

Boynton, W.V. et al. (2002) Distribution of Hydrogen in the Near Surface of Mars: Evidence for Subsurface Ice Deposits, *Science*, *297*, 81, doi: 10.1126/science.1073722

Boynton, W.V. et al. (2009) Evidence for Calcium Carbonate at the Mars Phoenix Landing Site, *Science*, *325*, 61, doi: 10.1126/science.1172768

Cabrol, N.A. et al. (2008) Soil sedimentology at Gusev Crater from Columbia Memorial Station to Winter Haven, *J. Geophys. Res.*, *113*, E06S05, doi: 10.1029/2007JE002953

Conrath, B., R. Curran, R. Hanel, V. Kunde, W. Maguire, J. Pearl, J. Pirraglia, J. Wilker, T. Burke (1973) Atmospheric and Surface Properties of Mars Obtained by Infrared Spectroscopy on Mariner 9, *J. Geophys. Res.*, *78*, 20, doi: 10.1029/JB078i020p04267

Cutts, J.A. and R.S.U. Smith (1973) Eolian Deposits and Dunes on Mars, *J. Geophys. Res.*, *78*, 20, doi:10.1029/JB078i020p04139

de Pater, I. and J.J. Lissauer (2004) Planetary Sciences, *Cambridge University Press*, ISBN: 0-521-48219-4

Drube, L. et al. (2010) Magnetic and optical properties of airborne dust and settling rates of dust at the Phoenix landing site, *J. Geophys. Res.*, *115*, E00E23, doi: 10.1029/2009JE003419

Eden, H.F. and B. Vonnegut (1973) Electrical Breakdown Caused by Dust Motion in Low-Pressure Atmospheres: Considerations for Mars, *Science*, *180*, pp. 962 – 963, doi: 10.1126/science.180.4089.962

Ellehoj, M.D. et al. (2010) Convective vortices and dust devils at the Phoenix Mars mission landing site, *J. Geophys. Res.*, *115*, E00E16, doi: 10.1029/2009JE003413

Farrell, W.M., M.L. Kaiser, M.D. Desch, J.G. Houser, S.A. Cummer, D.M. Wilt, G.A. Landis (1999) Detecting electrical activity from Martian dust storms, *J. Geophys. Res.*, *104*, 2, doi: 10.1029/98JE02821

Farrell, W.M. and M.D. Desch (2001) Is there a Martian atmospheric circuit?, *J. Geophys. Res.*, *106*, E4, doi: 10.1029/2000JE001271

Farrell, W.M. et al. (2004) Electric and magnetic signatures of dust devils from the 2000–2001 MATADOR desert tests, *J. Geophys. Res.*, *109*, E03004, doi: 10.1029/2003JE002088

Feldman, W.C. et al. (2002) Global Distribution of Neutrons from Mars: Results from Mars Odyssey, *Science*, *297*, 75, doi: 10.1126/science.1073541

Ferri, F., P.H. Smith, M. Lemmon, N.O. Renno (2003) Dust devils as observed by Mars Pathfinder, *J. Geophys. Res.*, *108*, E12, doi: 10.1029/2000JE001421

Fisher, J.A., M.I. Richardson, C.E. Newman, M.A. Szwast, C. Graf, S. Basu, S.P. Ewald, A.D. Toigo, R.J. Wilson (2005) A survey of Martian dust devil activity

using Mars Global Surveyor Mars Orbiter Camera images, *J. Geophys. Res.*, *110*, E03004, doi: 10.1029/2003JE002165

Forward, K.M., D.J. Lacks, R.M. Sankaran (2009) Charge Segregation Depends on Particle Size in Triboelectrically Charged Granular Materials, *Phys. Rev. Lett.*, *102*, 028001, doi: 10.1103/PhysRevLett.102.028001

Fox, R.W. and A.T. McDonald (1985) Introduction to Fluid Mechanics, *John Wiley and Sons*, 3rd edition, ISBN: 0-471-82106-3

Gierasch, P., and R. Goody (1968) A study of the thermal and dynamical structure of the Martian lower atmosphere, *Planet. Space Sci.*, *16*, doi: 10.1016/0032-0633

Gierasch, P.J. (1974) Martian Dust Storms, *Rev. Geophys. Space Sci.*, *12*, 4, doi: 10.1029/RG012i004p00730

Grant, J.A. and P.H. Schultz (1987) Possible Tornado-Like Tracks on Mars, *Science*, *237*, 4817, pp. 883 – 885, doi: 10.1126/science.237.4817.883

Greeley, R. (1979) Silt-clay aggregates on Mars, *J. Geophys. Res.*, *84*, B11, doi: 10.1029/JB084iB11p06248

Greeley, R., R. Leach, B. White, J. Iversen, J. Pollack (1980) Threshold windspeeds for sand on Mars: Wind tunnel simulations, *Geophys. Res. Lett.*, *7*, 2, doi: 10.1029/GL007i002p00121

Greeley, R. and J.D. Iversen (1985) Wind as a geological process on Earth, Mars, Venus and Titan, *Cambridge University Press*, ISBN: 0-521-24385-8

Greeley, R., N. Lancaster, S. Lee (1992) Martian Aeolian Processes, Sediments, and Features, in *Mars*, edited by H.H. Kiefer et al., pp. 730-766, *University of Arizona Press*, ISBN: 0-8165-1257-4

Greeley, R., M. Kraft, R. Sullivan, G. Wilson, N. Bridges, K. Herkenhoff, R.O. Kuzmin, M. Malin, W. Ward (1999) Aeolian features and processes at the Mars Pathfinder landing site, *J. Geophys. Res.*, *104*, E4, doi: 10.1029/98JE02553

Greeley, R., M.R. Balme, J.D. Iversen, S. Metzger, R. Mickelson, J. Phoreman, B. White (2003) Martian dust devils: Laboratory simulations of particle threshold, *J. Geophys. Res.*, *108*, E5, doi: 10.1029/2002JE001987

Greeley, R. et al. (2004) Wind-related Processes Detected by the Spirit Rover at Gusev Crater, Mars, *Science*, *305*, 810, doi: 10.1126/science.1100108

Greeley, R. et al., (2006) Gusev crater: Wind-related features and processes observed by the Mars Exploration Rover Spirit, *J. Geophys. Res.*, *111*, E02S09, doi: 10.1029/2005JE002491

Griffiths, D.J. (1999) Introduction to Electrodynamics, 3rd edition. *Prentice-Hall Inc.*, New Jersey, ISBN: 0-13-805326-X

Goetz, W. et al. (2010) Microscopy analysis of soils at the Phoenix landing site, Mars: Classification of soil particles and description of their optical and magnetic properties, *J. Geophys. Res.*, *115*, E00E22, doi: 10.1029/2009JE003437

Gunnlaugsson, H.P., K.M. Kinch, M.B. Madsen, J.P. Merrison, P. Nørnberg, H. Wahlgreen (2004) Device for measuring surface accumulation of dust: applications for future magnetic properties experiments on Mars, *Planetary and Space Science*, *52*, doi: 10.1016/j.pss.2004.01.002

Gunnlaugsson, H.P. et al. (2008) Telltale wind indicator for the Mars Phoenix lander, *J. Geophys. Res.*, *113*, E00A04, doi: 10.1029/2007JE003008

Hargraves, R.B., D.W. Collinson, R.E. Arvidson, C.R. Spitzer (1977) The Viking Magnetic Properties Experiment: Primary Mission Results, *J. Geophys. Res.*, *82*, 28, pp. 4,547-4,558, doi: 10.1029/JS082i028p04547

Hayward, R.K., K.F. Mullins, L.K. Fenton, T.M. Hare, T.N. Titus, M.C. Bourke, A. Colaprete, P.R. Christensen (2007) Mars Global Digital Dune Database and initial science results, *J. Geophys. Res.*, *112*, E11007, doi: 10.1029/2007JE002943

Hecht, M.H. et al. (2008) Microscopy capabilities of the Microscopy, Electrochemistry, and Conductivity Analyzer, *J. Geophys. Res.*, *113*, E00A22, doi: 10.1029/2008JE003077

Hecht, M.H. et al. (2009) Detection of Perchlorate and the Soluble Chemistry of Martian Soil at the Phoenix Lander Site, *Science*, *325*, 64, doi: 10.1126/science.1172466

Herkenhoff, K. E. et al. (2003) Athena Microscopic Imager investigation, *J. Geophys. Res.*, *108*, E12, 8065, doi: 10.1029/2003JE002076.

Hess, S.L., R.M. Henry, C.B. Leovy, J.A. Ryan, J.E. Tillman (1977) Meteorological Results From the Surface of Mars: Viking 1 and 2, *J. Geophys. Res.*, *82*, 28, pp. 4,559 – 4,574, doi: 10.1029/JS082i028p04559

Hess, S.L., R.M. Henry, J.E. Tillman (1979) The Seasonal Variation of Atmospheric Pressure on Mars as Affected by the South Polar Cap, *J. Geophys. Res.*, *84*, B6, doi: 10.1029/JB084iB06p02923

Holstein-Rathlou, C. et al. (2010) Winds at the Phoenix landing site, *J. Geophys. Res.*, *115*, E00E18, doi: 10.1029/2009JE003411

Hudson, T.L., A. Zent, M.H. Hecht, S. Wood, D. Cobos (2009) Near-Surface Humidity at the Phoenix Landing Site as Measured by the Thermal and

Electrical Conductivity Probe (TECP), *40th Lunar and Planetary Science Conference*, abstract 1804

Husain, E. and R.S. Nema (1982) Analysis of Paschen curves for Air, N₂ and SF₆ using the Townsend Breakdown Equation, *IEEE Transactions on Electrical Insulation, EI-17*, 4, doi: 10.1109/TEI.1982.298506

Jackson, T.L. and W.M. Farrell (2006) Electrostatic Fields in Dust Devils: An Analog to Mars, *IEEE Transactions on Geoscience and Remote Sensing*, 44, 10, doi: 10.1109/TGRS.2006.875785

Jones, T.B. (1995) Electromechanics of Particles, 1st edition, *Cambridge University Press*, ISBN: 0-521-43196-4

Keller, H.U. et al. (2008) Phoenix Robotic Arm Camera, *J. Geophys. Res.*, 113, E00A17, doi: 10.1029/2007JE003

Kieffer, H.H., S.C. Chase Jr., E. Miner, G. Münch, G. Neugebauer (1973) Preliminary Report on Infrared Radiometric Measurements from the Mariner 9 spacecraft, *J. Geophys. Res.*, 78, 20, doi: 10.1029/JB078i020p04291

Kieffer, H.H., B.M. Jakosky, C.W. Snyder, M.S. Matthews (1992) Mars, *Arizona University Press*, ISBN: 0-8165-1257-4

Kieffer, H. H., P. R. Christensen, T. N. Titus (2006) CO₂ jets formed by sublimation beneath translucent slab ice in Mars' seasonal south polar ice cap, *Nature*, 442, doi: 10.1038/nature04945

Kliore, A.J., G. Fjeldbo, B.L. Siedel, M.J. Sykes, P.M. Woiceshyn (1973) S Band Radio Occultation Measurements of the Atmosphere and Topography of Mars with Mariner 9: Extended Mission Coverage of Polar and Intermediate Latitudes, *J. Geophys. Res.*, 78, 20, doi: 10.1029/JB078i020p04331

Kok, J.F. and N.O. Renno (2006) Enhancement of the emission of mineral dust aerosols by electric forces, *Geophys. Res. Letters*, 33, L19S10, doi: 10.1029/2006GL026284

Kok, J.F. and D.J. Lacks (2009) Electrification of granular systems of identical insulators, *Phys. Rev. E*, 79, 051304, doi: 10.1103/PhysRevE.79.051304

Kok, J.F. (2010) Difference in the Wind Speeds Required for Initiation versus Continuation of Sand Transport in Mars: Implications for Dunes and Dust Storms, *Phys. Rev. Lett.*, 104, doi: 10.1103/PhysRevLett.104.074502

Kounaves, S.P. et al. (2009) The MECA Wet Chemistry Laboratory on the 2007 Phoenix Mars Scout Lander, *J. Geophys. Res.*, 114, E00A19, doi: 10.1029/2008JE003084

Lancaster, N. and R. Greeley (1990) Sediment Volume in the North Polar Sand Seas of Mars, *J. Geophys. Res.*, *95*, B7, doi: 10.1029/JB095iB07p10921

Larsen, S.E., H.E. Jørgensen, L. Landberg, J.E. Tillman (2002) Aspects of the Atmospheric Surface layers on Mars and Earth, *Boundary-Layer Meteorol.*, *105*, 3, pp. 451-470, doi: 10.1023/A:1020338016753

Larsen, S.E. (2006) Microscale Meteorology (lecture notes) *Risø National Laboratory*, Denmark (<http://www.risoe.dk/vea/thesis/LecturesCourses.htm>)

Leer, K. et al. (2008) Magnetic properties experiments and the Surface Stereo Imager calibration target onboard the Mars Phoenix 2007 Lander: Design, calibration, and science goals, *J. Geophys. Res.*, *113*, E00A16, doi: 10.1029/2007JE003014

Lemmon, M.T. et al. (2004) Atmospheric Imaging Results from the Mars Exploration Rovers: Spirit and Opportunity, *Science*, *306*, 1753, doi: 10.1126/science.1104474

Lemmon, M.T. et al. (2008) The Phoenix Surface Stereo Imager (SSI) Investigation, *39th Lunar and Planetary Science Conference*, abstract 2156

Leovy, C.B. (1979) Martian Meteorology, *Ann. Rev. Astron. Astrophys.*, *17*, pp. 387-413

Leovy, C. B. (1981), Observations of Martian tides over two annual cycles, *J. Atmos. Sci.*, *38*, doi: 10.1175/1520-0469

Lewis, S.R., M. Collins, P.L. Read, F. Forget, F. Hourdin, R. Fournier, C. Hourdin, O. Talagrand, J.-P. Huot (1999) A climate database for Mars, *J. Geophys. Res. Planets*, *104*, E10, doi: 10.1029/1999JE001024

Lindal, G.F, H.B. Hotz, D.N. Sweetnam, Z. Shippony, J.P. Brenkle, G.V. Hartsell, R.T. Spear, W.H. Michael (1979) Viking Radar Occultation Measurements of the Atmosphere and Topography of Mars: Data Acquired During 1 Martian Year of Tracking, *J. Geophys. Res.*, *84*, B14, doi: 10.1029/JB084iB14p08443

Martin, L.J. (1974) The Major Martian Dust Storms of 1971 and 1973, *Icarus*, *23*, doi: 10.1016/0019-1035(74)90108-0

Martin, L.J. and R.W. Zurek (1993) An Analysis of the History of Dust Activity on Mars, *J. Geophys. Res.*, *98*, E2, doi: 10.1029/92JE02937

McCauley, J.F. (1973) Mariner 9 Evidence for Wind Erosion in the Equatorial and Mid-Latitude Regions of Mars, *J. Geophys. Res.*, *78*, 20, doi: 10.1029/JB078i020p04123

McIlveen, R. (1992) Fundamentals of Weather and Climate, *Chapman & Hall*, pp. 299-313, ISBN: 0-412-41160-1

-
- Mellon, M.T., M.C. Malin, R.E. Arvidson, M.L. Searls, H.G. Sizemore, T.L. Heet, M.T. Lemmon, H.U. Keller, J. Marshall (2009) The periglacial landscape at the Phoenix landing site, *J. Geophys. Res.*, *114*, E00E06, doi: 10.1029/2009JE003418
- Melnik, O. and M. Parrot (1998) Electrostatic discharge in Martian dust storms, *J. Geophys. Res.*, *103*, A12, doi: 10.1029/98JA01954
- Merrison, J.P., J. Jensen, K. Kinch, R. Mugford, P. Nørnberg (2004) The electrical properties of Mars analogue dust, *Planetary and Space Science*, *52*, doi: 10.1016/j.pss.2003.11.003
- Merrison, J.P., H.P. Gunnlaugsson, K. Kinch, T.L. Jacobsen, A.E. Jensen, P. Nørnberg, H. Wahlgreen (2006) An integrated laser anemometer and dust accumulator for studying wind-induced dust transport on Mars, *Planetary and Space Science*, *54*, doi: 10.1016/j.pss.2006.05.026
- Merrison, J.P., H.P. Gunnlaugsson, P. Nørnberg, A.E. Jensen, K.R. Rasmussen (2007) Determination of the wind induces detachment threshold for granular material on Mars using wind tunnel simulations, *Icarus*, *191*, doi: 10.1016/j.icarus.2007.04.035
- Merrison, J. P., H. Bechtold, H. Gunnlaugsson, A. Jensen, K. Kinch, P. Nørnberg, K. Rasmussen (2008) An enviromental simulation wind tunnel for studying aeolian transport on Mars, *Planet. Space Sci.*, *56*, doi: 10.1016/j.pss.2007.11.007
- Misu, T., T. Uehara, S. Ono, M. Goto, T. Arai (2009) Discharge properties of CVD diamond electrodes by O₂ plasma treatment, *19th International Symposium on Plasma Chemistry*, abstract 784
- Mitrofanov, I. et al. (2002) Maps of Subsurface Hydrogen from the High Energy Neutron Detector, Mars Odyssey, *Science*, *297*, 78, doi: 10.1126/science.1073616
- Moore, H.J. and B.M. Jakosky (1989) Viking Landing Sites, Remote-Sensing Observations, and Physical Properties of Martian surface Materials, *Icarus*, *81*, doi: 10.1016/0019-1035(89)90132-2
- Moore, H.J., D.B. Bickler, J.A. Crisp, H.J. Eisen, J.A. Gensler, A.F.C. Haldemann, J.R. Matijevic, L.K. Reis, F. Pavlics (1999) Soil-like deposits observed by Sojourner, the Pathfinder rover, *J. Geophys. Res.*, *104*, E4, doi: 10.1029/1998JE900005
- Moores, J.E., M.T. Lemmon, P.H. Smith, L. Komguem, J.A. Whiteway (2010) Atmospheric dynamics at the Phoenix landing site as seen by the Surface Stereo Imager, *J. Geophys. Res.*, *115*, E00E08, doi: 10.1029/2009JE003409

- Newman, C.E., S.R. Lewis, P.L. Read (2005) The atmospheric circulation and dust activity on different orbital epochs on Mars, *Icarus*, 174, pp. 135 – 160, doi: 10.1016/j.icarus.2004.10.023
- Nørnberg, P., H.P. Gunnlaugsson, J.P. Merrison, A.L. Vendelboe (2009) Salten Skov I: A Martian magnetic dust analogue, *Planetary and Space Science*, 57, doi: 10.1016/j.pss.2008.08.017
- Pedersen, A (1975) The Effect of Surface Roughness on Breakdown in SF₆, *IEEE Trans. Power App. Syst., PAS-94*, 5, doi: 10.1109/T-PAS.1975.32019
- Pollack, J.B., D. Colburn, R. Kahn, J. Hunter, W. van Camp, C.E. Carlston, M.R. Wolf (1977) Properties of Aerosols in the Martian Atmosphere, as Inferred from Viking Lander Imaging Data, *J. Geophys. Res.*, 82, 28, doi:10.1029/J082i028p04479
- Portyankina, G., W.J. Markiewicz, N. Thomas, C.J. Hansen, M. Milazzo (2010) HiRISE observations of gas sublimation-driven activity in Mars' southern polar regions: III. Models of processes involving translucent ice, *Icarus*, 205, doi: 10.1016/j.icarus.2009.08.029
- Rajani, B.N., A. Kandasamy, Sekhar Majumdar (2009) Numerical simulation of laminar flow past a circular cylinder, *Applied Mathematical Modelling*, 33, doi: 10.1016/j.apm.2008.01.017
- Rasmussen, K.R., J.F. Kok, J.P. Merrison (2009) Enhancement in wind-driven sand transport by electric fields, *Planetary and Space Science*, 57, doi: 10.1016/j.pss.2009.03.001
- Ruf, C., N.O. Renno, J.F. Kok, E. Bandelier, M.J. Sander, S. Gross, L. Skjerve, B. Cantor (2009) Emission of non-thermal microwave radiation by a Martian dust storm, *Geophys. Res. Lett.*, 36, L13202, doi: 10.1029/2009GL038715
- Ryan, J.A. and R.M. Henry (1979) Mars Atmospheric Phenomena During Major Dust Storms as Measured at Surface, *J. Geophys. Res.*, 84, B6, doi: 10.1029/JB084iB06p02821
- Ryan, J.A. and R.D. Lucich (1983) Possible Dust Devils, Vortices on Mars, *J. Geophys. Res.*, 88, C15, doi: 10.1029/JC088iC15p11005
- Sagan, C. et al. (1973) Variable Features on Mars, 2, Mariner 9 Global Results, *J. Geophys. Res.*, 78, 20, doi: 10.1029/JB078i020p04163
- Salby, M.L. (1996) Fundamentals of Atmospheric Physics, *Academic Press*, pp. 405-423, ISBN: 0-12-615160-1
- Schofield, J.T., J.R. Barnes, D. Crisp, R.M. Haberle, S. Larsen, J.A. Magalhães, J.R. Murphy, A. Sieff, G. Wilson (1997) The Mars Pathfinder Atmospheric Structure Investigation/Meteorology (ASI/MET) Experiment, *Science*, 278, doi: 10.1126/science.278.5344.1752

-
- Schmidt, D. S., R.A. Schmidt, J.D. Dent (1998) Electrostatic force on saltating sand, *J. Geophys. Res.*, *103*, D8, doi: 10.1029/98JD00278
- Shao, Y. and H. Lu (2000) A simple expression for the wind erosion threshold friction velocity, *J. Geophys. Res.*, *105*, D17, doi: 10.1029/2000JD900304
- Shaw, A., R.E. Arvidson, R. Bonitz, J. Carsten, H.U. Keller, M.T. Lemmon, M.T. Mellon, M. Robinson, A. Trebi-Ollennu (2009) Phoenix soil physical properties investigation, *J. Geophys. Res.*, *114*, E00E05, doi: 10.1029/2009JE003455
- Smith, M.D., B.J. Conrath, J.C. Pearl, P.R. Christensen (2002) Thermal Emission Spectrometer Observations of Martian Planet-Encircling Dust Storm 2001A, *Icarus*, *157*, doi: 10.1006/icar.2001.6797
- Smith, P.H. et al. (2008) Introduction to special section on the Phoenix Mission: Landing Site Characterization Experiments, Mission Overviews, and Expected Science, *J. Geophys. Res.*, *113*, E00A18, doi: 10.1029/2008JE003083
- Smith, P.H. et al. (2009) H₂O at the Phoenix Landing Site, *Science*, *325*, 58, doi: 10.1126/science.1172339
- Snyder, C.W. (1979) The Planet Mars as Seen at the End of the Viking Mission, *J. Geophys. Res.*, *84*, B14, doi: 10.1029/JB084iB14p08487
- Snyder, S.J., P.E. Hintze, J.L. McFall, C.R. Buhler, J.S. Clements, C.I. Calle (2008) Triboelectric Charging of Dust and Its Relation to Organic Degradation on Mars, *Proc. ESA Annual Meeting on Electrostatics 2008*, Paper F2
- Stanzel, C., M. Pätzold, D.A. Williams, P.L. Whelley, R. Greeley, G. Neukum, HRSC Co-Investigator Team (2008) Dust devil speeds, directions of motion and general characteristics observed by the Mars Express High Resolution Stereo Camera, *Icarus*, *197*, doi: 10.1016/j.icarus.2008.04.017
- Stoy, R.D. (1995) Force on two touching dielectric spheres in parallel field, *Journal of Electrostatics*, *35*, 4, doi:10.1016/0304-3886(95)00003-S
- Strausberg, M.J., H. Wang, M.I. Richardson, S.P. Ewald, A.D. Toigo (2005) Observations of the initiation and evolution of the 2001 Mars global dust storm, *J. Geophys. Res.*, *110*, E02006, doi: 10.1029/2004JE002361
- Sullivan, R., R. Greeley, G. Wilson, P. Smith, C. Cooper (1996) Imager for the Mars Pathfinder Windsock Experiment, *27th Lunar and Planetary Science Conference*, abstract 1289
- Sullivan, R., R. Greeley, M. Kraft, G. Wilson, M. Golombek, K. Herkenhoff, J. Murphy, P. Smith (2000) Results of the Imager for Mars Pathfinder windsock experiment, *J. Geophys. Res.*, *105*, doi: 10.1029/1999JE001234

Sullivan, R. et al. (2008) Wind-driven particle mobility on Mars: Insights from Mars Exploration Rover observations at “El Dorado” and surroundings at Gusev Crater, *J. Geophys. Res.*, *113*, E06S07, doi: 10.1029/2008JE003101

Sutton, J.L., C.B. Leovy, J.E. Tillman (1978) Diurnal Variation of the Martian Surface Layer Meteorological Parameters During the First 45 Sols at Two Viking Lander Sites, *J. Atmos. Sci.*, *35*, 12, pp. 2,346 – 2,355

Tamppari, L.K. et al. (2010) Phoenix and MRO coordinated atmospheric measurements, *J. Geophys. Res.*, *115*, E00E17, doi: 10.1029/2009JE003415

Taylor, P.A., D.C. Catling, M. Daly, C.S. Dickinson, H.P. Gunnlaugsson, A.-M. Harri, C.F. Lange (2008) Temperature, pressure, and wind instrumentation in the Phoenix meteorological package, *J. Geophys. Res.*, *113*, E00A10, doi: 10.1029/2007JE003015

Taylor, P.A. et al. (2010) On pressure measurement and seasonal pressure variations during the Phoenix mission, *J. Geophys. Res.*, *115*, E00E15, doi: 10.1029/2009JE003422

Tillman, J. E., L. Landberg, S. E. Larsen (1994) The boundary layer of Mars: Fluxes, stability, turbulent spectra, and growth of the mixed layer, *J. Atmos. Sci.*, *51*, 12, doi: 10.1175/1520-0469

Thomas, P. and P.J. Gierasch (1985) Dust Devils on Mars, *Science*, *230*, 4722, doi: 10.1126/science.230.4722.175

Thomas, P. and J. Veverka (1979) Seasonal and Secular Variation of Wind Streaks on Mars: An Analysis of Mariner 9 and Viking Data, *J. Geophys. Res.*, *84*, B14, doi: 10.1029/JB084iB14p08131

Thomas, N., C.J. Hasen, G. Portyankina, P.S. Russell (2010) HiRISE observations of gas sublimation-driven activity in Mars’ southern polar regions: II. Surficial deposits and their origins, *Icarus*, *205*, doi: 10.1016/j.icarus.2009.05.030

Tomasko, M.G., L.R. Doose, M. Lemmon, P.H. Smith, E. Wegryn (1999) Properties of dust in the Martian atmosphere from the imager on Mars Pathfinder, *J. Geophys. Res.*, *104*, E4, doi: 10.1029/1998JE900016

Tsoar, H., R. Greeley, A.R. Peterfreund (1979) Mars: The North Polar sand sea and related wind patterns, *J. Geophys. Res.*, *84*, B14, doi: 10.1029/JB084iB14p08167

Ward, A.W. (1979) Yardangs on Mars: Evidence of Recent Wind Erosion, *J. Geophys. Res.*, *84*, B14, doi: 10.1029/JB084iB14p08147

Ward, A.W. and K.B. Doyle (1983) Speculation on Martian north polar wind circulation and the resultant orientations of polar sand dunes, *Icarus*, *55*, doi: 10.1016/0019-1035(83)90112-4

Whiteway, J., M. Daly, A. Carswell, T. Duck, C. Dickinson, L. Komguem, C. Cook (2008) Lidar on the Phoenix mission to Mars, *J. Geophys. Res.*, *113*, E00A08, doi: 10.1029/2007JE003002

Whiteway, J.M. (2009) Mars Water-Ice Clouds and Precipitation, *Science*, *325*, 68, doi: 10.1126/science.1172344

Zent, A.P. M.H. Hecht, D.R. Cobos, G.S. Campbell, C.S. Campbell, G. Cardell, M.C. Foote, S.E. Wood, M. Mehta (2009) Thermal and Electrical Conductivity Probe (TECP) for Phoenix, *J. Geophys. Res.*, *114*, E00A27, doi: 10.1029/2007JE003052

Zent, A.P., M.H. Hecht, D.R. Cobos, S.E. Wood, T.L. Hudson, S.M. Milkovich, L.P. DeFlores, M.T. Mellon (2010) Initial results from the thermal and electrical conductivity probe (TECP) on Phoenix, *J. Geophys. Res.*, *115*, E00E14, doi: 10.1029/2009JE003420

Zurek, R. W. (1976), Diurnal tide in the Martian atmosphere, *J. Atmos. Sci.*, *33*, doi: 10.1175/1520-0469

Zurek, R.W. and L.J. Martin (1993) Interannual Variability of Planet-Encircling Dust Storms on Mars, *J. Geophys. Res.*, *98*, E2, doi: 10.1029/92JE02936

A.1 Websites

[Beagle] Homepage for the Beagle 2 lander
<http://www.beagle2.com/index.htm>

[Clipper Controls] Dielectric Constant Values:
<https://www.clippercontrols.com/pages/dielectric-constant-values>

[CSA] Canadian Space Agency webpage on the LIDAR
<http://www.asc-csa.gc.ca/eng/astronomy/phoenix/lidar.asp>

[Dantec] Laser Doppler Anemometry measurement principles
<http://www.dantecdynamics.com/Default.aspx?ID=822>

[EIDP] Telltale End Item Data Package
http://users-phys.au.dk/hpg/EIDP/TT_EIDP.htm

[ESA yardangs] ESA website on yardangs from the Mars Express site:
http://www.esa.int/SPECIALS/Mars_Express/SEM6GV4QWD_0.html

[ESA seasons] ESA website on Martian seasons
<http://sci.esa.int/science-e/www/object/index.cfm?fobjectid=33803>

[Factsheet] Phoenix mission overview
http://phoenix.lpl.arizona.edu/pdf/fact_sheet.pdf

- [Free Dictionary] Entry on the second ionization coefficient
<http://encyclopedia2.thefreedictionary.com/Townsend+second+ionization+coefficient>
- [GRS] Subsurface hydrogen map of the North Pole on Mars from the homepage for the Mars Odyssey Gamma Ray Spectrometer:
<http://grs.lpl.arizona.edu/latestresults.jsp?lrid=21>
- [Mars factsheet] Accumulation of Mars facts from NASA
<http://nssdc.gsfc.nasa.gov/planetary/factsheet/marsfact.html>
- [MECA] Website for the MECA instrument
<http://planetary.chem.tufts.edu/Phoenix/MECA.html>
- [NASA landing sites] Overview of landing sites on Mars from NASA
<http://marsrover.nasa.gov/gallery/landingsites>
- [NASA – missions] Chronological list of Mars missions from NASA
<http://mars.jpl.nasa.gov/missions/log/>
- [NASA Science] Website on the 2001 global dust storm on Mars
http://science.nasa.gov/science-news/science-at-nasa/2001/ast11oct_2/
- [PHX] Phoenix Mars mission homepage
<http://phoenix.lpl.arizona.edu>
- [Telltale Calibration Report] From the Planetary Data System
http://atmos.nmsu.edu/pdsd/archive/data/phx-m-tt-5-wind-vel-dir-v10/phxwnd_0001/DOCUMENT/
- [VIK] NASA's website for the Viking mission
<http://nssdc.gsfc.nasa.gov/planetary/viking.html>
- [Wikipedia – Sandpaper] Entry on sandpaper (used grit sizes)
<http://en.wikipedia.org/wiki/Sandpaper>
- [Wikipedia – Townsend discharge] Entry on Townsend discharge
http://en.wikipedia.org/wiki/Townsend_discharge

Winds at the Phoenix landing site

Holstein-Rathlou, C., H.P. Gunnlaugsson, J.P. Merrison, K.M. Bean,
B.A. Cantor, J.A. Davis, R. Davy, N.B. Drake, M.D. Ellehoj, W. Goetz,
S.F. Hviid, C.F. Lange, S.E. Larsen, M.T. Lemmon, M.B. Madsen, M. Malin,
J.E. Moores, P. Nørnberg, P. Smith, L.K. Tamppari, P.A. Taylor

J. Geophys. Res., 115, E00E18, 2010
doi: 10.1029/2009JE003411



Winds at the Phoenix landing site

C. Holstein-Rathlou,¹ H. P. Gunnlaugsson,¹ J. P. Merrison,¹ K. M. Bean,² B. A. Cantor,³ J. A. Davis,⁴ R. Davy,⁵ N. B. Drake,⁶ M. D. Ellehoj,⁷ W. Goetz,⁸ S. F. Hviid,⁸ C. F. Lange,⁴ S. E. Larsen,⁹ M. T. Lemmon,² M. B. Madsen,⁷ M. Malin,³ J. E. Moores,¹⁰ P. Nørnberg,¹ P. Smith,¹⁰ L. K. Tamppari,¹¹ and P. A. Taylor⁵

Received 4 May 2009; revised 19 November 2009; accepted 11 December 2009; published 14 May 2010.

[1] Wind speeds and directions were measured on the Phoenix Lander by a mechanical anemometer, the so-called Telltale wind indicator. Analysis of images of the instrument taken with the onboard imager allowed for evaluation of wind speeds and directions. Daily characteristics of the wind data are highly turbulent behavior during midday due to daytime turbulence with more stable conditions during nighttime. From $L_s \sim 77^\circ$ – 123° winds were generally $\sim 4 \text{ m s}^{-1}$ from the east, with 360° rotation during midday. From $L_s \sim 123^\circ$ – 148° daytime wind speeds increased to an average of 6 – 10 m s^{-1} and were generally from the west. The highest wind speed recorded was 16 m s^{-1} seen on $L_s \sim 147^\circ$. Estimates of the surface roughness height are calculated from the smearing of the Kapton part of the Telltale during image exposure due to a 3 Hz turbulence and nighttime wind variability. These estimates yield $6 \pm 3 \text{ mm}$ and $5 \pm 3 \text{ mm}$, respectively. The Telltale wind data are used to suggest that Heimdal crater is a source of nighttime temperature fluctuations. Deviations between temperatures measured at various heights are explained as being due to winds passing over the Phoenix Lander. Events concerning sample delivery and frost formation are described and discussed. Two different mechanisms of dust lifting affecting the Phoenix site are proposed based on observations made with Mars Color Imager on Mars Reconnaissance Orbiter and the Telltale. The first is related to evaporation of the seasonal CO_2 ice and is observed up to $L_s \sim 95^\circ$. These events are not associated with increased wind speeds. The second mechanism is observed after $L_s \sim 111^\circ$ and is related to the passing of weather systems characterized by condensate clouds in orbital images and higher wind speeds as measured with the Telltale.

Citation: Holstein-Rathlou, C., et al. (2010), Winds at the Phoenix landing site, *J. Geophys. Res.*, *115*, E00E18, doi:10.1029/2009JE003411.

1. Introduction

[2] The NASA Phoenix Mars Lander is the first spacecraft to successfully land in a polar region of Mars (68.22°N , 125.75°W). The mission lasted 152 sols corresponding to $L_s = 76^\circ$ to 148° . The main mission objective was to verify the presence of ice in the subsurface using a suite of instruments [Smith *et al.*, 2009]. This landing site is of meteorological interest as it provides unprecedented observations of the northern polar weather and its interaction with the north pole and the subsurface ice.

[3] The lander carried a suite of instruments to investigate the weather conditions. This included a pressure sensor on the lander deck, three thermocouples on a meteorological (MET) mast [Taylor *et al.*, 2008], a lidar [Whiteway *et al.*, 2008] and an imaging system, the Surface Stereo Imager (SSI) with capabilities to perform various atmospheric observations [Lemmon *et al.*, 2008].

[4] Additionally, it was possible to perform coordinated observations with orbiting spacecraft instruments [Tamppari *et al.*, 2010]. This included observations from the Mars Color Imager (MARCI) [Malin *et al.*, 2001] onboard the Mars

¹Department of Physics and Astronomy, Aarhus University, Aarhus C, Denmark.

²Department of Atmospheric Sciences, Texas A&M University, College Station, Texas, USA.

³Malin Space Science Systems, Inc., San Diego, California, USA.

⁴Department of Mechanical Engineering, University of Alberta, Edmonton, Alberta, Canada.

⁵Centre for Research in Earth and Space Science, York University, Toronto, Ontario, Canada.

⁶D. E. Shaw Research, New York, New York, USA.

⁷Niels Bohr Institute, University of Copenhagen, Copenhagen, Denmark.

⁸Max Planck Institute for Solar System Research, Katlenburg-Lindau, Germany.

⁹Wind Energy Department, Risoe National Laboratory, Technical University of Denmark, Roskilde, Denmark.

¹⁰Lunar and Planetary Laboratory, University of Arizona, Tucson, Arizona, USA.

¹¹Jet Propulsion Laboratory, California Institute of Technology, Pasadena, California, USA.



Figure 1. Color images of the Telltale taken between 0800 and 1100 local mean solar time (LMST). The sol numbers are specified in the frame and correspond (in ascending order) to $L_s \sim 99^\circ, 110^\circ, 119^\circ, 131^\circ, 135^\circ, 142^\circ$. The wind speeds and directions for each image are $2.8(5) \text{ m s}^{-1}$ from northeast, $3.2(4) \text{ m s}^{-1}$ from north, $6.8(5) \text{ m s}^{-1}$ from ENE, $6.6(5) \text{ m s}^{-1}$ from SSE, $4.2(4) \text{ m s}^{-1}$ from southwest and $5.2(4) \text{ m s}^{-1}$ from southwest, respectively.

Reconnaissance Orbiter. MARCI produces color images of the whole north polar region, at 1500 local time [Malin et al., 2008]. This enables using information from a local weather station (the Phoenix Lander) in a global context.

[5] Early in 2005, wind measurement instruments on the Phoenix Lander had been descoped for various reasons [Gunnlaugsson et al., 2008; Taylor et al., 2008]. It was, however, noted by the science team that even simple wind measurements would greatly enhance the scientific value of other meteorological instrumentation. For this reason, the so-called Telltale wind indicator [Gunnlaugsson et al., 2008] was added to the payload. The Telltale wind indicator is a mechanical anemometer (see Figure 1) with a total height of roughly 7 cm. It consists of a lightweight Kapton cylinder suspended by Kevlar fibers designed to be deflected under the action of wind. Imaging of the Telltale deflection by the Surface Stereo Imager (SSI) [Lemmon et al., 2008] allowed the wind speed and direction to be quantified. As seen in Figure 2 the SSI and the Telltale are roughly at the same height. A mirror was mounted below the Kapton part of the Telltale to allow for deflections in the line of sight of the SSI to be determined. The Telltale was imaged in series of 3 to 100 images with intervals down to 50 s resulting in an intermittent data set. However, with more than 7500 images over 150 sols, a good degree of diurnal coverage was obtained.

[6] Only three previous Mars landers have measured wind speeds and directions, all in the equatorial regions of Mars. The Viking landers recorded daily wind speeds up to 7 m s^{-1} , with a maximum of 9.5 m s^{-1} [Hess et al., 1977]. Wind speeds were highest in the morning, when the pressure gradient was largest. Wind directions generally rotated 360° daily, counter-clockwise and clockwise, respectively, for the Viking Lander 1 and Viking Lander 2 sites. Mars Pathfinder measured clockwise rotating wind directions [Schofield et al., 1997]. Wind speeds were measured, but await calibrations. The wind speeds from Mars Pathfinder are estimated to be between 5 and 10 m s^{-1} , which correlate well with the sparse results from the windsock experiment on Mars Pathfinder [Sullivan et al., 2000]. Knowledge of the previously measured wind speeds on Mars impacted the design of the Telltale ensuring

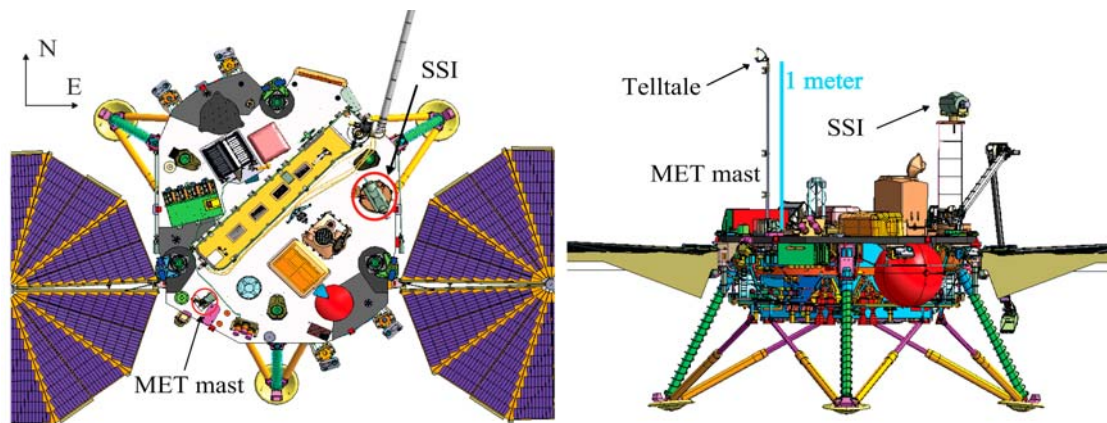


Figure 2. Views of the Mars Phoenix Lander from (left) above and (right) the south. For size considerations, a 1 m line is indicated. The height from the lander deck to the surface is approximately 1 m; thus, the Telltale measures winds at 2 m height above the surface.

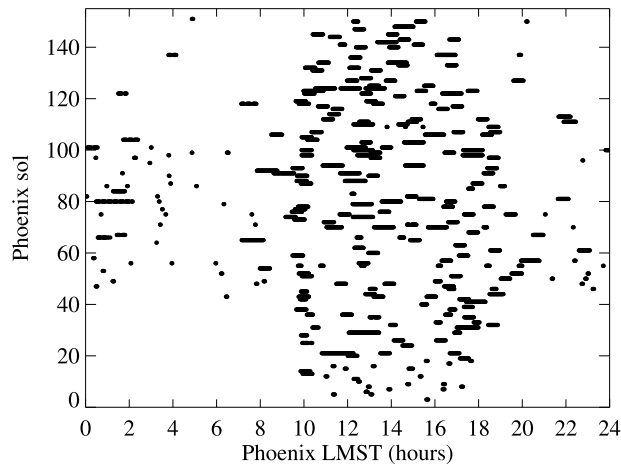


Figure 3. Overview of all Telltale data acquired during the Phoenix mission with time of day plotted against sol number. The nighttime measurements are much less frequent than daytime and are mainly constrained to the interval between sols 40 and 110 ($L_s \sim 95^\circ$ – 128°).

that it would withstand and be sensitive to the range of expected wind speeds at the Phoenix landing site.

2. Telltale Data Collection

[7] Wind data were acquired regularly throughout the Phoenix mission with the bulk of the data obtained in the daytime (0700–1900 local mean solar time (LMST)) operational period of the lander (see Figure 3). Until approximately sol 90 ($L_s \sim 118^\circ$) the Sun never set, thus making nighttime imaging of the Telltale possible. By the end of the mission the Sun rose at 0300 LMST, set at 1950 LMST and dipped 8.9 degrees below the horizon, leaving enough scattered light for the SSI to image the Telltale. The nighttime Telltale images were regular from sol 43 to sol 104 ($L_s \sim 96^\circ$ – 125°). For the remainder of the mission nighttime imaging was very sporadic due to power limitations on the operation of the spacecraft caused by the dwindling amount of sunlight available for recharging the batteries. Despite these nighttime limitations, the diurnal cycle was quantified quite accurately due to the very calm nature of the nighttime winds.

[8] The Telltale was imaged using the 445 nm diopter filter in the right eye of the SSI. This gives excellent contrast in images as the yellow Kapton tube reflects very little light in this wavelength and appears black with the sky as background. Furthermore, it allowed for the longest exposure times, longer than the period of the unperturbed Telltale resonance oscillation at 3 Hz under Martian conditions [Gunnlaugsson *et al.*, 2008]. Contrast problems were only encountered in the afternoon when the sun was closest to the viewing direction of the Telltale.

[9] In the beginning of the mission, sequences consisting of 20 consecutive images with a time interval of just over 1 min were often obtained. By sol 19 ($L_s \sim 85^\circ$) the pointing of the SSI to the Telltale had become sufficiently accurate allowing the images to be reduced to a subframe in order to minimize data volume (see Figure 4). After sol 28 ($L_s \sim 89^\circ$), the SSI Telltale imaging procedure was optimized and images were taken with time intervals of 50–55 s. As a result, acquisition

of 32 images lasted about 28 min. This became the standard for Telltale imaging after sol 35 ($L_s \sim 92^\circ$). From sol 60 ($L_s \sim 104^\circ$) an extra image taken with the 753 nm diopter filter was added to some, and after sol 78 ($L_s \sim 112^\circ$) to all image sequences to allow for more detailed examination and monitoring of dust accumulation on the mirror. An actual dust monitoring image sequence was run about every 20 sols from sol 70 ($L_s \sim 108^\circ$) and consisted of 6 images using the 672 nm stereo pair, 445 nm diopter, 604 nm and 533 nm filters. This set of filters allows for differentiation between dust and ice particles and can be used to obtain color images of the Telltale as seen in Figure 1.

3. Data Analysis

3.1. Image Analysis

[10] Each image was analyzed with respect to the image coordinates of the reference points shown schematically in Figure 4. First, the position of the orientation marker was determined by making use of the holes in it as seen through the mirror image. Then the position of the so-called suspension point (S) was found. Finally, the position of the Kapton tube and its mirror image was determined by superimposing an outline image of the Kapton tube. This information was used to determine the shift of the Kapton tube relative to the symmetry line extending from the suspension point (see “S” in Figure 4) to the center of the mirror (x_{TT} , y_{TT}). x_{TT} is the shift perpendicular to the line of sight from the SSI and y_{TT} is the shift along the line of sight.

3.2. Extraction of Wind Data

[11] The deflection of the Kapton tube of the Telltale as a function of wind speed was carefully calibrated before launch [Gunnlaugsson *et al.*, 2008]. The methods applied made use

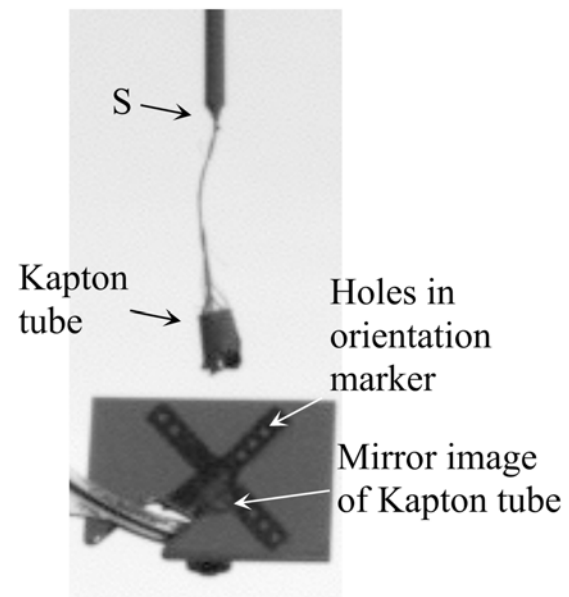


Figure 4. A typical Telltale image after subframing was introduced from sol 19 ($L_s \sim 85^\circ$) and onward. The reference points used for the image analysis throughout the mission are indicated.

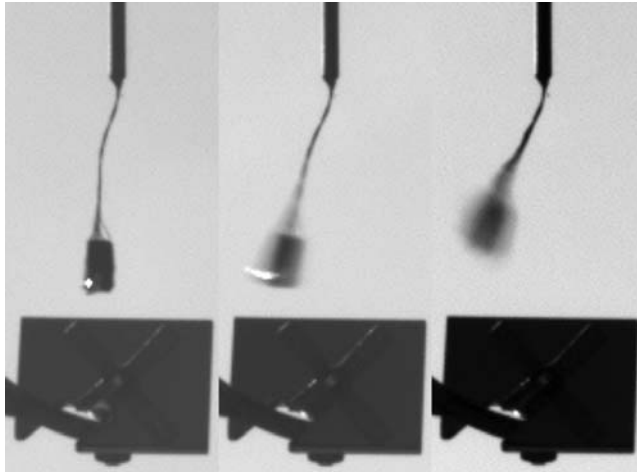


Figure 5. Telltale images from sol 147 ($L_s \sim 146^\circ$) displaying three stages of blurring from (left to right) calm to very blurry. The wind speed and directions are, from left to right, $5.6(5) \text{ m s}^{-1}$ from WNW, $9.4(6) \text{ m s}^{-1}$ from WNW, and $13.3(8) \text{ m s}^{-1}$ from west.

of various types of calibration data [Gunnlaugsson *et al.*, 2008], the most important of which was wind deflection measured in the Aarhus wind tunnel facilities [Merrison *et al.*, 2008]. The data obtained were used to develop a mathematical model of the Telltale's performance in air at 7–20 mbar. This model was then scaled to Martian gravity and atmospheric gas composition. The accuracy of the measured deflection depends on how well the rest position, where the Telltale would reside under no wind conditions, is determined. This depends on the tilt of the lander, whether the mast is perfectly perpendicular to the lander deck and potential damage and rearrangement of Kevlar fibers during launch and landing. Small inaccuracies in determining the vector of gravity relative to the Telltale have significant impact on the exact shift of the Kapton part of the Telltale especially at low wind speeds. Instead of making use of the preflight data to determine this rest position, it was decided to make use of the so-called blurring of the Kapton part of the Telltale as described below.

3.3. Calibration of the Telltale on the Surface of Mars

[12] In order to determine the true rest position of the Telltale on Mars the amount of blur in the image of the Kapton tube was used. The blurring, or smearing, of the Kapton tube in the images (see Figure 5) is caused by its movement during image exposure, making it appear larger than it actually is. Part of this blurring is caused by real wind changes during exposure, but some is also due to the 3 Hz resonance of the Telltale on Mars which can increase the observed oscillation amplitudes by a factor of up to 6.5 in the frequency range 2.5–3.5 Hz [Gunnlaugsson *et al.*, 2008]. Even the slightest wind contains fluctuations, which depend on the wind speed. The blurring is proportional to these wind speed fluctuations, so the position with the smallest blurring should correspond to the rest position of the Kapton part of the Telltale. Besides wind speed and wind direction the analysis will also provide a value for the surface roughness height.

3.3.1. Theoretical Considerations

[13] The strength of the 3 Hz resonance can be estimated using generic power spectra of the surface layer turbulence [Kaimal *et al.*, 1972]. Here the power spectrum $fS(n)$ can be found from

$$\frac{fS(n)}{u_*^2} = \frac{105n}{(1 + 33n)^{5/3}} \quad (1)$$

where n is the normalized frequency, $n = fz/v$, z is the measurement height (2 m), v the wind speed, and u_* the friction velocity:

$$u_* = \frac{\kappa v}{\ln(z/z_0)} \quad (2)$$

where κ is von Karman's constant usually taken as 0.4 and z_0 is the surface roughness height. The square root of the integration of the power spectrum in the relevant frequency range gives the standard deviation of wind fluctuation:

$$\sigma_{res}(v) = \sqrt{\int_{2.5}^{3.5} S(f) df} \quad (3)$$

where the subscript "res" refers to integration around the resonance. Within the range of wind speeds used for the blurring analysis ($v = 2\text{--}15 \text{ m s}^{-1}$) and using surface roughness heights of $z_0 = 1\text{--}100 \text{ mm}$, a reasonable approximation yields

$$\sigma_{res}(v) = \frac{0.06915 \cdot v^{4/3}}{\ln(z/z_0)} \quad (4)$$

[14] The most important result from these considerations is that one should expect σ/v to follow $v^{1/3}$ dependence. The description above is valid for winds perpendicular to the line of sight of the Telltale. However, the turbulence also has a perpendicular component of similar magnitude, making this description independent of the angle relative to the line of sight.

3.3.2. Data Analysis

[15] The blurring was found by estimating the width of the Kapton part of the Telltale in radiometric calibrated images. In many cases, this was not possible due to reflections and/or noise in underexposed images. Certain angles give rise to higher turbulence due to airflow coming from the frame of the Telltale (the gallows) and mirror (see below) and were avoided in the analysis. Only daytime data (9–15 LMST) were used for the analysis.

[16] From each image used for the analysis (labeled I), the shift of the Kapton part of the Telltale ($x_{TT,I}$, $y_{TT,I}$) was determined together with the blurring b_I . The rest position (x_0 , y_0) was determined as the solution of

$$\text{Min}_{x_0, y_0, C} \left(b_I - C \left((x_{TT,I} - x_0)^2 + (y_{TT,I} - y_0)^2 \right)^{7/12} \right) \quad (5)$$

where C is a constant and the exponent 7/12 originates from the shift being roughly proportional to v^2 (cf. Figure 5 of Gunnlaugsson *et al.* [2008]) and appropriate change of

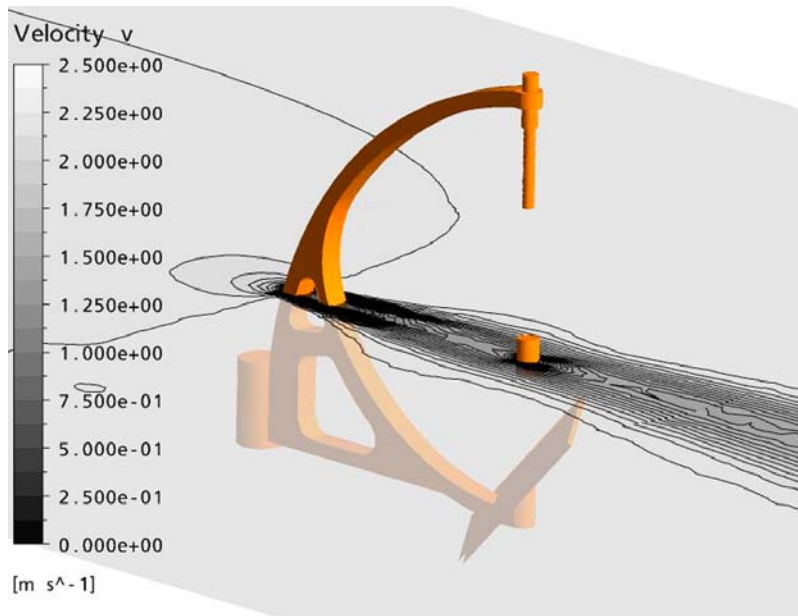


Figure 6. Velocity contours showing the effect of the gallows on the wind speeds measured by the Kapton tube. Wind velocities are in units of m s^{-1} with the lowest wind speeds seen in the wake of the gallows.

variables. This gave $x_0 = 0.55(7)$ mm and $y_0 = 3.30(7)$ mm. This solution is 2 mm from preflight estimate which could be caused by a slight tilt of the mast toward the right in the image frame. Change in gravity from Earth to Mars could also be responsible for a different bending of the Kevlar fibers, thus changing the rest position of the Kapton tube. From the optimization we find the solution $\Delta v = 0.0119 \cdot v^{4/3}$ where Δv corresponds to the standard deviation. Using equation (4) and taking the strength of the resonance into account we find $z_0 = 6(3)$ mm.

3.4. Potential Sources of Error

3.4.1. Structures Around the Kapton Tube

[17] If the Kapton tube is in the wake of another solid object, it may not see the true wind velocity. Several sources of wakes are identified: the frame of the Telltale (the gallows), the mirror mounted on the Telltale, and the SSI camera. To study the effects of these wakes, computational fluid dynamics (CFD) simulations were performed, solving the flow around the Telltale under Martian conditions [Davis and Lange, 2009b], as well as wind tunnel experiments using the Aarhus wind tunnel facilities [Merrison et al., 2008]. In the wind tunnel experiments, the wind speed of particles was measured using Laser Doppler Anemometer in the direction of the flow at 11 mbar of air which is closer to the fluid density of the atmosphere on Mars than 7 mbar of air.

[18] Simulations of the Kapton tube orientated exactly in the wake of the Telltale's frame (c.f. Figure 6) show a reduction of up to 60% in the perceived wind velocity of 2.5 m s^{-1} . Wind tunnel measurements show a maximum reduction of 15% at 2 m s^{-1} over a narrow angular interval ($\pm 20^\circ$) and a larger deviation at lower wind speeds (35% reduction at 0.4 m s^{-1} over $\pm 40^\circ$). Overestimation in CFD calculations may be due to lack of turbulence in the incoming airflow. The low Reynolds number, of about 10, of the flow in CFD calculations, suggests the wake would be steady [Frisch, 1995] in the case of a steady wind.

[19] Results of CFD calculations related to the Telltale mirror are shown in Figures 7 and 8. First, it was noted that the drag force enhancement is greatest when the fluid is flowing over the back of the mirror (as shown in Figure 7), resulting in a perceived increase in wind speed of 20% for a wind velocity of 2.5 m s^{-1} . Wind tunnel experiments at 2 m s^{-1} suggest 10%

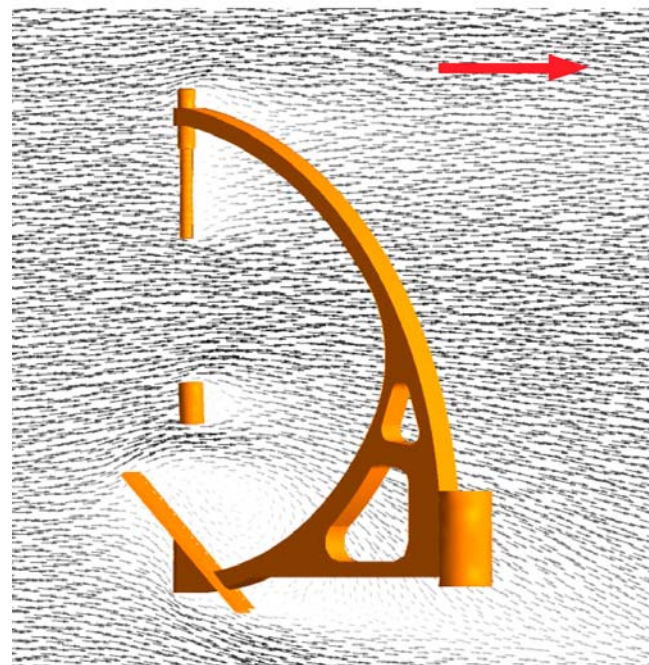


Figure 7. Velocity vector plots obtained from Computational Fluid Dynamic (CFD) calculations showing the effect of the mirror on the Kapton tube for a wind speed of $v = 2.5 \text{ m s}^{-1}$ flowing over the back side of the mirror. Wind is to the right.

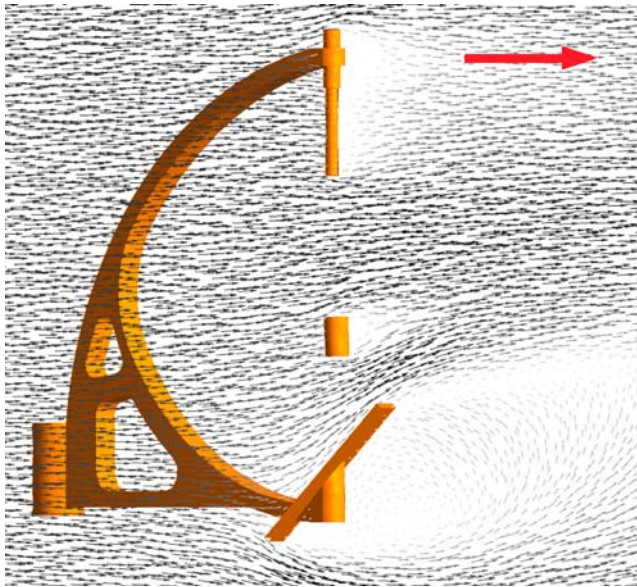


Figure 8. Velocity vector plots obtained from CFD calculations showing the effect of the mirror on the Kapton tube for a wind speed of $v = 2.5 \text{ m s}^{-1}$ flowing over the front side of the mirror. Wind is to the right.

increase in the wind speed. Small lift forces caused by the air deflecting from the mirror can contribute to this increase. The lift forces are strongest, when the wind comes from the front of the mirror, as seen in Figure 8.

[20] The wake of the SSI camera is responsible for another source of momentum deficit, i.e., velocity difference between the Telltale and the surroundings. Simulations of a flow over the Phoenix Lander with a wind direction of 45° (NE), seen in Figure 9, show a weaker effect from this wake, producing a flow reduction of only 5% near the Telltale at the top of the MET mast. Here, due to the larger scales of the lander, the actual Telltale was not simulated.

[21] Momentum error can also stem from the heating of the lander itself, which produces thermal plumes that may, under quiescent conditions, result in a vertically dominant flow. In CFD simulations of such cases the mirror was found to significantly shield the Telltale from these plumes, reducing the vertical velocity to 0.1 times the plumes' vertical velocity component [Davis and Lange, 2009a].

[22] Although these estimated wake effects seem significant, they are highly dependent on the wind direction, requiring almost perfect flow alignment for the full effect. Natural variability in the wind direction results in a significantly reduced effective impact in the measurements. Wind tunnel flow experiments of the wake effect of the galleys showed less deviation than CFD calculations, and the effect was reduced with increased wind speeds. These experimental flow cases, with turbulent velocity fluctuations of 5% on average, demonstrate how the actual effect of wakes is smaller than the extreme cases from the simulations.

[23] We have chosen not to alter the numbers found from the data analysis, but for careful interpretation of the data, one has to assume up to 20% underestimation of wind speeds from meteorological direction of 106° (galleys) and an overestimation of up to 10% at meteorological direction of 236° (mirror).

3.4.2. Dust Accumulation

[24] As the mission progressed, dust accumulation on the Kevlar fibers became evident (see Figure 10). On sol 3 ($L_s \sim 78^\circ$) only minor dust accumulation on the Kevlar fibers can be seen from the contrast of the fibers. This contrast increases at steady rate until sol 70 ($L_s \sim 108^\circ$). On later sols, the fibers appear thinner, indicating that they have been partially cleared of dust. The first major dust devil days, were at sols 77–78 ($L_s \sim 112^\circ$) and 93–95 ($L_s \sim 120^\circ$) [Ellehoj et al., 2010], suggesting that dust devils have cleaned dust off the fibers.

[25] Laboratory tests suggest an upper limit of the dust accumulation of the order of 0.5 mg. As this mass is accumulated on the upper part of the movable component of the Telltale, and is small compared to the total weight of the

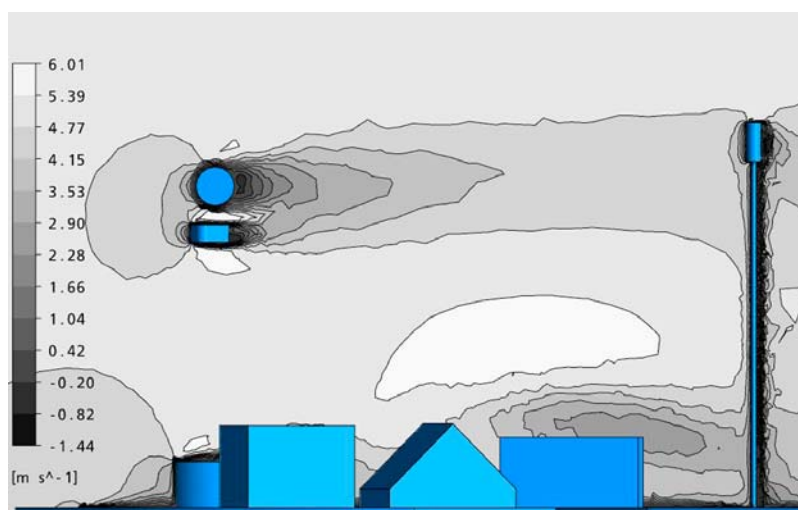


Figure 9. Schematic drawing of the Phoenix Lander with velocity contours showing the effect of the SSI Camera (circle on the left) on the wind speeds measured at the top of the MET mast (pole on the right). The Telltale is too small to be included in the lander model. The wind is to the right and velocities are in units of m s^{-1} .

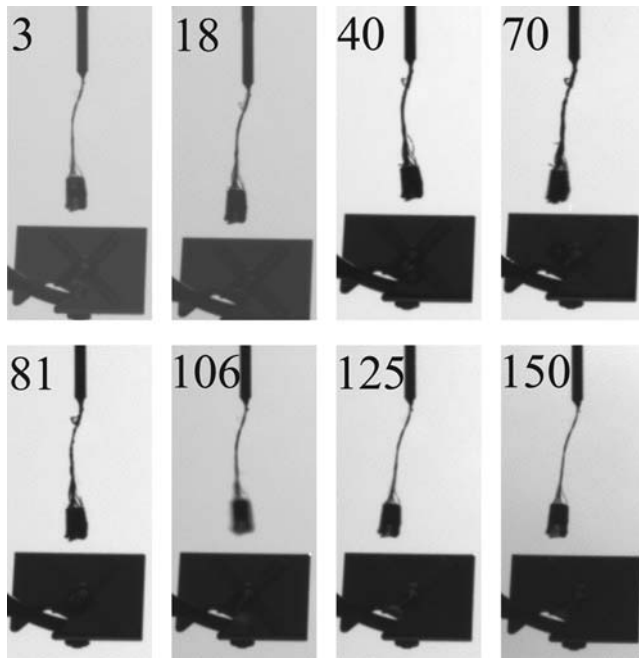


Figure 10. Images of the Telltale taken around 1535 LMST on the sols indicated. Up to sol 81 ($L_s \sim 114^\circ$) the contrast between the fibers and the background increases indicating dust accumulation on the fibers. Thereafter less contrast suggests removal of dust. The corresponding values of L_s , wind speed, and direction are as follows: 78° , $4.5(5) \text{ m s}^{-1}$ from west; 85° , $5.2(5) \text{ m s}^{-1}$ from northwest; 95° , $2.3(5) \text{ m s}^{-1}$ from southwest; 109° , $7.4(5) \text{ m s}^{-1}$ from north; 114° , $3.9(5) \text{ m s}^{-1}$ from north; 126° , $5.0(5) \text{ m s}^{-1}$ from WSW; 135° , $7.7(5) \text{ m s}^{-1}$ from NNW; 148° , $7.1(5) \text{ m s}^{-1}$ from northwest.

active part of the instrument ($\sim 15 \text{ mg}$) its potential effect has been neglected here.

[26] Dust also accumulated on the Telltale mirror (see Figure 1), preferentially at the bottom and right sides. This may have given rise to small errors in the position of the bottommost holes in the orientation marker. This effect is worst in the late afternoon where contrast problems affect the Telltale mirror. The error is below one pixel and has a minimum effect on the final wind speed and direction due to the manner of the data analysis. As with the fibers, the mirror seems to be cleaned after sol 80 ($L_s \sim 113^\circ$) (see Figure 1).

4. Meteorological Results

[27] After data reduction, the data from each image is presented as wind speed (v), given in units of m s^{-1} , and direction (θ), given according to standard meteorological convention with 0° being winds from the north, 90° coming from the east, 180° coming from the south, and 270° coming from the west.

4.1. Daily Trends in the Wind Data

[28] Figure 11 shows representative 1 h data from the Telltale during midday and nighttime. During midday, daytime turbulence significantly modifies the average conditions both for temperature and winds as seen in Figures 11a–11c. The time scale of these features is on the order of minutes, so

to obtain useful averages, one must use as long sampling periods as possible. Referring to Figure 11a it is evident that a 5 image exposure could result in average wind speeds in the range of $2\text{--}6 \text{ m s}^{-1}$ depending on the momentary conditions.

[29] Sequences of 32 images were regular from sol 35 ($L_s \sim 92^\circ$) resulting in an adequate number of sequences throughout the mission from which to obtain the statistics as a function of local time as shown in Figure 12. During midday relative standard deviations of 15–40% are observed due to daytime turbulence. These statistics were not seen to change during the mission. From 18 to 06 LMST stable conditions are observed with relative standard deviation of $\sim 4\%$, corresponding to the stable nighttime conditions seen in Figures 11d–11f. The nighttime statistics give an independent measure of the surface roughness height. With integration over the relevant frequency range, and using the fact that average wind speeds in this period were $\sim 4.7 \text{ m s}^{-1}$, one finds $z_0 = 5(3) \text{ mm}$, in agreement with the value found from blurring analysis.

4.2. General Trends and Changes in Weather Pattern

[30] To illustrate general trends with mission time, Figure 13 presents the hourly average values and standard deviations for the complete Telltale data set in sections of 30 sols. In the first 60 sols ($L_s \sim 77^\circ$ to 105°), conditions were very repeatable with average wind speeds of about $3\text{--}6 \text{ m s}^{-1}$ and nighttime wind direction generally from east to northeast. During daytime (07–19 LMST) wind directions tend to rotate 360 degrees clockwise. After sol 90 ($L_s \sim 118^\circ$), this repeatable pattern started to change, and winds were observed more commonly from the west with high wind speeds during midday of average 8 m s^{-1} .

4.2.1. Wind Speeds

[31] Figure 14 displays average wind speeds during daytime conditions from Telltale image series with more than 10 images. The first ~ 70 sols reflect the general trend seen in Figure 13 with average daytime wind speeds of $\sim 4 \text{ m s}^{-1}$. From sol 70 to 100 ($L_s \sim 108^\circ\text{--}123^\circ$) there are two periods of increased wind speeds at around sols 77 and 94 ($L_s \sim 112^\circ$ and 120°) which correlate with increased dust devil activity [Ellehoj *et al.*, 2010]. Other related meteorological observations indicate that this increase in atmospheric activity might be the result of weather systems passing over the Phoenix Lander. The issue will be addressed in more detail in the discussion section of this paper. From sol 110 ($L_s \sim 127^\circ$) a steady rise in daytime average wind speeds is observed with a maximum wind speed of $16(1) \text{ m s}^{-1}$ measured on sol 148 ($L_s \sim 147^\circ$).

4.2.2. Wind Directions

[32] Figure 15 shows the average wind directions for all Telltale series containing 10 or more images. Evident in both daytime and nighttime data is the change to westerly wind directions which starts about sol 90 ($L_s \sim 118^\circ$). Large error bars on the average daytime wind directions stem from the daytime turbulence which is largest during the 13–19 LMST time period. Later in the mission a stronger westerly wind component is observed resulting in diminishing error bars. Nighttime wind directional change starts simultaneously with the daytime wind directions.

[33] Another source of wind direction data at the Phoenix site is the Zenith movie data set [Moore *et al.*, 2010]. A Zenith movie is a series of images taken with the SSI pointing

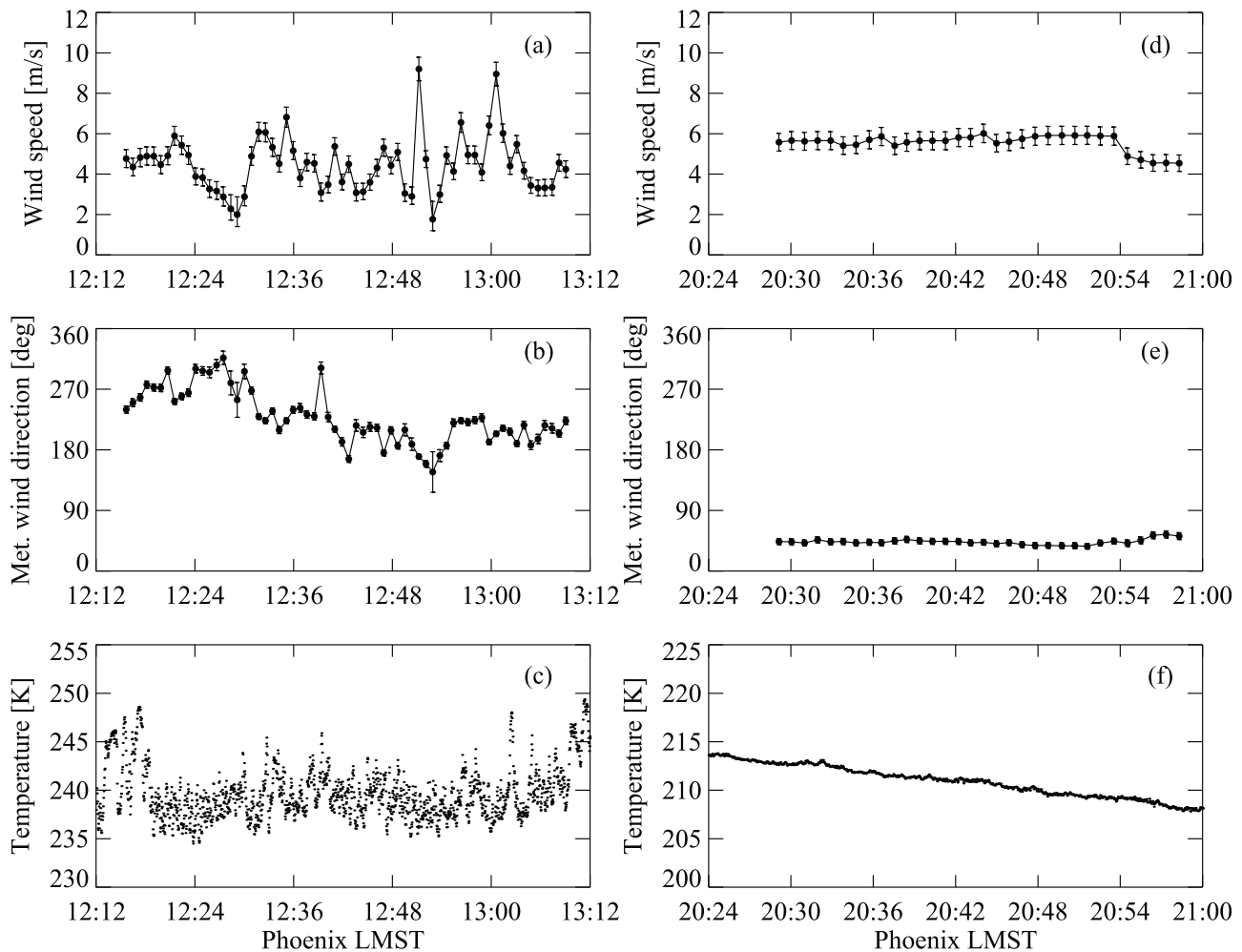


Figure 11. Examples of typical wind data and their corresponding temperature data. (a–c) Unstable mid-day conditions on sol 67 ($L_s \sim 107^\circ$). (d–f) More stable evening conditions on sol 100 ($L_s \sim 123^\circ$).

upward to the zenith point. Wind directions were inferred from the movement of features between the images. The data show the same daily turnaround in wind directions as seen in the Telltale data [Tamppari *et al.*, 2010]. This is unusual since the Zenith movies are most likely seeing winds at several km's height, where slope winds at nighttime should be absent. The Zenith movie wind directions are, however, not seen to change later in the mission as observed with the Telltale wind directions. This could be related to the fact that the features which are present later in the mission move too fast through the image field, making accurate determination of wind direction increasingly difficult [Moores *et al.*, 2010] or due to scarce Zenith movie data in the last part of the mission.

[34] Slope winds do not seem to be an explanation for the diurnal wind direction variations. Local slopes are small, and as winds at several kilometers observed in Zenith movies data set [Moores *et al.*, 2010] follow the same pattern, the boundary layer would have to be unusually thick. Alternatively, atmospheric thermal tides may be invoked to explain these findings [Gierasch and Goody, 1968; Zurek, 1976; Leovy, 1981].

[35] The seasonally changing wind direction is however mirrored in the associated directions of the dust devil observations made at the Phoenix landing site. Dust devils in the

vicinity of the lander were identified as sudden drops in the pressure data [Ellehoj *et al.*, 2010]. Correlating the times of the dust devils with the Telltale observations resulted in 28 instances where it is possible to discern from which direction

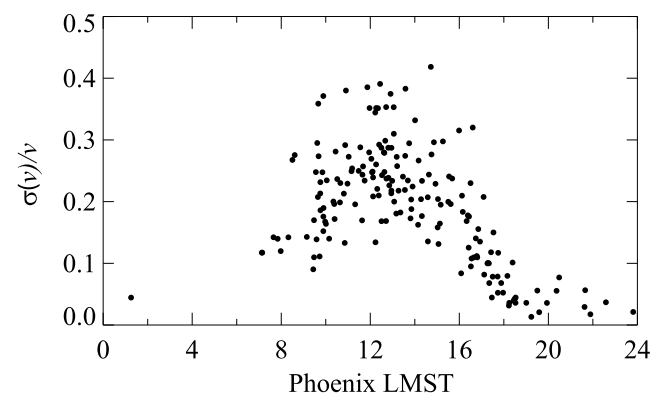


Figure 12. Standard deviation of wind speeds divided by the average wind speed as calculated from 32 image exposures as a function of LMST. The data spans the whole mission. The highly turbulent behavior of the daytime winds is expressed in the midday higher values.

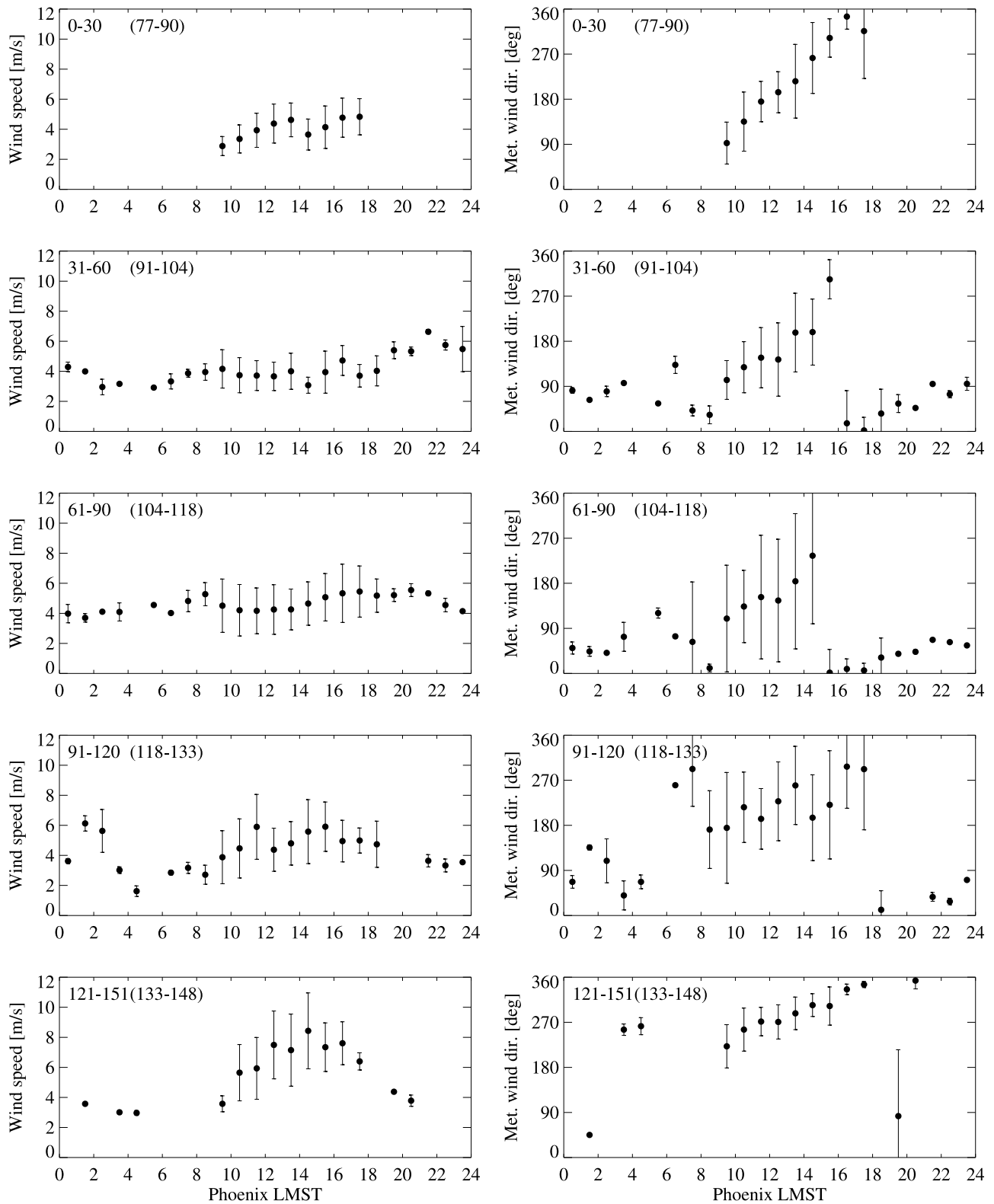


Figure 13. (left) Average wind speeds and (right) wind directions as measured by the Telltale during the Phoenix mission. The calculations were done in 1 h intervals for the sol range indicated (L_s is indicated in parenthesis). Error bars represent the standard deviation in each bin.

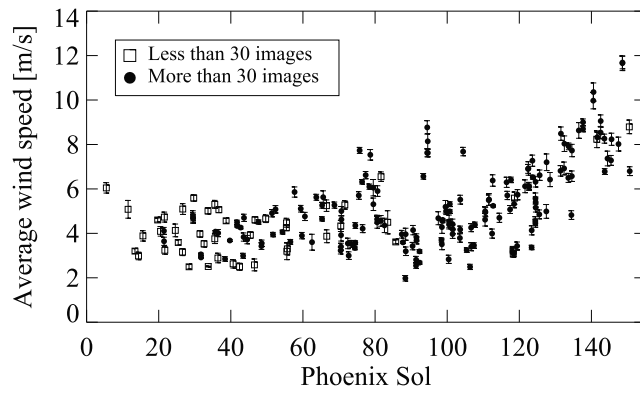


Figure 14. Average wind speeds between 0600 and 1800 LMST as a function of mission time. Open squares mean the value was calculated from an image series with 10 to 30 images; closed circles indicate more than 30 images. Error bars indicate one standard deviation.

the dust devil came from by using the Telltale wind direction just prior to the dust devil passing. Figure 16 shows the wind direction for these 28 dust devil passages. The agreement between the 13–19 LMST data in Figure 15 (left) and the dust devil wind directions is due to the fact that dust devils were mostly observed during midday [Ellehoj *et al.*, 2010].

[36] Dust devil tracks as well as wind streak features as seen from MGS were used by Drake *et al.* [2006] to infer the wind direction in the Phoenix landing latitude before Phoenix landed. The original paper did not include the wind directions for the Phoenix landing site (region D of Arvidson *et al.* [2008]) as this region had been descoped at the time of the study. They are however provided in Figure 17 where the predominant wind direction is seen to be WNW or ESE. Note that there is a directional ambiguity since the surface expression of these winds does not indicate if the winds are blowing, e.g., NW to SE or SE to NW. Wind directions in the latter part of the Phoenix mission (after approximately sol 95 ($L_s \sim 120^\circ$)) correspond well with these very unidirectional

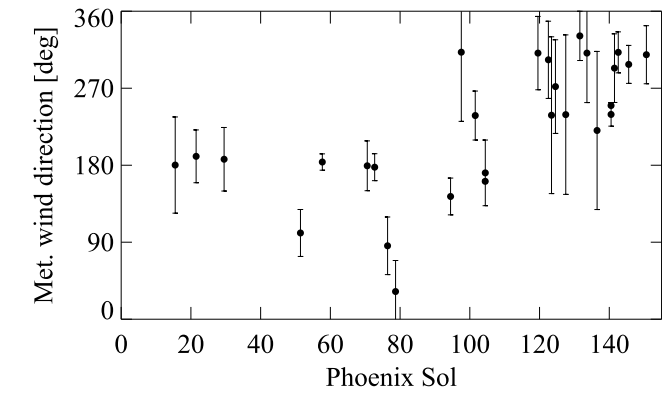
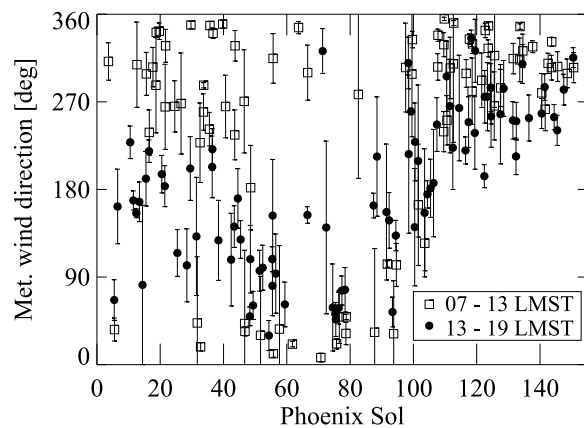


Figure 16. Wind directions obtained from Telltale image series overlapping with dust devil passing as a function of time of mission. Error bars represent one standard deviation.

tracks, indicating that the dust devils most likely came from the WNW direction. The fact that only one direction is observed, contrary to Figure 16, could be due to the fact that these tracks were made at the peak of the dust devil season, which is indicated to be after $L_s \sim 150^\circ$ by dust devil statistics from the Phoenix Lander [Ellehoj *et al.*, 2010]. However, lack of complete seasonal data makes it difficult to reach definite conclusions on this issue.

[37] Wind conditions modeled by Tyler *et al.* [2008] and from the Mars Climate Database [Forget *et al.*, 1999] around the time of landing suggest winds from the east throughout the day.

4.3. Turbulence Parameters

[38] The two independently determined values for the surface roughness heights at the Phoenix landing site agree on a smaller value, 5(3) and 6(3) mm, than previously cited for the Viking Lander 2 and Mars Pathfinder landing sites of 1 and 3 cm, respectively [Tillman *et al.*, 1994; Sullivan *et al.*, 2000]. This is expected since the landing sites of the two Viking landers and Mars Pathfinder are more rock abundant

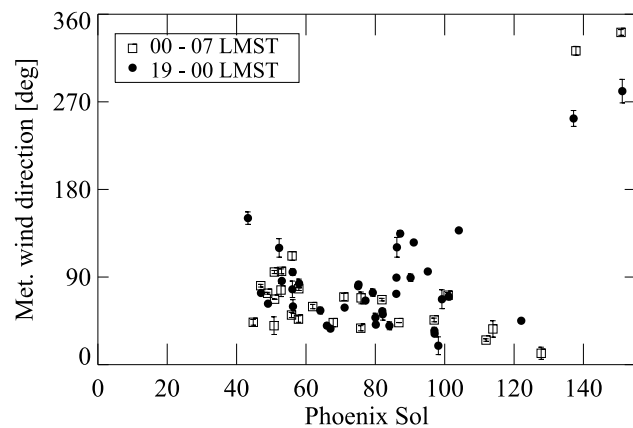


Figure 15. Average wind directions during (left) daytime and (right) nighttime as a function of mission time. In each case, the time period is split into early (open squares) and late periods (filled circles) in order to view differential behavior. Each point represents the average wind direction of a Telltale image series with more than 10 images. Error bars represent one standard deviation.

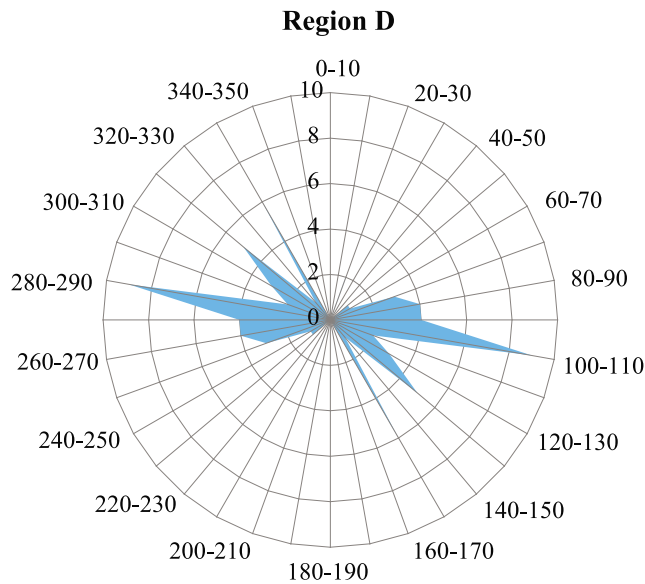


Figure 17. Directions of dust devil tracks and wind streak in the Phoenix landing area, region D, as a function of number of observations (radial axis). The observations are grouped in bins of 10 degrees and all wind directions are meteorological convention. Inferred wind direction may be parallel or anti-parallel to track/streak orientation.

than the Phoenix landing site [Golombek *et al.*, 1997; Heet *et al.*, 2009].

[39] Using a surface roughness height of 6 mm, the highest friction velocities observed at the Phoenix landing site were around 1.1 m s^{-1} . This gives shear stress of 0.02 Pa which should be sufficient to move dust aggregates with diameters of around $150 \text{ }\mu\text{m}$ or above [Merrison *et al.*, 2008]. Imaging by the Optical Microscope indicates that the building blocks for dust aggregates exist at the landing site [Smith *et al.*, 2009]. Until sol 104 ($L_s \sim 125^\circ$) only dustless vortices were observed at the landing site through pressure drops [Ellehoj *et al.*, 2010]. Hereafter dust devils could be observed by the SSI camera [Ellehoj *et al.*, 2010]. The maximum shear stress of 0.02 Pa is far from the shear stress of 0.07 Pa needed to detach sand grains [Merrison *et al.*, 2008]. Thus, the relative flatness of the landing site, resulting in the low surface roughness height, may hamper the formation of dunes in this area, or the formation of dunes takes place at a rate slower than modifications of the surface due to underlying ice.

5. Discussion on Wind Effects

5.1. Nighttime Temperature Fluctuations

[40] Temperatures measured by the Phoenix Lander show a general trend throughout the mission with 10–20 K fluctuations in the daytime and smoother profiles during nighttime. The temperature fluctuations due to daytime turbulence die out in the late afternoon ($\sim 17 \text{ LMST}$) and start again in the early morning ($\sim 06 \text{ LMST}$). However, at around midnight, significant fluctuations are observed. An example is shown in Figure 18 (top). The temperature events repeated almost every night around the same time for the first couple of months. To visualize these fluctuations better, we applied a filter to pick out 1 min fluctuations and then applied a

90 s running average. The results are shown in Figure 18 (bottom).

[41] On sol 113 ($L_s \sim 129^\circ$), Telltale observations were made when the midnight temperature fluctuations started. Figure 19 shows temperature and wind data from sol 113, compared to the same time period on sol 81 ($L_s \sim 114^\circ$), where conditions were more stable. Sols 81 and 113 are among the scarce Telltale observations from this time period.

[42] Although the temperature fluctuations have some of the same characteristics of the midday temperature fluctuations, the Telltale data for sol 113 shows only minor direction changes, and no characteristic daytime turbulence behavior as seen in daytime data (see Figures 11a–11c). Conditions seem only slightly more variable than on sol 81. With turbulence absent, the temperature fluctuations represent instead an air mass that has not been completely homogenized. Based on Telltale data, winds are generally from the east at this time of day (see Figure 15), and it seems possible that this behavior is due to an air mass that has passed over Heimdal crater. Heimdal crater is 10 km across and being only 20 km to the east from the Phoenix Lander it is the only major geographical feature in the vicinity [Smith *et al.*, 2009]. MOLA data shows that Heimdal has slopes reaching 4–7 degrees, far

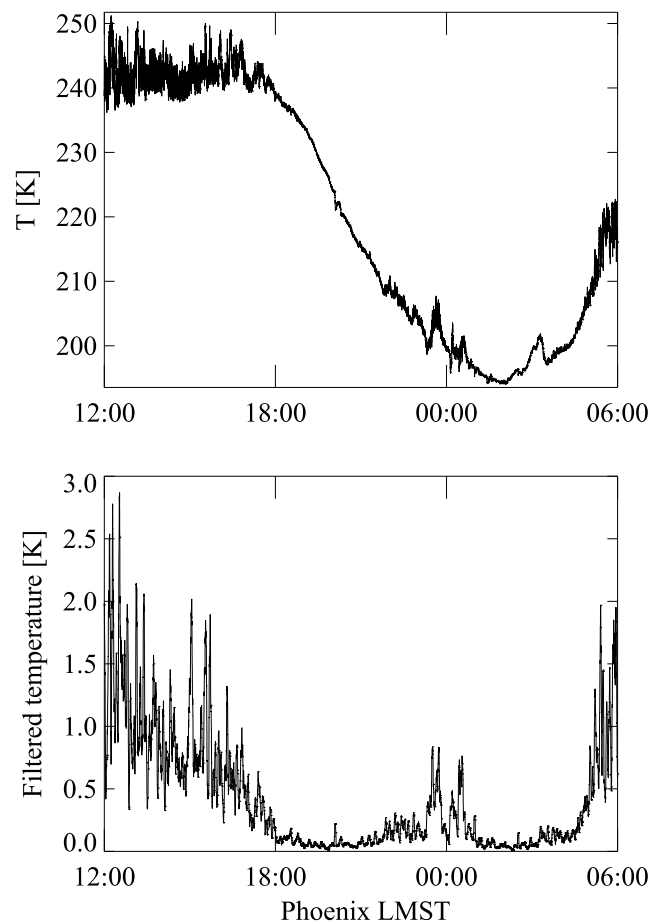


Figure 18. (top) Atmospheric temperature measured at a sampling frequency of 0.5 Hz with the top thermocouple on sols 55/56 ($L_s \sim 101^\circ$ – 102°) from noon to 0600 LMST. (bottom) One minute temperature fluctuations on sol 55/56 from noon to 0600 LMST.

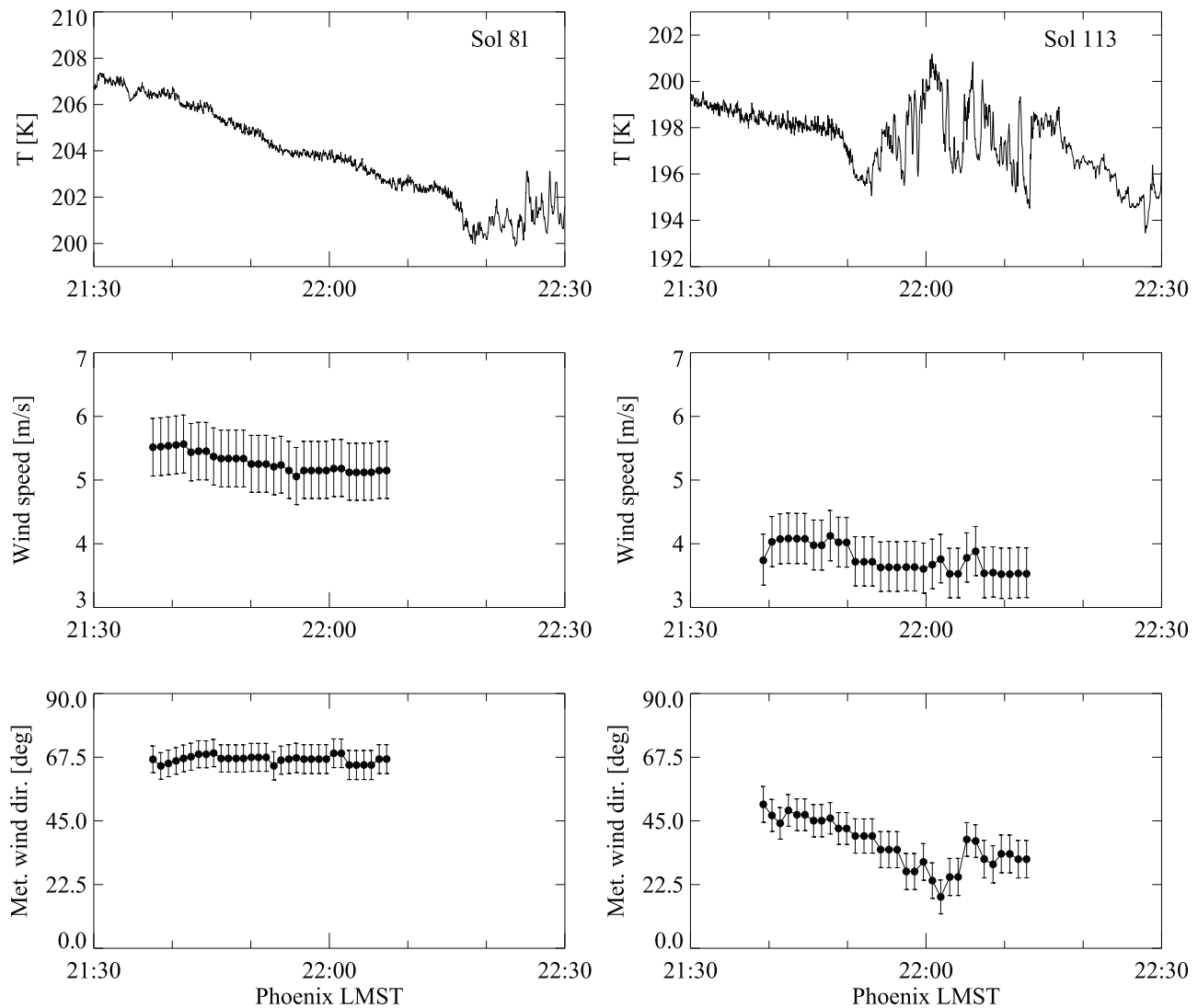


Figure 19. Comparison between (left) sol 81 ($L_s \sim 113^\circ$), which has no temperature disturbance, and (right) sol 113 ($L_s \sim 129^\circ$) with temperature disturbance. The differences are seen in the temperature of the (top) top thermocouple, (middle) wind speeds, and (bottom) wind directions.

exceeding the 1 degree slope of Green Valley, where Phoenix sits, and the 1.4 degrees of the area southeast of Heimdal.

[43] As seen in Figure 15 wind directions change late in the mission and on sol 137 ($L_s \sim 141^\circ$), in particular, winds from the west dominate the early morning and late evening data. Filtered temperature data from sol 137 show the absence of the up to ~ 1 K fluctuations in these data (see Figure 20). Winds do not pass over Heimdal crater indicating that the midnight temperature fluctuations are possibly related to Heimdal crater. More mesoscale modeling is needed to get in-depth information on this phenomenon.

5.2. Directional Temperature Dependency

[44] Air temperatures were measured continuously throughout the Phoenix mission with the three thermocouples positioned on the MET mast [Taylor *et al.*, 2008]. At several times during a typical sol, not counting the midday turbu-

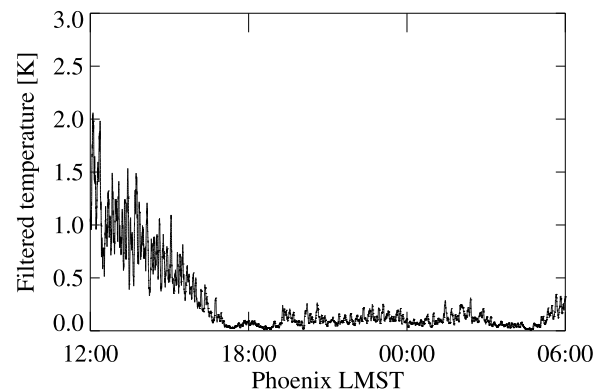


Figure 20. Filtered temperature data from sols 137/138 ($L_s \sim 141^\circ$) where the nighttime temperature fluctuations are absent.

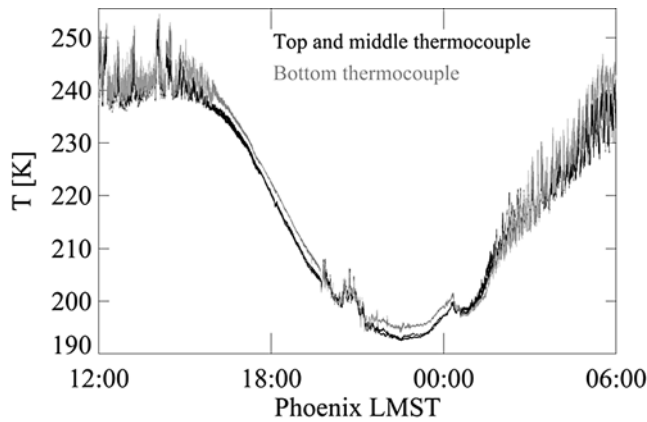


Figure 21. Thermocouple temperatures as a function of time of day from mid sol 66 to mid sol 67 ($L_s \sim 107^\circ$). The temperature measurements from the top and middle thermocouple fall on top of each other and are therefore represented as one combined black line. The gray line indicates the temperatures as measured from the bottom thermocouple.

lence, the bottom thermocouple showed unexpected higher temperatures than the other two as seen in Figure 21.

[45] In order to help explain these temperature differences it has proven useful to investigate if they depend on the wind direction. To further examine this phenomenon the temperature difference between the bottom thermocouple and the average value of the two upper thermocouples, $T_{\text{bottom}} - \langle T_{\text{top}}, T_{\text{middle}} \rangle$ was calculated for every Telltale measurement. The average value was employed because the two upper thermocouples display roughly equal temperatures and to get better statistics. Each temperature difference thus has an associated wind direction. When binning the wind directions in bins of 5 degrees from 0 to 360 degrees, average values and standard deviations of the associated temperature differences could be calculated. Figure 22 shows the resulting plot which displays a clear directional dependency with the greatest

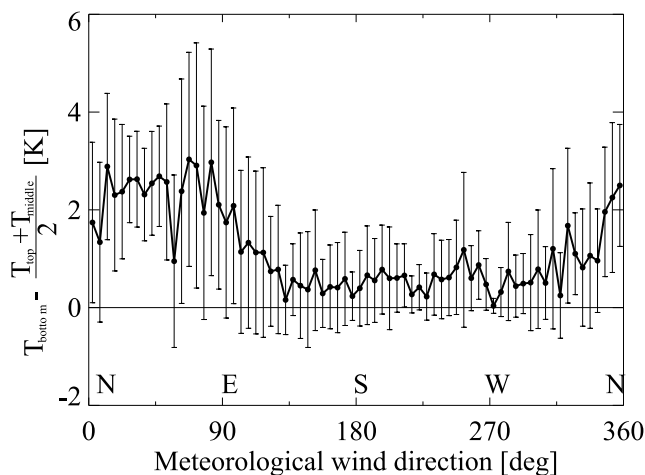


Figure 22. Thermocouple temperature differences with respect to the bottom thermocouple as a function of wind direction. Each point on the line represents the average temperature value calculated for the respective wind direction bin. Error bars represent one standard deviation.

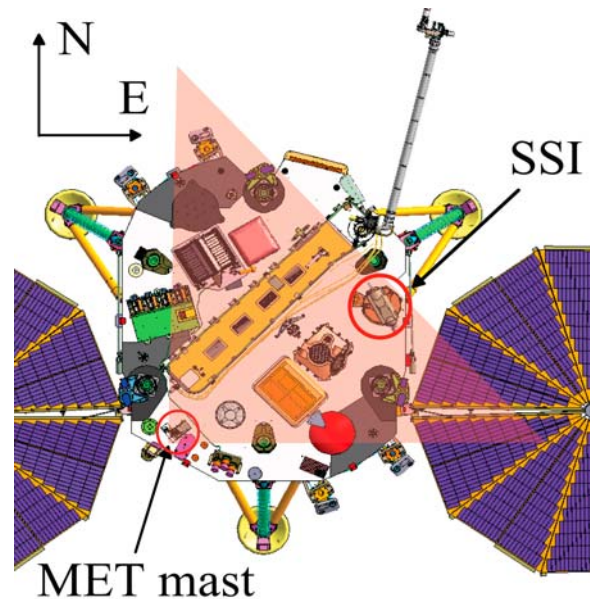


Figure 23. Overview of the Phoenix Lander deck showing the placement of the MET mast in the bottom left corner. The shaded triangle covers the directions across the lander which affected the bottom thermocouple. Underneath this area is located the TEGA instrument, the LIDAR, several communication devices, the SSI, and parts of MECA.

temperature differences being when the wind direction is from north through east.

[46] Correlating these wind directions with an overview of the Phoenix Lander deck (see Figure 23) reveals that the greatest temperature differences occur when the winds reaching the MET mast have passed over the lander deck. Instruments and communication antennas positioned on the deck were all in need of heating to remain functional throughout the mission in addition to being heated by the sun, thus automatically heating the air masses right above the lander deck with diffusive heat from the deck. By means of the Telltale wind data it was possible to setup an accurate flow simulation to study these scenarios in detail using Computational Fluid Dynamics. The CFD simulations show that, although the magnitude of the winds measured during the mission is sufficient to overpower the buoyancy forces of the thermal plumes from the lander, the obstacles on the deck perturb the wind flow sufficiently to raise the thermal wake and influence mainly the bottom thermocouple's temperature. The results show that, for moderate wind velocities (2 to 4 m s^{-1}) and typical midday lander deck heating ($\Delta T = 40 \text{ K}$), it is possible for the bottom thermocouple to measure an elevated temperature of 1 to 2 K above the undisturbed atmospheric value, as shown in Figure 24. Under certain circumstances, even the middle thermocouple can also be affected. [Davy *et al.*, 2010].

5.3. Wind Effects on Sample Delivery

[47] Due to potential contamination problems, the SSI was usually not operated during sample delivery. However, on sol 122 ($L_s \sim 133^\circ$), a delivery of the organic free blank (OFB) was attempted, and simultaneously, the SSI was taking images of the Telltale.

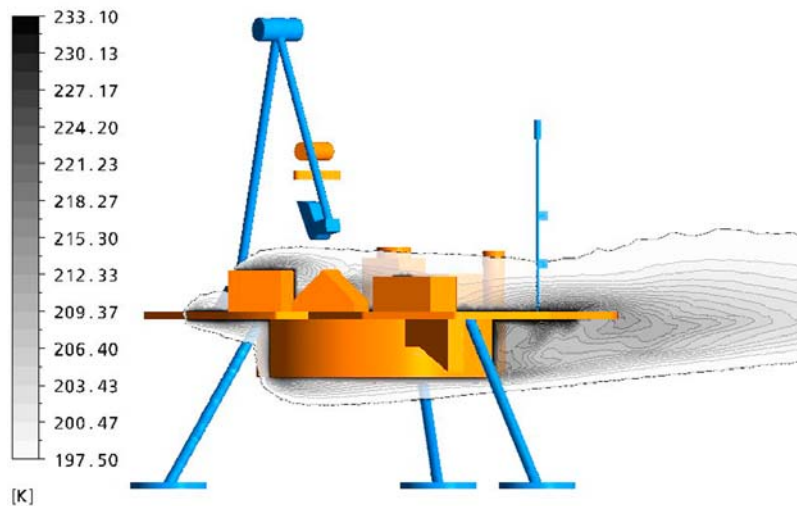


Figure 24. Example of results of the lander heating simulation using $\Delta T = 40$ K and $v = 4$ m s⁻¹. Temperature scale of the left is in Kelvin. The bottom and middle thermocouple are seen as the blue boxes on the MET mast to the right.

[48] As is seen in Figure 25, particles of the OFB do not drop vertically down, but make an angle of 10°–70° relative to the vertical. At low Reynolds numbers, the ratio of drag forces to gravitational forces is [Fox and McDonald, 1985]

$$\frac{F_D}{F_g} = \frac{18\mu v}{d^2 \rho_p g}$$

where μ is the kinematic viscosity (1.1×10^{-5} [m² s⁻¹]) [Holstein-Rathlou et al., 2008], d the particle, g the gravity acceleration and ρ_p its density assuming spherical, non-porous particles (2.52 g cm⁻³ for the OFB; Macor datasheet available at <http://www.coming.com/assets/0/965/989/1081/83CD6BA1-2665-4624-BBD5-ABC5FFF040FC.pdf>). During the delivery, the Telltale data showed 6–8 m s⁻¹ winds from south. From the position of the Robotic Arm Camera (RAC) over the TEGA during the taking of this image, particles should move toward the right in the image field as is seen (see Figure 25). Particles with diameters in the range from 0.3 to 1.0 mm would under these conditions show this behavior.

[49] In view of how easily samples are blown away from the delivery position, it seems strange that any sample delivery has been successful. It is quite possible that loose dust has been removed without entering the instruments, but excavations in the work area around the Phoenix Lander show very cloddy soil [Arvidson et al., 2009]. This ensures that samples delivered to TEGA and MECA fell as conglomerates of effectively larger particle size in the airstream ensuring successful, and somewhat difficult, delivery [Kounaves et al., 2009].

5.4. Frost

[50] Nighttime observations made of the Telltale after sol 78 ($L_s \sim 112^\circ$) quite frequently showed frost on the Telltale mirror. One special case was the night between sols 79 and 80 ($L_s \sim 112^\circ$ – 113°) where the frost appeared on the Telltale mirror throughout the course of a 64 image series. The sequence starts at 0028:32 LMST and the first definite signs

of change in the mirror are seen at 0036:51 LMST when the temperature goes below 192.5 K (see Figure 26). The ice remains on the Telltale mirror during the 3 image series at 0322 LMST though it seems to slowly dissipate from the right side of the mirror (see Figure 27). The ice is completely gone when the next set of Telltale images are taken at 1333:19 LMST on sol 80. With no images of the Telltale in the meantime it is not possible to say when the ice completely disappeared.

[51] From the Telltale images and data from the top thermocouple we can calculate the partial pressure of water with the Goff Gratch equation for saturation pressure of water vapor over ice [Smithsonian Institution, 1951]. At the first definite sign of change in the mirror, the saturation pressure of water over ice is 0.049 Pa, which is of the same order as has been reported by Zent et al. [2008].

5.5. Dust Raising Events

[52] During the first ~70 sols, two periods of increased optical depth were observed, at sols 5–7 ($L_s \sim 79^\circ$ – 80°) and sols 25–40 ($L_s \sim 88^\circ$ – 94.5°) [Tamppari et al., 2010]. These two periods are characterized by slightly elevated pressure relative to the seasonal decline in pressure levels [Taylor et al., 2010]. When these dust events are traced back in MARCI data [Ellehoj et al., 2010], they seem to originate at the pole when the remaining CO₂ frost in the north polar region disappears. Two possible hypotheses are that either the sublimation of the remaining CO₂ frost lifts dust into suspension or that below the CO₂ ice layer is dust that is easily put into suspension by the local winds. Solar induced basal sublimation of the translucent north polar CO₂ ice leading to the formation of vents [Kieffer et al., 2006; Thomas et al., 2010] likely carry too little dust to explain these observations (N. Thomas, private communication, 2009).

[53] As previously mentioned, between sol 70 and sol 100 ($L_s \sim 108^\circ$ – 23°) there are two periods of increased wind speeds at around sols 77 and 94 ($L_s \sim 112^\circ$ and 120°). These events correlate with the passing of condensate clouds over the landing site [Ellehoj et al., 2010], increased dust devil

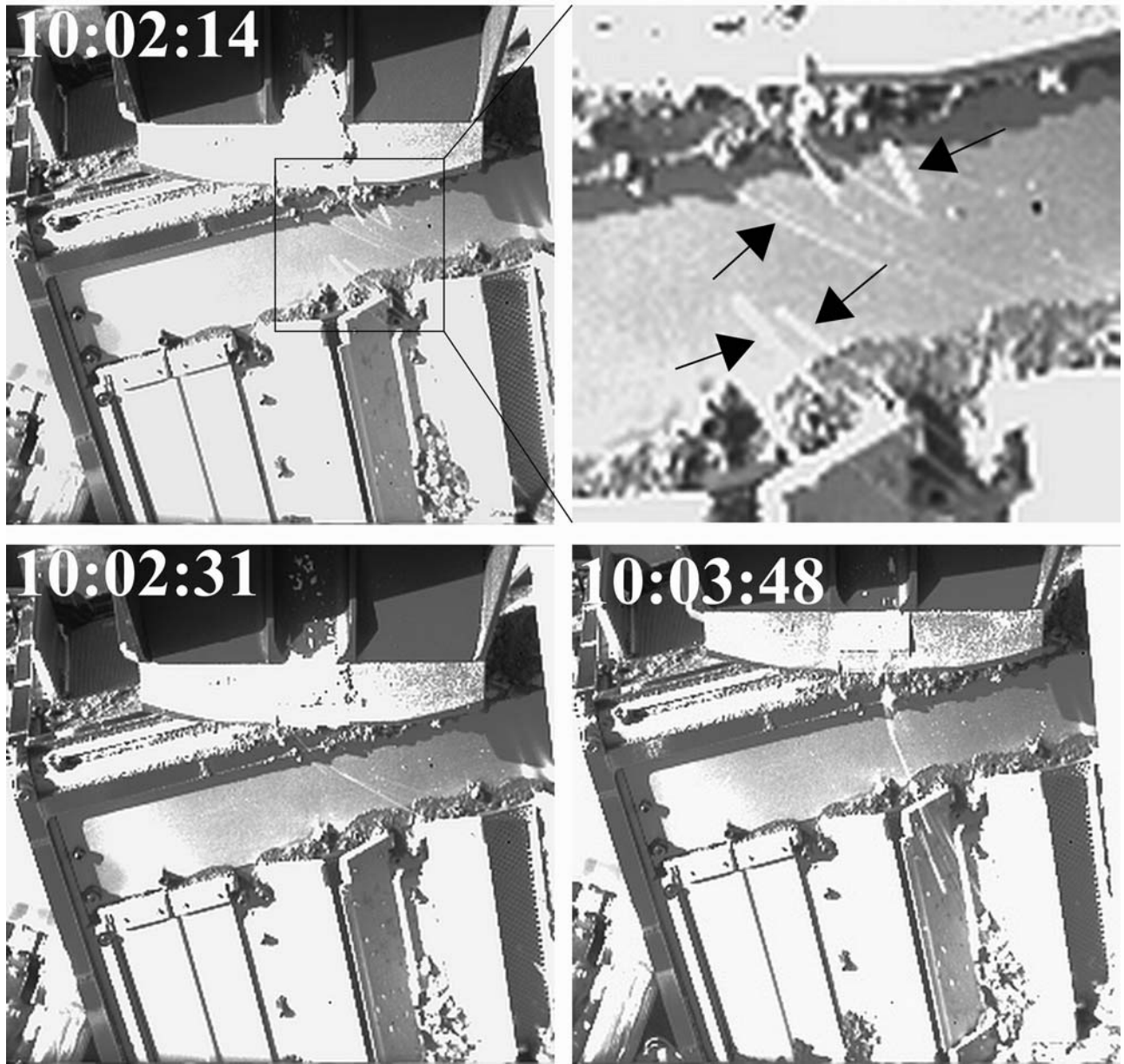


Figure 25. Series of robotic arm camera (RAC) images obtained at the LMST indicated, showing the delivery of the OFB to the TEGA instrument. The arrow in the top right image points to white streaks which are the wind-swept falling particles.

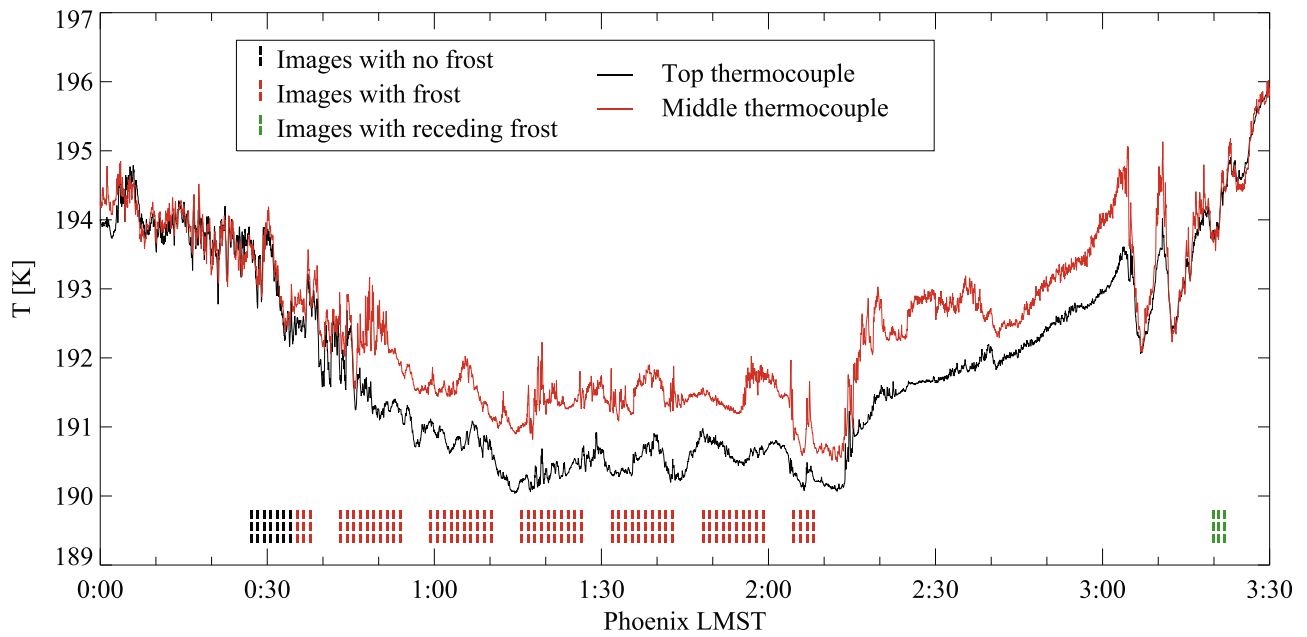


Figure 26. Temperature measurements from the top and middle thermocouple in the early morning of sol 80 ($L_s \sim 113^\circ$) with the times of simultaneous Telltale images marked with the lines at the bottom.

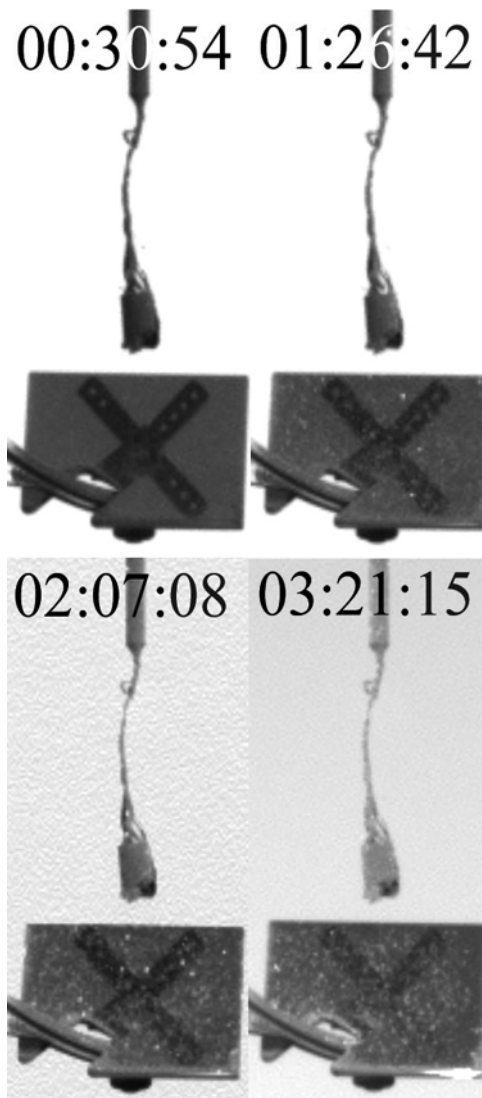


Figure 27. Sample Telltale images from early morning sol 80 ($L_s \sim 113^\circ$) showing the frost evolution on the mirror from frost-free at 0030:54 to completely covered at 0321:15. Times are in LMST and the wind is $4.0(5) \text{ m s}^{-1}$ from north-west in all four images.

activity [Ellehoj *et al.*, 2010] and the latter period is accompanied by a decreased pressure level relative to the seasonal decline [Taylor *et al.*, 2010]. South of 70°N the condensate clouds do not seem to be related to major dust activity. However, when these condensate clouds approach the north polar region, dust raising events are observed. The fact that the passing of condensate clouds is related to dust raising events in the north polar region, but not at lower latitudes, is a standing inconsistency. There are at least two hypotheses for explaining this observation; either the winds pick up when

approaching the polar region and/or there is more dust available for lifting in the polar region.

[54] From the MARCI mosaics the dust raising events, or dust storms, develop within the north polar dune fields or in very close proximity to them. Figure 28 shows one example of this behavior when condensate clouds reach Olympia Undae. On sol 128 ($L_s \sim 136.5^\circ$) a condensate cloud, centered on 70°N , 90°E , is approaching the north polar dune field. No major dust activity is seen. On sol 129 ($L_s \sim 137^\circ$) the cloud has reached the north polar region and dust storm activity is seen at 75°N , 115°E . This dust activity has spread out on sol 130 ($L_s \sim 137.5^\circ$) and a major dust storm has developed by sol 131 ($L_s \sim 138^\circ$) centered around 76°N , 143°E . A similar dust raising event was responsible for the clouds over the Phoenix Lander on sol 150 ($L_s \sim 147^\circ$), an event that eventually led to the end of the mission. The generation of a dust storm over or in very close proximity to the darker albedo dune fields to the north suggests that the enhancement of frontal winds by thermally generated afternoon winds along the boundary of the ice cover outliers and the surrounding dark frost-free terrain plays a significant role in storm generation. Though most of the dunes have shown no movement since Mariner 9, there has been some local mass movement observed in this region in the past 10 years [Bourke *et al.*, 2008]. This indicates that there is dust available for lifting if a front generating strong enough surface winds passes through the region.

[55] The data presented above suggest two types of dust raising mechanisms that affected the Phoenix landing site during the mission. The first mechanism is related to the sublimation of the north polar CO_2 seasonal ice cap. These events may not be related to weather systems as they do not result in increased wind speeds. This mechanism ends when the CO_2 ice from the north polar region has (mostly) evaporated. The second mechanism is related to weather systems, characterized in orbital data by condensate clouds, lower pressures [Taylor *et al.*, 2010] and increased dust devil activity [Ellehoj *et al.*, 2010]. These weather systems were observed regularly in the last part of the Phoenix mission. In between these two mechanisms, the atmosphere was rather clear and the lowest optical depths observed [Tamppari *et al.*, 2010].

6. Conclusions

[56] The Telltale has been the single most photographed object on the Mars Phoenix Lander and the obtained data set has been the first of its kind from this region of Mars. Being dependent on the SSI for imaging has resulted in an intermittent data set, but the sheer number of images combined with the calm nighttime conditions have allowed for good diurnal coverage.

[57] During nighttime wind speeds of $\sim 4 \text{ m s}^{-1}$ were observed with low variability in speed and direction. During daytime, turbulence influenced wind measurements lead-

Figure 28. (left) Time series showing MARCI color images from sols 128–131 ($L_s \sim 137^\circ$ – 138°). The color images are composites generated using 420 nm, 550 nm, and 600 nm filter band images. They have been polar stereographically projected at resolution of 2 km. The north pole is toward the bottom left in the image surrounded by the dark dune fields. (right) We have picked out specific features in the original color images. Condensate clouds are shown in blue, and bright reddish areas correspond to suspended dust. The Phoenix landing site is outside the image frame toward the left (68.22°N , 116.45°W).

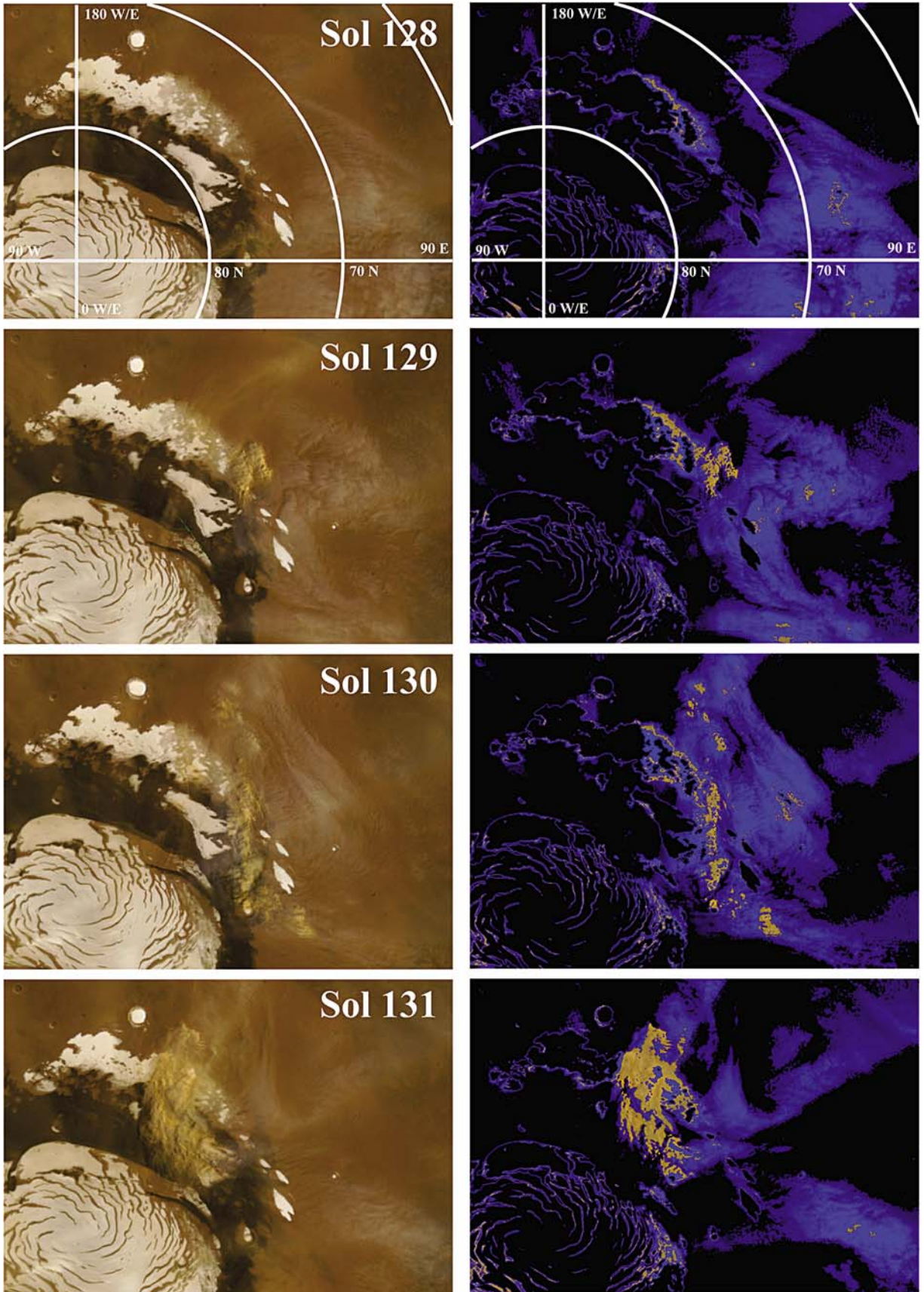


Figure 28

ing to 15–40% variability for wind speeds between 1 and 10 m s⁻¹.

[58] The surface roughness height was estimated using two techniques; the blurring of the Telltale which measures the strength of the 3 Hz turbulence and by using wind stability at nighttime. Both methods give roughly the same measure, 6(3) mm and 5(3) mm, respectively, giving a rough confidence in these numbers. Both estimates are lower than estimates from Mars Pathfinder and the Viking missions which is expected from the rock depleted landing site of the Phoenix mission.

[59] A change in the wind pattern was observed during the mission. Up to sol ~100 (L_s ~123°), wind directions were from the north and northeast during nighttime and completed a full clockwise rotation during daytime. Later in the mission daytime wind speeds increased and wind directions became generally from the west. The maximum observed wind speed of 16(1) m s⁻¹ is sufficient to lift agglomerates, but not sand grains, into suspension.

[60] Combining the knowledge of the Telltale data set with the atmospheric temperature and pressure measurements resulted in explanations for several observed phenomena. The nighttime temperature fluctuations are hypothesized to be due to atmospheric disturbances from the nearby Heimdal crater. The absence of temperature fluctuations after wind directions change strengthens this hypothesis. The Phoenix Lander itself is shown to be a source of heated air masses which are blown toward the MET mast. The resulting disturbance for the bottom thermocouple makes it unreliable for temperature measurements.

[61] Throughout the mission the Telltale wind measurements were used as a guideline for when to deliver samples, but delivery of the organic free blank was made while high daytime winds and turbulence was present, resulting in the sample being blown away. From RAC images of the blown away sample the size of the particles moved by the wind can be determined.

[62] Frost was seen to appear during a nighttime imaging sequence on the Telltale mirror. Together with temperature measurements, this event was used to validate the theoretical values for water over ice saturation pressures at the time of ice formation.

[63] Days with unusually high wind speeds are associated with the passing of condensate clouds as seen in MARCI images. Weather systems containing such condensate clouds have been observed to invoke dust storms when passing over the north polar dune fields. This was observed frequently as the Phoenix mission came to an end. Dust events observed early in the Phoenix mission by increased optical depth do not associate with increased wind speeds and seem to have a different source. When such dust events are traced back in MARCI images they coincide with the sublimation of the seasonal CO₂ ice cap.

[64] **Acknowledgments.** The Telltale project has been supported by the Danish Natural Science Research Council. The support of the Canadian Space Agency for the work of J. A. Davis and C. F. Lange is gratefully acknowledged. The authors acknowledge A. Leung for CFD simulations of the Telltale, and J. Boddez and G. Heacock for creation of the Open Lander model used in the CFD simulations. L. Tamppari's contribution to the research described in this paper was carried out at the Jet Propulsion Laboratory, California Institute of Technology, under a contract with NASA.

References

- Arvidson, R. E., et al. (2008), Mars Exploration Program 2007 Phoenix landing site selection and characteristics, *J. Geophys. Res.*, *113*, E00A03, doi:10.1029/2007JE003021.
- Arvidson, R. E., et al. (2009), Results from the Mars Phoenix Lander Robotic Arm Experiment, *J. Geophys. Res.*, *114*, E00E02, doi:10.1029/2009JE003408.
- Bourke, M. C., K. S. Edgett, and B. A. Cantor (2008), Recent aeolian dune change on Mars, *Geomorphology*, *94*, 247–255, doi:10.1016/j.geomorph.2007.05.012.
- Davis, J. A., and C. F. Lange (2009a), Simulations of vertically dominant flow around the wind sensor on the Phoenix Mars Lander, paper presented at 17th Annual Conference of the CFD Society of Canada, CFDSC2009, Ottawa, Ont., Canada.
- Davis, J. A., and C. F. Lange (2009b), Numerical analysis and characterization of the Phoenix MET instruments, *Rep. 2010-03-31-CSA-Lange-ME-01*, Univ. of Alberta, Edmonton, Alberta, Canada.
- Davy, R., J. A. Davis, P. A. Taylor, C. F. Lange, W. Weng, J. Whiteway, and H. P. Gunnlaugsson (2010), Initial analyses of air temperature and related data from the Phoenix MET station and their use in estimating turbulent heat fluxes, *J. Geophys. Res.*, *115*, E00E13, doi:10.1029/2009JE003444.
- Drake, N. B., L. K. Tamppari, R. D. Baker, B. A. Cantor, and A. S. Hale (2006), Dust devil tracks and wind streaks in the north polar region of Mars: A study of the 2007 Phoenix Mars Lander sites, *Geophys. Res. Lett.*, *33*, L19S02, doi:10.1029/2006GL026270.
- Ellehoj, M. D., et al. (2010), Phoenix Mars Lander: Vortices and dust devils at the landing site, *J. Geophys. Res.*, *115*, E00E16, doi:10.1029/2009JE003413.
- Forget, F., F. Hourdin, R. Fournier, C. Hourdin, and O. Talagrand (1999), Improved general circulation models of the Martian atmosphere from the surface to above 80 km, *J. Geophys. Res.*, *104*, 24,155–24,176, doi:10.1029/1999JE001025.
- Fox, R. W., and A. T. McDonald (1985), *Introduction to Fluid Mechanics*, 3rd ed., John Wiley, New York.
- Frisch, U. (1995), *Turbulence: The Legacy of A.N. Kolmogorov*, Cambridge Univ. Press, Cambridge, U. K.
- Gierasch, P., and R. Goody (1968), A study of the thermal and dynamical structure of the Martian lower atmosphere, *Planet. Space Sci.*, *16*, 615–636, doi:10.1016/0032-0633(68)90102-5.
- Golombek, M. P., et al. (1997), Overview of the Mars Pathfinder Mission and assessment of landing site predictions, *Science*, *278*, 1743–1748, doi:10.1126/science.278.5344.1743.
- Gunnlaugsson, H. P., et al. (2008), The Telltale wind experiment on Mars Phoenix Lander, *J. Geophys. Res.*, *113*, E00A04, doi:10.1029/2007JE003008.
- Heet, T. L., R. E. Arvidson, S. C. Cull, M. T. Mellon, and K. D. Seelos (2009), Geomorphic and geological settings of the Phoenix Lander mission landing site, *J. Geophys. Res.*, *114*, E00E04, doi:10.1029/2009JE003416.
- Hess, S., R. Henry, C. Leovy, J. Ryan, and J. Tillman (1977), Meteorological results from the surface of Mars: Viking 1 and 2, *J. Geophys. Res.*, *82*, 4559–4574, doi:10.1029/JS082i028p04559.
- Holstein-Rathlou, C., H. P. Gunnlaugsson, and J. P. Merrison (2008), Telltale calibration report, version 7, Dep. of Phys. and Astron., Aarhus Univ., Aarhus, Denmark.
- Kaimal, J. C., J. C. Wyngaard, Y. Izumi, and O. R. Cote (1972), Spectral characteristics of surface-layer turbulence, *Q. J. R. Meteorol. Soc.*, *98*, 563–589, doi:10.1002/qj.49709841707.
- Kieffer, H. H., P. R. Christensen, and T. N. Titus (2006), CO₂ jets formed by sublimation beneath translucent slab ice in Mars' seasonal south polar ice cap, *Nature*, *442*, doi:10.1038/nature04945.
- Kounaves, S. P., D. Catling, B. C. Clark, L. DeFlores, K. Gospodinova, M. H. Hecht, J. Kapit, D. W. Ming, R. C. Quinn, and The Phoenix Science Team (2009), Aqueous carbonate chemistry of the Martian soil at the Phoenix landing site, *Lunar Planet. Sci.*, *XL*, Abstract 2489.
- Lemmon, M. T., et al. (2008), The Phoenix Surface Stereo Imager (SSI) Investigation, *Lunar Planet. Sci.*, *XXXIX*, Abstract 2156.
- Leovy, C. B. (1981), Observations of Martian tides over two annual cycles, *J. Atmos. Sci.*, *38*, 30–39, doi:10.1175/1520-0469(1981)038<0030:OOMTOT>2.0.CO;2.
- Malin, M. C., J. F. Bell III, W. Calvin, R. T. Clancy, R. M. Haberle, P. B. James, S. W. Lee, P. C. Thomas, and M. A. Caplinger (2001), Mars Color Imager (MARCI) on the Mars Climate Orbiter, *J. Geophys. Res.*, *106*, 17,651–17,672, doi:10.1029/1999JE001145.
- Malin, M. C., W. Calvin, B. A. Cantor, R. T. Clancy, R. M. Haberle, P. B. James, P. C. Thomas, M. J. Wolff, J. F. Bell III, and S. W. Lee (2008), Climate, weather, and north polar observations from the Mars Reconnaissance

- sance Orbiter Mars Color Imager, *Icarus*, 194, 501–512, doi:10.1016/j.icarus.2007.10.016.
- Merrison, J. P., H. Bechtold, H. Gunnlaugsson, A. Jensen, K. Kinch, P. Nørnberg, and K. Rasmussen (2008), An environmental simulation wind tunnel for studying aeolian transport on Mars, *Planet. Space Sci.*, 56, 426–437.
- Moores, J. E., M. T. Lemmon, P. H. Smith, L. Komguem, and J. Whiteway (2010), Atmospheric dynamics at the Phoenix landing site as seen by the Surface Stereo Imager (SSI), *J. Geophys. Res.*, 115, E00E08, doi:10.1029/2009JE003409.
- Schofield, J. T., J. R. Barnes, D. Crisp, R. M. Haberle, S. Larsen, J. A. Magalhães, J. R. Murphy, A. Seiff, and G. Wilson (1997), The Mars Pathfinder Atmospheric Structure Investigation/Meteorology (ASI/MET) experiment, *Science*, 278, 1752–1758, doi:10.1126/science.278.5344.1752.
- Smith, P. H., et al. (2009), Water at the Phoenix landing site, *Science*, 325, 58–61, doi:10.1126/science.1172339.
- Smithsonian Institution (1951), *Smithsonian Meteorological Tables*, 6th rev. ed., 350 pp., Washington, D. C.
- Sullivan, R., R. Greeley, M. Kraft, G. Wilson, M. Golombek, K. Herkenhoff, J. Murphy, and P. Smith (2000), Results of the Imager for Mars Pathfinder windsock experiment, *J. Geophys. Res.*, 105, 24,547–24,562, doi:10.1029/1999JE001234.
- Tamppari, L. K., et al. (2010), Phoenix and MRO coordinated atmospheric measurements, *J. Geophys. Res.*, doi:10.1029/2009JE003415, in press.
- Taylor, P. A., D. C. Catling, M. Daly, C. S. Dickinson, H. P. Gunnlaugsson, A. Harri, and C. F. Lange (2008), Temperature, pressure, and wind instrumentation in the Phoenix meteorological package, *J. Geophys. Res.*, 113, E00A10, doi:10.1029/2007JE003015.
- Taylor, P. A., et al. (2010), On Pressure Measurement and Seasonal Pressure Variations during the Phoenix mission, *J. Geophys. Res.*, 115, E00E15, doi:10.1029/2009JE003422.
- Thomas, N., C. J. Hansen, G. Portyankina, and P. S. Russell (2010), HiRISE observations of gas sublimation-driven activity in Mars' southern polar regions: II. Surficial deposits and their origins, *Icarus*, 205, 296–310.
- Tillman, J. E., L. Landberg, and S. E. Larsen (1994), The boundary layer of Mars: Fluxes, stability, turbulent spectra, and growth of the mixed layer, *J. Atmos. Sci.*, 51(12), 1709–1727, doi:10.1175/1520-0469(1994)051<1709:TBL0MF>2.0.CO;2.
- Tyler, D., Jr., J. R. Barnes, and E. D. Skillingstad (2008), Mesoscale and large-eddy simulation model studies of the Martian atmosphere in support of Phoenix, *J. Geophys. Res.*, 113, E00A12, doi:10.1029/2007JE003012.
- Whiteway, J., M. Daly, A. Carswell, T. Duck, C. Dickinson, L. Komguem, and C. Cook (2008), Lidar on the Phoenix mission to Mars, *J. Geophys. Res.*, 113, E00A08, doi:10.1029/2007JE003002.
- Zent, A., M. Hecht, S. Wood, D. Cobos, T. Hudson, S. Milkovich, and P. Smith (2008), Regolith-Atmosphere H₂O exchange and surface energy balances at the Phoenix landing site, *Eos Trans. AGU*, 89(53), Fall Meet. Suppl., Abstract U11B-0031.
- Zurek, R. W. (1976), Diurnal tide in the Martian atmosphere, *J. Atmos. Sci.*, 33, 321–337, doi:10.1175/1520-0469(1976)033<0321:DTITMA>2.0.CO;2.
- K. M. Bean and M. T. Lemmon, Department of Atmospheric Sciences, Texas A&M University, College Station, TX 77843, USA.
- B. A. Cantor and M. C. Malin, Malin Space Science Systems Inc., PO Box 910148, San Diego, CA 92191, USA.
- J. A. Davis and C. F. Lange, Department of Mechanical Engineering, University of Alberta, Edmonton, AB T6G 2M7, Canada.
- R. Davy and P. A. Taylor, Centre for Research in Earth and Space Science, York University, Toronto, ON M3J 1P3, Canada.
- N. B. Drake, D. E. Shaw Research, 120 West 45th St., New York, NY 10036, USA.
- M. D. Ellehoj and M. B. Madsen, Niels Bohr Institute, University of Copenhagen, DK-1165 Copenhagen, Denmark.
- W. Goetz and S. F. Hviid, Max Planck Institute for Solar System Research, Max-Planck-Str. 2, D-37191 Katlenburg-Lindau, Germany.
- H. P. Gunnlaugsson, C. Holstein-Rathlou, J. P. Merrison, and P. Nørnberg, Department of Physics and Astronomy, Aarhus University, Ny Munkegade 120, DK-8000 Aarhus C, Denmark. (holstein@phys.au.dk)
- S. E. Larsen, Wind Energy Department, Risoe National Laboratory, Technical University of Denmark, DK-4000 Roskilde, Denmark.
- J. E. Moores and P. Smith, Lunar and Planetary Laboratory, University of Arizona, Tucson, AZ 85719, USA.
- K. Tamppari, Jet Propulsion Laboratory, California Institute of Technology, Pasadena, CA 91125, USA.